

REPORT DOCUMENTATION PAGE				<i>Form Approved</i> <i>OMB No. 0704-0188</i>	
<small>Public reporting burden for this collection of information is estimated to average 1 hour per response, including the time for reviewing instructions, searching existing data sources, gathering and maintaining the data needed, and completing and reviewing this collection of information. Send comments regarding this burden estimate or any other aspect of this collection of information, including suggestions for reducing this burden to Department of Defense, Washington Headquarters Services, Directorate for Information Operations and Reports (0704-0188), 1215 Jefferson Davis Highway, Suite 1204, Arlington, VA 22202-4302. Respondents should be aware that notwithstanding any other provision of law, no person shall be subject to any penalty for failing to comply with a collection of information if it does not display a currently valid OMB control number. PLEASE DO NOT RETURN YOUR FORM TO THE ABOVE ADDRESS.</small>					
1. REPORT DATE (DD-MM-YYYY)		2. REPORT TYPE		3. DATES COVERED (From - To)	
4. TITLE AND SUBTITLE				5a. CONTRACT NUMBER	
				5b. GRANT NUMBER	
				5c. PROGRAM ELEMENT NUMBER	
6. AUTHOR(S)				5d. PROJECT NUMBER	
				5e. TASK NUMBER	
				5f. WORK UNIT NUMBER	
7. PERFORMING ORGANIZATION NAME(S) AND ADDRESS(ES)				8. PERFORMING ORGANIZATION REPORT NUMBER	
9. SPONSORING / MONITORING AGENCY NAME(S) AND ADDRESS(ES)				10. SPONSOR/MONITOR'S ACRONYM(S)	
				11. SPONSOR/MONITOR'S REPORT NUMBER(S)	
12. DISTRIBUTION / AVAILABILITY STATEMENT					
13. SUPPLEMENTARY NOTES					
14. ABSTRACT					
15. SUBJECT TERMS					
16. SECURITY CLASSIFICATION OF:			17. LIMITATION OF ABSTRACT	18. NUMBER OF PAGES	19a. NAME OF RESPONSIBLE PERSON
a. REPORT	b. ABSTRACT	c. THIS PAGE			19b. TELEPHONE NUMBER (include area code)

FINAL PERFORMANCE REPORT

Contract/Grant Title: Closely coupled multi-mode radiators: A new concept for improving the performance of electrically small antennas.

Contract/Grant No.: N00014-11-1-0618

Reporting Period: 1 April 2011 – 31 August 2015

Report Date: 23 November 2015

Sponsoring/Monitoring DoD Organization:

Office of Naval Research
875 North Randolph Street
Arlington, VA 22203-1995

Program Officer: Capt. Benjamin Pimentel, ONR 30

Performing Organization:

THE BOARD OF REGENTS OF THE UNIVERSITY OF WISCONSIN
RESEARCH & SPONSORED PROGRAMS
21 N. PARK STREET SUITE 6401
MADISON, WI 53715-1218

Principal Investigator:

Nader Behdad
Department of Electrical and Computer Engineering
1415 Engineering Drive,
Madison, WI 53706
Tel: (608) 262 8804
Email: behdad@wisc.edu
Fax: (608) 262 1267

Contents

1. Abstract.....	3
2. Summary of Main Accomplishments of This Project.....	3
3. Compact, Ultra-Wideband Antennas with Monopole Like Radiation.....	4
3.1. <i>Development of a low-profile, ultra-wideband antenna</i>	4
3.2. <i>Development of a small UWB antenna occupying a cubic volume</i>	5
4. Development of a Compact, Ultra-Wideband, Circularly-Polarized Spiral Antenna	6
5. RF Signature Reduction of Linearly- and Circularly-Polarized Antennas	7
5.1. <i>Harmonic Suppressed Miniaturized Element Frequency Selective Surfaces</i>	7
5.2. <i>Integration of the Antennas with Harmonic Suppressed FSSs</i>	8
6. Development of Wideband Antennas With Directional Radiation in the Azimuth Plane	9
7. Enhancement of the Bandwidth of HF Antennas by Exploiting the Supporting Platform.....	10
8. Publications Resulted from This Efforts	11
9. Inventions and Patents Resulted from This Effort	12
10. Appendix A: Copies of the Journal Papers Resulted From This Work.....	13

1. Abstract

Final performance report of the Young Investigator Program (YIP) project titled “Closely coupled multi-mode radiators: A new concept for improving the performance of electrically small antennas” is presented in this document. The research conducted in this project resulted in a number of unique ultra-wideband antenna designs for operation in military communications systems of interest to the U.S. Navy and Marine Corps. Specifically, as part of this project, we developed and experimentally demonstrated a number of UWB antennas that, for a given occupied volume, have the lowest frequencies of operation that are reported to date. Other major findings of this project include the introduction, development, and experimental demonstration of miniaturized, wideband, circularly polarized antennas, low-observable electrically-small antennas that exploit miniaturized-element frequency selective surfaces, antennas with directional radiation patterns in the azimuth plane, and platform-based antennas for wideband HF communications. The findings of this project are expected to advance the state-of-the-art in development of military antennas used for tactical communications systems operating in the HF, VHF, and UHF frequency bands.

2. Summary of Main Accomplishments of This Project

The broad objective of this project was to use the advances in the areas of multi-mode, closely coupled miniaturized radiators and artificially-engineered materials to bring about transformational advancements in development of ultra-broadband, highly-efficient, electrically small antennas. Upon conclusion of the project, a number of unique contributions were made to the field, which are listed below:

- Developed and experimentally demonstrated the lowest-profile, miniaturized UWB antenna that does not rely on resistive loading and achieves a 10:1 bandwidth.
- Developed and experimentally demonstrated the smallest UWB antenna occupying a cubic volume reported to date.
- Developed and experimentally demonstrated a new technique for designing compact, low-profile, UWB circularly-polarized spiral antennas.
- Developed techniques for RF signature reduction and visual signature elimination of both linear and CP versions of the UWB antennas.
- Developed metamaterial-based FSSs with harmonically suppressed responses over extremely broad bandwidths.
- Developed wideband antennas with directional radiation patterns in the azimuth plane for self-/co-site-interference mitigation.
- Developed a technique for taking advantage of platform to enhance the performance of platform-mounted HF antennas.

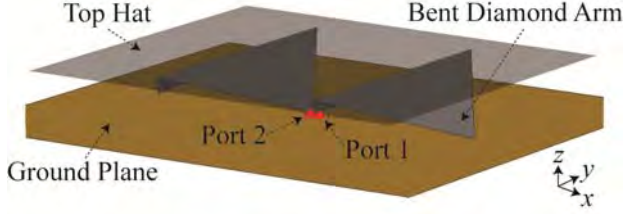


Fig. 1. Topology (left) and photograph (right) of a low-profile, ultra-wideband antenna developed in this project. This antenna has the lowest profile of all UWB antennas reported to date that radiates like a vertically-polarized monopole and have very compact dimensions. The antenna has an overall bandwidth of 4:1.

The results of our investigations in the aforementioned areas are described in the following sections.

3. Compact, Ultra-Wideband Antennas with Monopole Like Radiation

3.1. Development of a low-profile, ultra-wideband antenna

Fig. 1 shows the topology and photograph of a fabricated prototype of a low-profile UWB antenna developed in this project. The antenna is composed of two electrically-small loops coupled together in their near fields. Each loop has a three-dimensional surface with a bent-diamond-arm shape. Half of each loop placed on top of an infinite conducting ground plane is used in the design. Each loop is loaded with a top hat to reduce the lowest frequency of operation of the antenna. This antenna was designed and optimized in the initial stages of the project. The antenna radiates like a vertically-polarized monopole with omni-directional, vertically-polarized radiation patterns in the azimuth plane. The antenna demonstrates consistent radiation characteristics over a 4:1 frequency band. At its lowest frequency of operation, the antenna has an extremely low height of $0.033\lambda_{\min}$ where λ_{\min} is the free-space wavelength at the lowest frequency of operation of the antenna. Moreover, the antenna has lateral dimensions of $0.22\lambda_{\min} \times 0.22\lambda_{\min}$ at the lowest frequency of operation. Details of the design and optimization of this antenna are presented in a journal paper published in 2013 [1]. It is important to note that the combination of wide bandwidth, low-profile, and compact dimensions of this antenna have not yet been matched by any other design reported in the literature to date.

While the antenna shown in Fig. 1 is capable of delivering impressive performance levels, its bandwidth is limited to two octaves. Obtaining greater bandwidths may be of interest in some applications. To extend the bandwidth of this antenna, we examined the factors that limits its bandwidth. It was found that the bandwidth of this antenna is limited by the fact that its radiation patterns are deteriorated as frequency increases. This is due to the fact that as frequency increases, the radiation emanating from the different locations of the antenna have a larger phase difference between them. This way, the radiation emanating from the antenna adds constructively at some angles and destructively at others resulting in deterioration of the radiation pattern of the structure from the desired omni-directional patterns at higher frequencies. To overcome this limitation and extend the bandwidth of the antenna, we proposed a new design

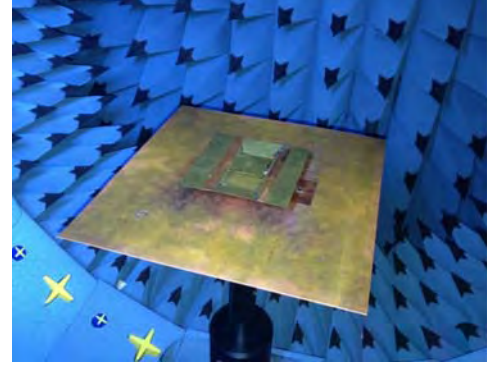
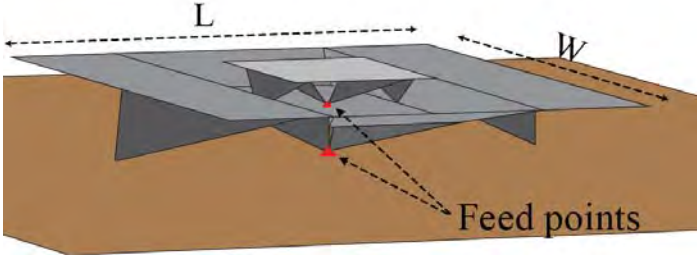


Fig. 2. Topology (left) and photograph (right) of the fabricated prototype of a low-profile, ultra-wideband antenna that is capable of providing a 10:1 bandwidth with vertically-polarized, omni-directional radiation patterns across its entire band of operation.

of a wideband antenna that takes advantage of the previous antenna in a dual-antenna system. This significantly enhances the bandwidth over which the antenna can maintain its omni-directionality. The topology and the photograph of a fabricated prototype of this modified antenna is shown in Fig. 2. We demonstrated experimentally that this antenna can cover up to a decade of bandwidth with consistent, vertically-polarized, omni-directional patterns across the entire band. At its lowest frequency of operation, this antenna has electrical dimensions of $0.026 \lambda_{\min} \times 0.026 \lambda_{\min} \times 0.046 \lambda_{\min}$, where λ_{\min} is the wavelength at the lowest frequency of operation. The complete details of the design, fabrication, and characterization of this antenna are reported in a paper that we published in IEEE Transactions on Antennas and Propagation in 2015 [2].

3.2. Development of a small UWB antenna occupying a cubic volume

As part of this project, we also investigated the development of small, ultra-wideband antennas that efficiently occupy a cubic volume. The antenna developed in this part of the project is an

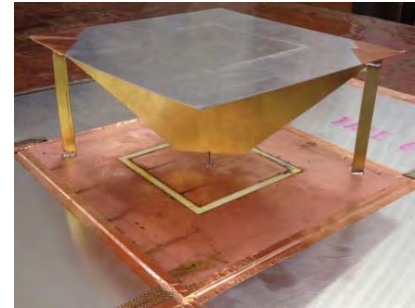
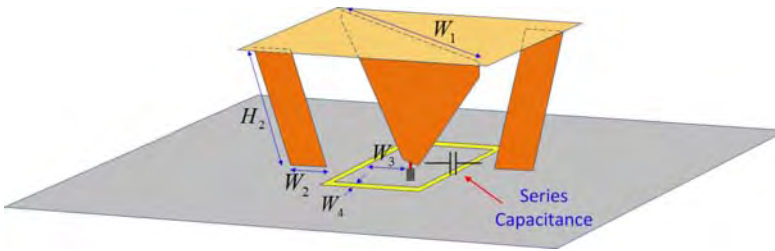


Fig. 3. Topology (left) and photograph (right) of the fabricated prototype of a compact ultra-wideband antenna that efficiently utilizes the volume of a cuboid. This antenna is capable of providing a 5.5:1 bandwidth with vertically-polarized, omni-directional radiation patterns across its entire band of operation.

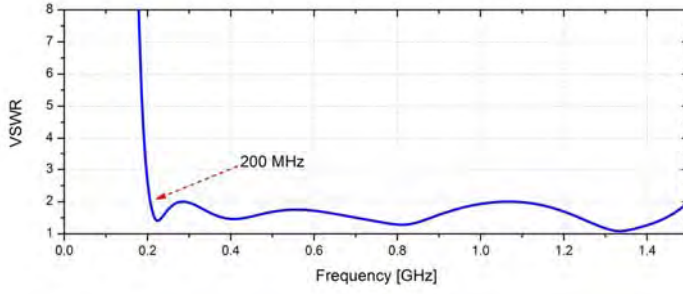


Fig. 4. The measured input VSWR of the antenna prototype shown in Fig. 3.

electrically small, low-profile, ultra wideband antenna with monopole-like radiation characteristics. Fig. 3 shows the topology and the photograph of a fabricated prototype of this antenna. The antenna is composed of a monopole bow-tie antenna reactively loaded with a cascaded system of top hats, two shorting arms, and a ring slot cut into the ground plane. The reactive loads are used to introduce two additional resonances close to each other and below the lowest resonant frequency of the bow-tie. This results in a very compact, ultra-wideband antenna that utilizes the available volume inside the Chu's sphere rather efficiently. At the lowest frequency of operation, the proposed antenna has electrical dimensions of $0.085 \lambda_{\min} \times 0.19 \lambda_{\min} \times 0.19 \lambda_{\min}$, where λ_{\min} is the free-space wavelength. The antenna demonstrates a VSWR of 2.2:1 and consistent monopole-like, omnidirectional radiation patterns over a 5.5:1 bandwidth. The details of the design and optimization of the antenna as well as the results of the experimental characterization of the antenna are reported in a paper that we published in IEEE Antennas and Wireless Propagation Letters in 2014 [3].

4. Development of a Compact, Ultra-Wideband, Circularly-Polarized Spiral Antenna

As part of this project, we also developed a new technique for designing low-profile, compact spiral antennas with a broadband circularly polarized (CP) responses. The antenna is backed by a ground plane and has unidirectional radiation patterns over its entire frequency band of operation. Fig. 5 shows the topology and the photograph of the fabricated antenna. This antenna is a multilayer structure composed of a center-fed modified Archimedean spiral that exploits a novel loading structure, a ring-shaped absorber, and a feed network, which includes a 180° power splitter. The loading structure possesses both inductive and capacitive characteristics, which increase the equivalent electrical length of the antenna while maintaining its maximum dimensions. The Archimedean spiral is integrated into the multilayer dielectric structure along with its differential feed network. An optimized ring-shaped absorber is used on the periphery of the antenna to reduce the ground effects on the antenna performance. The antenna developed in this part of the project occupies a volume that is 89% smaller than that occupied by a conventional ground-plane-backed Archimedean spiral antenna. At its lowest frequency of operation, the antenna has electrical dimensions of $0.21\lambda_{\min} \times 0.21\lambda_{\min} \times 0.09\lambda_{\min}$, where λ_{\min} is the free-space wavelength at the lowest frequency of operation (0.5 GHz). Over the frequency range from 0.5 to 1.4 GHz (2.8:1), the antenna has a VSWR of 2.4:1, and it has a CP radiation pattern with an axial ratio better than 1.2 dB. Within this frequency range, the antenna has minimum and maximum realized gain values of -5.0 dBiC and 3.1 dBiC, respectively. Details of the design, optimization, simulation, and the measured results of the fabricated prototype of this

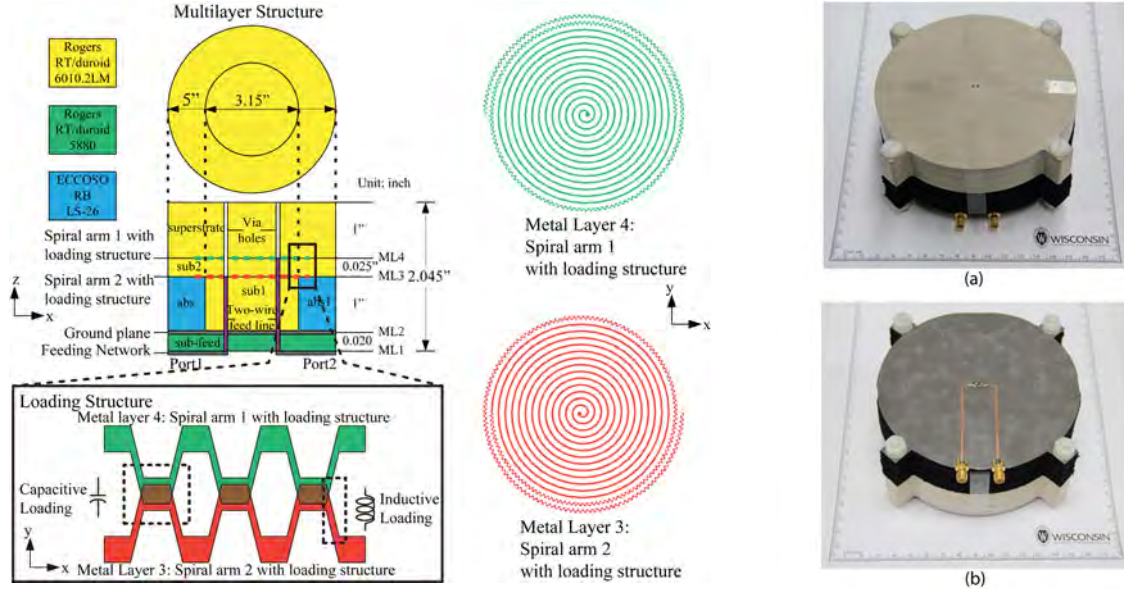


Fig. 5. (Left) Topology of the miniaturized, ground-plane backed, circularly-polarized UWB antenna developed in this project. (Right) Photograph of the fabricated prototype.

antenna were published in IEEE Transactions on Antennas and Propagation in 2015 [4]. A copy of this paper is attached in Appendix A.

5. RF Signature Reduction of Linearly- and Circularly-Polarized Antennas

In this project, we also examined the design of low-observable antennas where the radar cross section of the antenna is reduced by using a miniaturized-element frequency selective surface (MEFSS) and integrating it with a low-profile, wideband, circularly-polarized or linearly-polarized antenna. In this section, we will first describe the design and operation of the harmonic suppressed MEFSSs and then discuss the design of the low-observable antennas.

5.1. Harmonic Suppressed Miniaturized Element Frequency Selective Surfaces

We introduced a new technique for designing miniaturized-element frequency selective surfaces

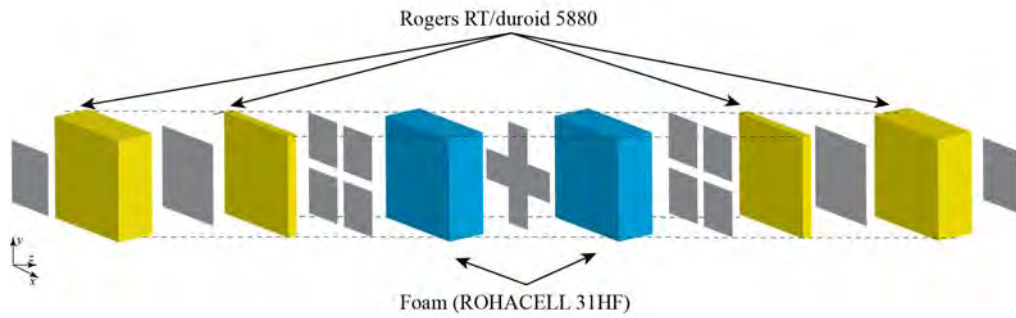


Fig. 6. Topology of the unit cell of a miniaturized-element frequency selective surface with harmonic suppression over a very wide band.

having bandpass responses and no spurious transmission windows over extremely large bandwidths. The proposed harmonic-suppressed MEFSSs consist of multiple metallic and dielectric layers. The unit cell of this MEFSS is shown in Fig. 6. Each metallic layer is in the form of a two-dimensional arrangement of capacitive patches or an inductive wire grid with extremely sub-wavelength periods. Harmonic-free operation in these structures is achieved by using multiple, closely spaced capacitive layers with overlapping unit cells to synthesize a single, effective capacitive layer with a larger capacitance value. This allows for reducing the unit cell size of a conventional MEFSS considerably and moving the natural resonant frequencies of its constituting elements to considerably higher frequencies. Consequently, the spurious transmission windows of such MEFSSs, which are caused by these higher order harmonics, can be shifted to very high frequencies and an extremely broad frequency band free of any spurious transmission windows can be obtained.

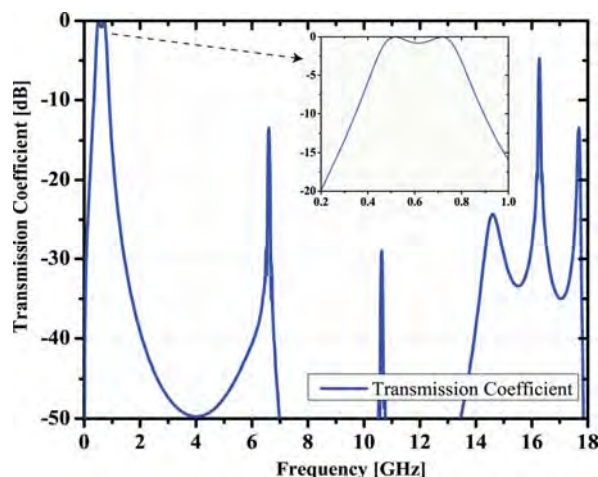


Fig. 7. Simulation results of a low-frequency MEFSS which has harmonic suppressed responses up to about 18 GHz.

Using this technique, a number of MEFSSs with second-order bandpass responses are designed. Fig. 7 shows the simulated responses of one such structure that operates in the lower UHF frequency band with harmonic suppression up to around 18 GHz or so. This represents an approximately 30:1 frequency band where the structure's harmonics are significantly suppressed. Other prototypes of these types of MEFSSs were also designed and fabricated and characterized. Details of the design and measurement results of these prototypes are given in a paper that we published in IEEE Transactions on Antennas and Propagation in 2014 [5]. This paper is also attached in Appendix A of this report.

5.2.Integration of the Antennas with Harmonic Suppressed FSSs

The MEFSSs demonstrated in the previous sub-section were also integrated with low-profile, linearly- and circularly-polarized antennas. Fig. 8 shows a photograph of the linearly-polarized antenna integrated with the MEFSS. The antenna radiates similar to a vertically-polarized monopole but is completely flush mounted. The antenna also has omni-directional radiation patterns

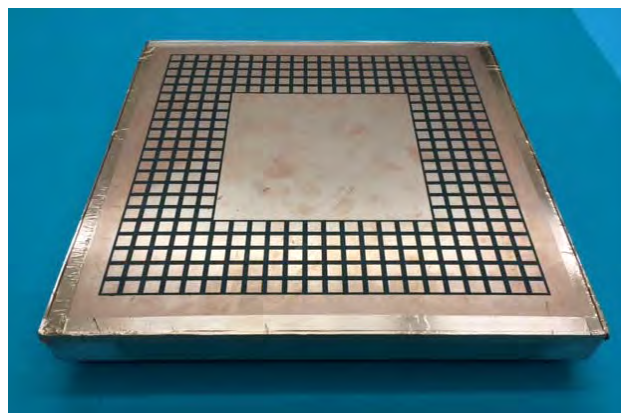


Fig. 8. Photograph showing the fabricated integrated antenna/FSS prototype.

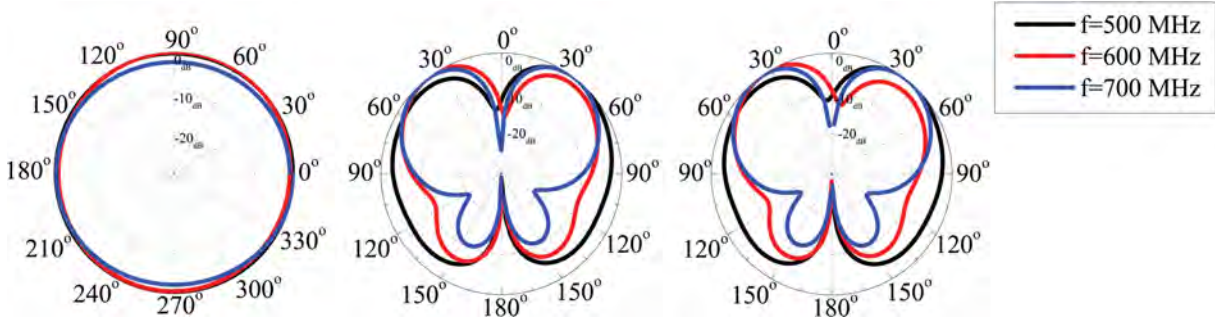


Fig. 9. Measured radiation patterns of the antenna shown in Fig. 8. (Left) Measured radiation patterns in the azimuth plane. (Center) Elevation plane (x-z plane). (Right) Elevation plane (y-z plane).

in the azimuth plane. The antenna is cavity-backed and the frequency selective surface is completely integrated with the antenna within the cavity. The FSS is designed to be transparent in the frequency range where the antenna is expected to radiate. Outside of this frequency range, it presents a metallic ground plane where the FSS shields the antenna, at frequencies where the radar cross section of the antenna may be high.

The radiation properties of the antenna were also measured and the results are shown in Fig. 9. As can be seen, along the azimuth plane, the antenna shows a completely omni-directional radiation pattern. The radiation patterns of the antenna in the elevation plane are also shown in this figure and as can be seen, the antenna has radiation patterns similar to those of a monopole antenna on top of a finite ground plane.

6. Development of Wideband Antennas With Directional Radiation in the Azimuth Plane

In this project, we also developed a low-profile, compact and wideband vertically-polarized antenna demonstrating directional radiation characteristics in both the azimuth and the elevation planes of radiation. The antenna is composed of four bent-diamond-shaped half loops placed on a ground plane. A photograph of the fabricated prototype of this antenna is shown in Fig. 10. The half loops are fed at their centers and short circuited to the ground at their ends. Two of the half loops are fed in phase while the other two are fed with 180° phase difference generating omni-directional and figure-eight shaped radiation patterns, respectively. Coherent combination of these radiation patterns

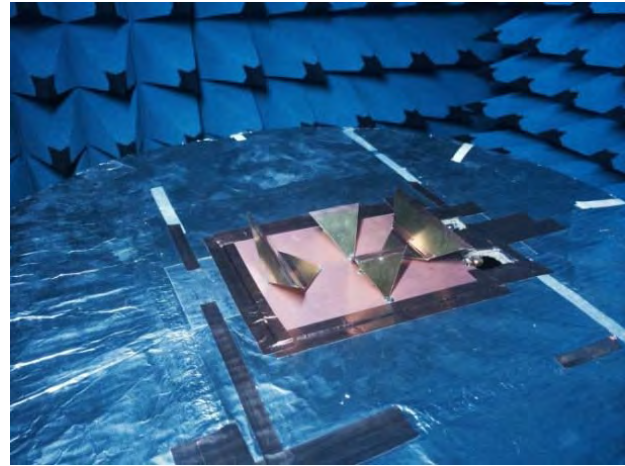


Fig. 10. Photograph of a low-profile, vertically-polarized, wideband antenna with directional radiation patterns in the azimuth plane. The antenna was developed as part of this project.

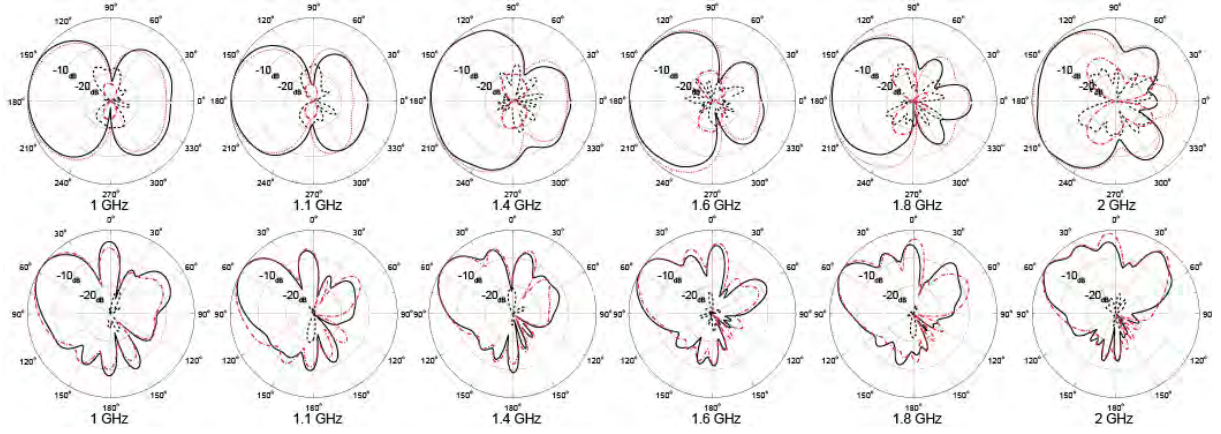


Fig. 11. Simulated and measured radiation patterns of the antenna shown in Fig. 10. (Top) The radiation patterns in the azimuth plane. (Bottom) The radiation patterns in the elevation plane.

generates a cardioid-shaped directional pattern. A prototype of the antenna was fabricated and characterized. The antenna has electrical dimensions of $0.54\lambda_{\min} \times 0.4\lambda_{\min} \times 0.116\lambda_{\min}$ at its lowest frequency of operation and operates over a 2:1 bandwidth. The radiation patterns and the other radiation characteristics of this antenna were measured. Fig. 11 shows the measured and simulated radiation patterns of the antenna in the azimuth (top row) and in the elevation (bottom row) planes. Details of the design and fabrication along with the detailed measurement results of this antenna are reported in an article that we published in *IEEE Antennas and Wireless Propagation Letters* in 2015 [6]. This paper is also provided in Appendix A.

7. Enhancement of the Bandwidth of HF Antennas by Exploiting the Supporting Platform

Many antennas working at the high frequency (HF) band have significantly smaller dimensions than the operating wavelength and thus, suffer from narrow bandwidths. In many military applications, such HF antennas are mounted on relatively large metallic platforms. In this part of the project, we studied how a platform mounted antenna can be used to excite the natural resonant modes of the platform to increase the overall bandwidth of the system. This way, the platform acts as the main radiator and the mounted antennas act primarily as the coupling mechanism between the antenna and the external circuit. We used the theory of characteristic modes to identify the appropriate platform modes and determine the efficient means of exciting them. This allows for significantly increasing the bandwidth of the antenna system compared to what is achievable using the mounted antennas in isolation. This approach was employed to successfully enhance the bandwidth of a horizontally-polarized HF antenna system by as much as 10 times compared to a stand-alone antenna operating in free space. Scaled models of the proposed antennas were fabricated and experimentally characterized. Measurement results were observed to be in good agreement with the theoretically predicted results and demonstrated the feasibility of using the proposed approach in designing bandwidth-enhanced platform-mounted HF antennas. The work conducted in this area was summarized in a paper, which was submitted to *IEEE Transactions on Antennas and Propagation* and is under review [7].

8. Publications Resulted from This Efforts

The list of the papers published as a result of this effort is provided. In total, 7 journal papers were resulted from this research efforts, 6 of which are already published and one is still under review. Additionally, 2 invited conference papers [8-9] and 15 contributed conference papers were also resulted from this research project [10-24].

1. N. Behdad, L. Meng, and Y. Yusuf, "A Very Low-Profile, Omnidirectional, Ultrawideband Antenna," *Antennas and Wireless Propagation Letters, IEEE*, vol. 12, pp. 280-283, 2013.
2. K. Ghaemi and N. Behdad, "A Low-Profile, Vertically Polarized Ultrawideband Antenna With Monopole-Like Radiation Characteristics," *Antennas and Propagation, IEEE Transactions on*, vol. 63, pp. 3699-3705, 2015.
3. S. M. A. M. H. Abadi and N. Behdad, "An Electrically Small, Vertically Polarized Ultrawideband Antenna With Monopole-Like Radiation Characteristics," *Antennas and Wireless Propagation Letters, IEEE*, vol. 13, pp. 742-745, 2014.
4. Ting-Yen Shih and N. Behdad, "A Compact, Broadband Spiral Antenna With Unidirectional Circularly Polarized Radiation Patterns," *Antennas and Propagation, IEEE Transactions on*, vol. 63, pp. 2776-2781, 2015.
5. S. M. A. Momeni Hasan Abadi, L. Meng, and N. Behdad, "Harmonic-Suppressed Miniaturized-Element Frequency Selective Surfaces With Higher Order Bandpass Responses," *Antennas and Propagation, IEEE Transactions on*, vol. 62, pp. 2562-2571, 2014.
6. K. Ghaemi and N. Behdad, "A Low-Profile, Wideband Antenna with Vertically-Polarized Directional Radiation," *Antennas and Wireless Propagation Letters, IEEE (Accepted for Publication)*.
7. T. Y. Shih and N. Behdad, "Bandwidth Enhancement of Platform-Mounted HF Antennas Using the Characteristic Mode Theory," *submitted to IEEE Transactions on Antennas and Propagation*.
8. T.-Y. Shih and N. Behdad, "Design of platform-mounted HF/VHF antennas using the characteristics mode theory" *2015 International Workshop on Antenna Technology (iWAT 2015)*, March 4-6 2015, Seoul, Republic of Korea.
9. K. Ghaemi and N. Behdad, "A low-profile, compact, wideband antenna array with cardioid-shaped radiation patterns in the azimuth plane," *2015 International Workshop on Antenna Technology (iWAT 2015)*, March 4-6 2015, Seoul, Republic of Korea.
10. T.-Y. Shih and N. Behdad, "Bandwidth Enhancement of HF Antennas Mounted on Military Platforms Using a Characteristic-Modes-Based Design Approach," *International Symposium on Antennas and Propagation (ISAP2015)*, 9-12 Nov. 2015, Hobart, Tasmania, Australia.
11. T.-Y. Shih and N. Behdad, "Bandwidth Enhancement of Expeditionary-Fighting-Vehicle-Mounted Antennas Using the Characteristic Mode Theory," *Antenna Applications Symposium*, Robert Allerton Park, Monticello IL, Sep. 22-24 2015.
12. T. Y. Shih and N. Behdad, "Bandwidth Enhancement of Platform-Mounted HF Antennas Using the Characteristic Modes Theory," *2015 IEEE Int. Symp. Antennas and Propagation and North American Radio Sci. Meeting*, 19-25 July 2015, Vancouver, BC, Canada.

13. K. Ghaemi and N. Behdad, "A low-profile, wideband, vertically-polarized antenna with directional radiation patterns in the azimuth plane," *2015 IEEE Int. Symp. Antennas and Propagation and North American Radio Sci. Meeting*, 19-25 July 2015, Vancouver, BC, Canada.
14. K. Ghaemi and N. Behdad, "A Low-Profile, Wideband, Vertically-Polarized Antenna with Directional Radiation Patterns in the Azimuth Plane," 19th International Conference on Antennas and Propagation, December 2-5 2014, Kaohsiung, Taiwan.
15. T.-Y. Shih[#] and N. Behdad, "Miniaturization of A Circularly-Polarized, Uni-Directional, Ultra-Wideband Spiral Antenna," *2014 IEEE International Symposium on Antennas and Propagation and USNC-URSI Radio Science Meeting*, July 6-12, 2014, Memphis, TN.
16. S. M. A. Momeni Hasan Abadi[#] and N. Behdad, "A Harmonic-Suppressed Miniaturized-Element Frequency Selective Surface With a Second-Order Bandpass Response," *2014 IEEE International Symposium on Antennas and Propagation and USNC-URSI Radio Science Meeting*, July 6-12, 2014, Memphis, TN.
17. S. M. A. Momeni Hasan Abadi[#] and N. Behdad, "A Miniaturized, Low-Profile, Omni-Directional Ultra-Wideband Antenna," *2014 IEEE International Symposium on Antennas and Propagation and USNC-URSI Radio Science Meeting*, July 6-12, 2014, Memphis, TN.
18. K. Ghaemi[#] and N. Behdad, "A Low-Profile, Vertically-Polarized, Compact, Ultra-Wideband Antenna with a 10:1 Bandwidth," *2014 IEEE International Symposium on Antennas and Propagation and USNC-URSI Radio Science Meeting*, July 6-12, 2014, Memphis, TN.
19. T.-Y. Shih and N. Behdad, "A Miniaturized, Ultra-Wideband, Circularly Polarized Spiral Antenna," *International Workshop on Antenna Technology (iWAT 2014)*, March 4-6, 2014, Sydney, Australia.
20. S. M. A. Momeni Hasan Abadi[#] and N. Behdad, "Harmonic-Suppressed Miniaturized-Element Frequency Selective Surfaces for Low-Observable Antenna Applications," *2013 AP-S/URSI Symposium*, Orlando, FL.
21. N. Behdad, "An Extremely Low-Profile Ultra-Wideband Antenna with Monopole-Like Radiation Characteristics," *2013 AP-S/URSI Symposium*, Orlando, FL.
22. Y. Yusuf[#] and N. Behdad, "Dual-mode, compact, low-profile ultra-wideband antennas," *Proceedings of the 2012 IEEE International Conference on Wireless Information Technology and Systems*, 11-16 November 2012, Maui, HI, pp. 1-4.
23. Y. Yusuf[#] and N. Behdad, "Compact, Low-Profile UWB Antennas Exploiting the Concept of Closely-Coupled Dual-Mode Radiators," *2012 IEEE International Symposium on Antennas and Propagation and USNC-URSI National Radio Science Meeting*, July 8-14, 2012, Chicago, IL, pp. 1-2.
24. N. Behdad, M. Li[#], and M. Al-Joumayly[#], "Ultra-Low Profile, Compact UWB Antennas Based on the Concept of Closely Coupled, Dual-Mode Radiators," *2011 Antenna Applications Symposium*, Robert Allerton Park, Monticello IL, September 20-22, 2011.

9. Inventions and Patents Resulted from This Effort

1. "Electrically-Small, Low-Profile, Ultra-Broadband Antenna," Inventors: Amin Momeni and Nader Behdad, filed with USPTO in May 2013.

2. “A low-profile, ultra-wideband antenna with monopole-like radiation characteristics,”
Inventors: Kasra Ghaemi and Nader Behdad, filed with USPTO on 6/4/2014 (US App.
No. 14/296,138).

10. Appendix A: Copies of the Journal Papers Resulted From This Work

A Very Low-Profile, Omnidirectional, Ultrawideband Antenna

Nader Behdad, *Senior Member, IEEE*, Meng Li, *Student Member, IEEE*, and Yazid Yusuf, *Member, IEEE*

Abstract—We present a compact, ultra-low-profile, ultrawideband (UWB) antenna with monopole-like radiation characteristics. The antenna is composed of two bent diamond-shaped loops that are fed in parallel and loaded with a common capacitive top hat to reduce their lowest frequencies of operation. A series capacitor is used at the feeding terminals of one of the loops to create an additional resonance below the lowest frequency of operation of one of the loops and, hence, further reduce the lowest frequency of operation of the antenna. At the lowest frequency of operation, the proposed antenna has electrical dimensions of $L \times W \times H = 0.22\lambda_{\min} \times 0.22\lambda_{\min} \times 0.033\lambda_{\min}$, where λ_{\min} is the free-space wavelength. The antenna demonstrates a VSWR lower than 3:1 and consistent monopole-like, omnidirectional radiation patterns over a 4:1 bandwidth. A prototype of the antenna with physical dimensions of $7 \times 7 \times 1 \text{ cm}^3$, which operates in the 1.0–4.0-GHz frequency range, is fabricated and characterized using a near-field system.

Index Terms—Broadband antennas, electrically small antennas, omnidirectional antennas, ultrawideband (UWB) antennas.

I. INTRODUCTION

ULTRAWIDEBAND (UWB) antennas have been the subject of many studies due to their widespread applications in areas ranging from wireless communications and sensing to radar systems and microwave imaging. Ultrawideband antennas are expected to radiate efficiently over large frequency bands and demonstrate consistent radiation characteristics over the entire band of operation. The size of a UWB antenna is primarily determined by its lowest frequency of operation. Therefore, in applications where relatively low RF/microwave frequencies are used, the physical size of a UWB antenna may become prohibitively large. Additionally, in certain low-frequency applications (e.g., military communications at HF, VHF, and UHF bands), antennas with monopole-like radiation patterns (i.e., vertically polarized with omnidirectional radiation patterns) are required. In such applications, besides having compact dimensions, reducing the overall height of the antenna and its overall visual signature becomes extremely important as well.

Various efforts have been made in the past to realize compact UWB antennas. Multiresonant structures composed of a monopole-like radiating structure loaded with a top hat and incorporating various impedance-matching elements (e.g., shorting pins or series inductors) within the body of the antenna were among the first structures examined in this area [1]–[3]. One of the earliest designs in this category is the antenna proposed by Goubau [2], which achieves a bandwidth¹ of about one octave while occupying a cylindrical volume with a diameter of $0.18\lambda_{\min}$ and a height of $0.065\lambda_{\min}$, where λ_{\min} is the free-space wavelength at the lowest frequency of operation. A somewhat different design was also proposed by Friedman in [3], which achieves a bandwidth of an octave from a structure occupying the same volume. More recently, a low-profile antenna with an overall height of $0.07\lambda_{\min}$, composed of a conducting body of revolution and a shorted parasitic ring was reported in [4].

Compact antennas that use loops as the main radiating elements have also been examined. In [5], a compact UWB antenna utilizing two coupled loops was demonstrated to achieve monopole-like radiation patterns over a very wide frequency band. Miniaturized versions of this antenna, which reduce the overall antenna height and lateral dimensions, were later reported in [6] and [7]. While all of these antennas achieve impressive performance levels, the smallest overall profile reported in these structures is limited to approximately $0.06\lambda_{\min}$ at the lowest frequency of operation. Recently, new designs have been reported that further reduce the overall profile of such UWB antennas [8]–[10]. However, these designs use either lossy ferrites [8] or resistive loading [9], [10] to load the antenna and achieve improved impedance matching at the lowest frequency of operation.

In this letter, we report an ultrawideband antenna with an extremely small overall height. The antenna is composed of two loops that are capacitively loaded with a common top hat to reduce their lowest frequencies of operation [6]. Each loop has a three-dimensional surface with a bent diamond shape. The two loops are fed in parallel using a power divider network. A series capacitor is used at the feeding terminals of one of the loops to create an additional resonance below the lowest frequency of operation of the loops and, hence, further reduce the lowest frequency of operation of the antenna. The antenna has electrical dimensions of $\sim 0.22\lambda_{\min} \times 0.22\lambda_{\min} \times 0.033\lambda_{\min}$ at its lowest frequency of operation and achieves a VSWR lower than 3:1 over an extremely broad frequency band. The antenna demonstrates omnidirectional monopole-like radiation patterns

Manuscript received January 23, 2013; revised February 13, 2013; accepted February 19, 2013. Date of publication February 22, 2013; date of current version March 14, 2013. This material is based upon work supported by the Office of Naval Research under ONR Award No. N00014-11-1-0618.

The authors are with the Department of Electrical and Computer Engineering, University of Wisconsin-Madison, Madison, WI 53706 USA (e-mail: behdad@wisc.edu).

Color versions of one or more of the figures in this letter are available online at <http://ieeexplore.ieee.org>.

Digital Object Identifier 10.1109/LAWP.2013.2248693

¹In the comparisons provided in this letter, the 3:1 VSWR bandwidth of all antennas are considered.

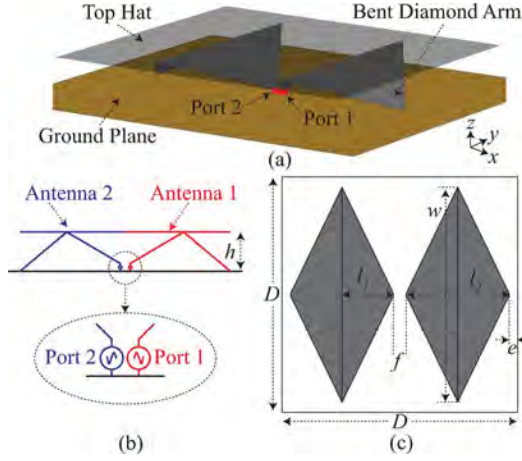


Fig. 1. (a) Three-dimensional topology of the proposed ultra-low-profile UWB antenna. (b) Side view of the antenna showing the two radiators and the feeding arrangement. (c) Top view of the structure.

over a bandwidth that exceeds 4:1. In what follows, first the design procedure of the antenna will be discussed in Section II. In Section III, measurement results of a fabricated prototype are presented, and Section IV concludes the letter.

II. ANTENNA DESIGN

Fig. 1(a) shows the three-dimensional (3-D) topology of the proposed antenna. Fig. 1(b) and (c) show respectively the side view and the top view of the structure. The antenna is composed of two identical radiators mounted on top of an infinite ground plane. Each radiator takes the shape of a bent diamond plate that is short-circuited at its end to the ground plane and is fed at the other end. Thus, each radiator and its image with respect to the ground plane form a loop with bent diamond-shaped arms. The two radiators are loaded with a common top hat, which connects to the diamond-shaped arms at the bend locations. The first resonance of each diamond loop occurs when the overall length of the structure, including the length of the image, is half a wavelength. The effect of the top hat is to capacitively load the antenna and, hence, reduce its lowest resonant frequency of operation [1], [6]. When the two radiators are fed in phase, they act as a coupled-loop antenna and demonstrate an ultra-broadband response. In this case, the antenna radiates in a manner similar to a vertically polarized monopole and demonstrates an omni-directional radiation pattern in the azimuth plane over a broad frequency band.

The main goal in the design process of this antenna is to reduce the lowest frequency of operation of the structure while minimizing its overall height and, to the extent possible, its lateral dimensions. To demonstrate the effect of the important parameters in the design process, we consider a prototype of this antenna with maximum lateral dimensions of $7 \times 7 \text{ cm}^2$. First, the effect of the antenna height on the performance of the structure is examined using full-wave electromagnetic (EM) simulations in CST Microwave Studio. In doing so, we assume that the two loops are fed in parallel [i.e., Ports 1 and 2 in Fig. 1(b) are connected, and $f = 0$ in Fig. 1(c)] and consider four different antenna heights in the 0.5–2.0-cm range. For each height, the dimensions of the free parameters in the antennas [l_1 , l_2 , and

w in Fig. 1(c)] are optimized to achieve a VSWR lower than 3:1 over as wide a frequency band as possible. The results of this study are shown in Fig. 2(a)–(c). Fig. 2(a) and (b) shows the real and imaginary parts of the input impedances of the antennas. As can be observed, when the antenna height is 0.5 cm, the input resistance is rather small, and the separation between resonant frequencies of the antenna is rather large. Thus, achieving broadband impedance matching is not possible. As the antenna height increases, however, the input resistance increases and, perhaps more importantly, the separation between the resonant frequencies decreases substantially. This makes it easier to achieve broadband impedance matching with a reasonably low VSWR. In addition to the height of the antenna, the bend location l_1 and the bend width w also impact the response of the structure. The effects of these parameters are also examined using full-wave EM simulations for a fixed height of 1.5 cm, and the results are shown in Fig. 2(d)–(i). As can be observed, the lowest VSWR is generally achieved when the bend location is in the middle of the diamond-shaped arm of the loop (i.e., $l_1 \approx 0.5l_2$). Additionally, increasing the width of the arms, w , improves the input VSWR, but also slightly increases the lowest frequency of operation of the antenna. Therefore, to achieve a VSWR lower than 3:1, w can be chosen to be slightly smaller than D .

One of the key challenges in designing compact, low-profile UWB antennas is reducing the lowest frequency of operation of the antenna without increasing its occupied volume. In the proposed antenna, the lowest frequency of operation can further be reduced by using the feeding arrangement shown in the inset of Fig. 3(c). In this case, a capacitor is used in series with one of the two loop antennas shown in Fig. 1(a), and then the two antennas are fed in parallel using a single source. Using this series capacitor, an additional resonance can be created, the frequency of which falls below the main resonant frequency of the antenna when the two radiators are directly fed in parallel (i.e., no capacitor is used). By changing the value of this capacitor, the frequency of this resonance can be changed as desired. If the frequency of this newly added resonance is close enough to the lowest frequency of operation of the loops, the lowest frequency of operation of the antenna can be further reduced. This scenario is shown in Fig. 3 for an antenna of the type shown in Fig. 1 with maximum dimensions of $7 \times 7 \times 1 \text{ cm}^3$. Fig. 3(a) and (b) shows the real and imaginary parts of the input impedance of the antenna with and without a 3.3-pF series capacitor. As can be clearly seen, the capacitor introduces a new resonance close to that of the main one. Fig. 3(c) compares the input VSWRs of the antenna with and without this feeding network. As can be observed, the lowest frequency where a VSWR of 3 is achieved is further reduced when the feeding network shown in the inset of Fig. 3(c) is used.

III. MEASUREMENT RESULTS AND DISCUSSION

A prototype of the antenna discussed in Section II with a single capacitor feed network is fabricated, and its photograph is shown in Fig. 4(a). A dielectric substrate covered with metal on one side is used as the ground plane of the two radiators. On the bottom side, a 50- Ω microstrip line is fabricated. At the end of this microstrip line, a through-substrate via is used to

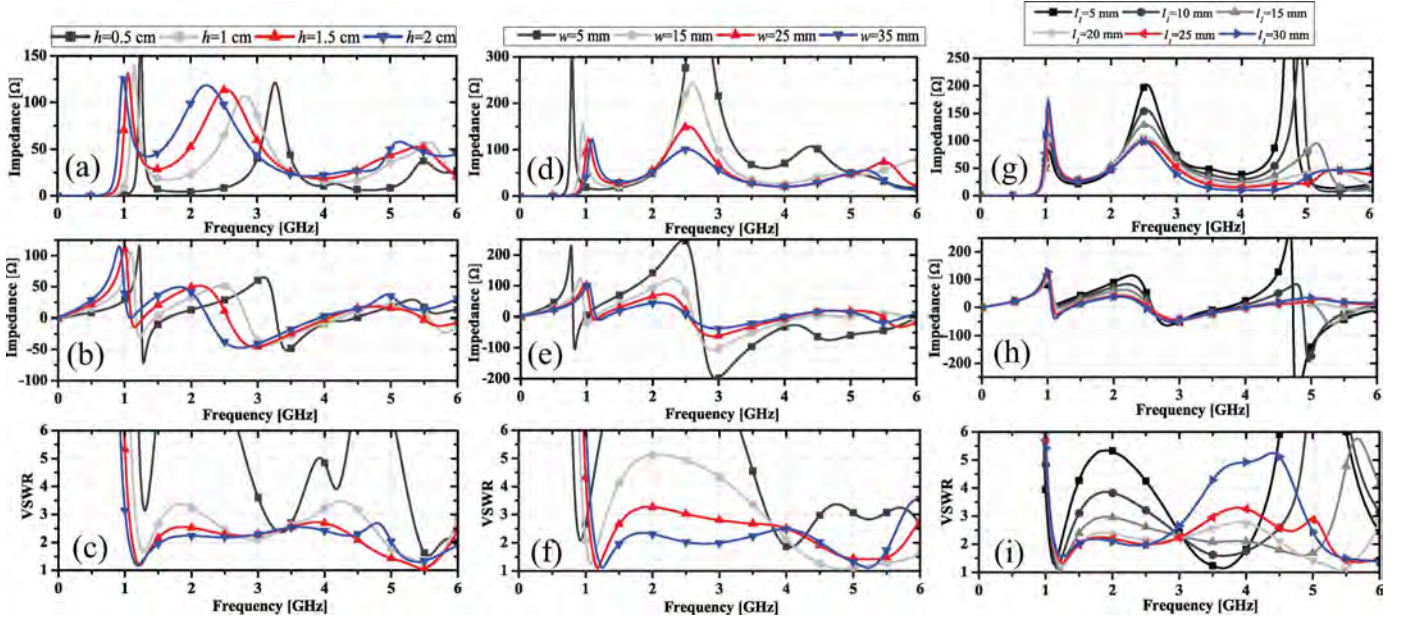


Fig. 2. (a)–(c) Effect of the antenna height on the performance of the proposed ultra-low-profile UWB antenna. (a) Real and (b) imaginary parts of the input impedance as well as the (c) input VSWR of the antennas optimized for different heights are shown. All antennas have $f = e = 0$ mm, $w = 31.5$ mm, and $l_2 = 35$ mm. The optimum l_1 values are 14, 17.5, 20, and 25 mm, respectively, for $h = 0.5, 1.0, 1.5$, and 2 cm. (d)–(f) Effect of the bent width w on the (d) real and (e) imaginary parts of the input impedance as well as the (f) input VSWR of the antenna. For cases (d)–(f), $h = 15$ mm, $l_1 = 20$ mm, and $l_2 = 35$ mm. (g)–(i) Effect of the bent location l_1 on the (g) real and (h) imaginary parts of the input impedance of the antenna and the (i) input VSWR. For cases (g)–(i), $h = 15$ mm, $l_2 = 35$ mm, and $w = 31.5$ mm.

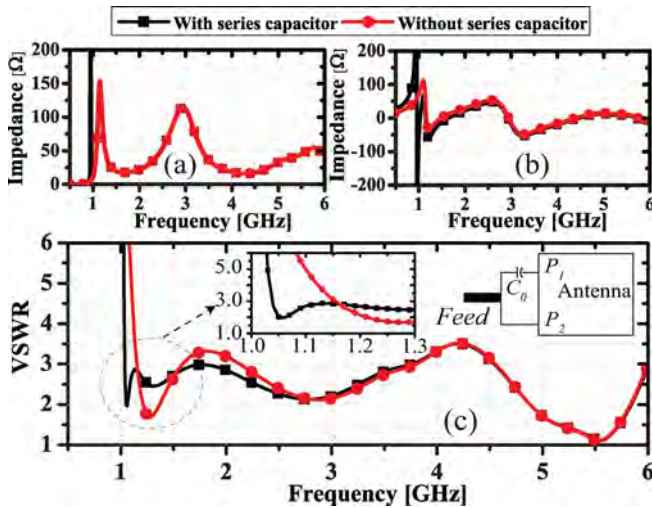


Fig. 3. (a), (b) Real and imaginary parts of the input impedances of the antenna with and without a series 3.3-pF capacitor used in the feed network shown in the inset of (c). (c) Input VSWR of the antenna with and without the series capacitor in the feeding network.

feed one of the radiators. A 3×3 -mm² metallic patch is located adjacent to the end of the feeding microstrip line and is connected to it using a 3.3-pF capacitor. The center of this patch is connected to the feeding terminal of the other radiator using a through-substrate via. A photograph of the feed network is shown in Fig. 4(b). During the measurements, the ground plane of the fabricated antenna is electrically connected to a large brass plate with dimensions of 30×30 cm² (i.e., the effective size of the finite ground plane is 30×30 cm²). The measured

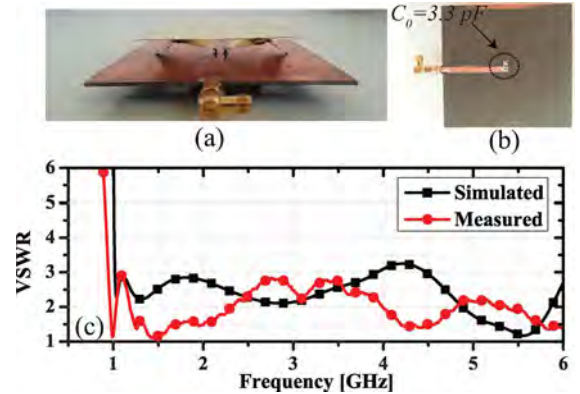


Fig. 4. (a) Photograph of the fabricated prototype. (b) Photograph of the power-divider feed network employing a 3.3-pF series capacitor. (c) Measured and simulated input VSWR of the antenna.

input VSWR of the prototype along with the predicted simulation results of the antenna, which models the feed network and the microstrip line, are shown in Fig. 4. In the simulation results shown in this figure, the lumped element capacitor is modeled as a series RLC circuit (with $R = 0.1 \Omega$, $L = 0.156$ nH, and $C = 3.3$ pF) to take into account the parasitic effects. As can be seen, a reasonable agreement between the simulation and measurement is achieved. The differences observed between the two results are attributed to uncertainties involved in precise modeling of the fabricated structure. Among others, examples include tolerances of the values of the capacitor, the dielectric constant, and the loss of the substrate as well as potential differences between the exact dimensions and precise shape of the 3-D loops and those of the modeled ones. Nevertheless, the measurement result demonstrates a broadband performance with an

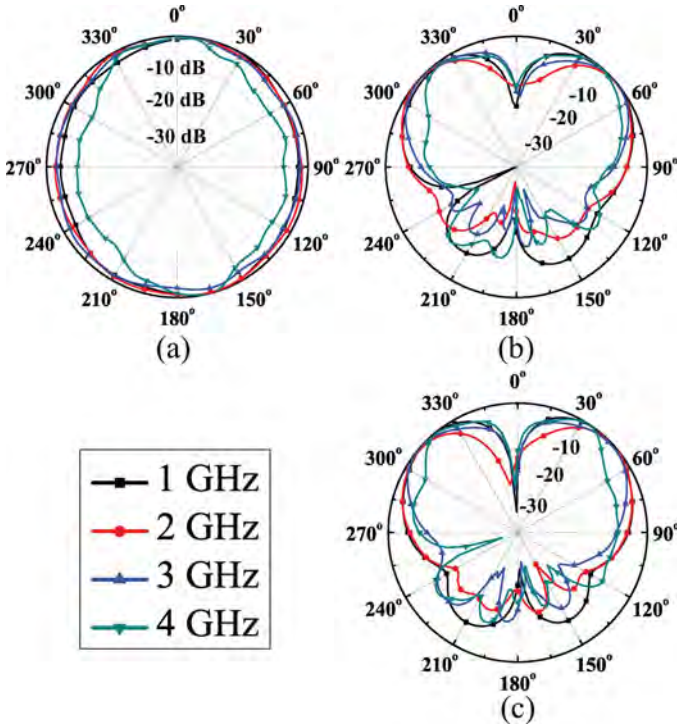


Fig. 5. Measured normalized radiation patterns of the antenna in the azimuth xz -plane and two elevation planes xz and yz . (a) Azimuth plane (xy). (b) Elevation plane (xz). (c) Elevation plane (yz).

input VSWR that remains lower than 3 over a frequency band of 0.95 to at least 6.0 GHz.

The radiation characteristics of the antenna are measured using a multiprobe near-field system from 0.8 to 6.0 GHz. Fig. 5 shows the measured radiation patterns of the antenna in the frequency range of 1.0–4.0 GHz. Observe that the antenna has an omnidirectional radiation pattern in the azimuth plane. The radiation patterns in two elevation planes (xz - and yz -planes) are shown. The antenna has figure-eight radiation patterns in both planes that are similar to those of a vertically polarized monopole on a finite ground plane. Overall, the antenna demonstrates reasonably stable and consistent radiation characteristics in the 1–4-GHz range. As frequency increases beyond 4 GHz, the radiation pattern of the antenna in the azimuth plane starts to become more directional.

The gain and radiation efficiency of the antenna are also measured using the same near-field system. In doing these measurements, a well-characterized double-ridged horn antenna was used as a reference to calibrate the near-field system for antenna gain measurements. The measured realized gain of the antenna, which includes the impedance mismatch effects, is shown in Fig. 6. The total efficiency of the antenna is also measured using the same multiprobe near-field system, and its radiation efficiency is extracted by taking out the effects of the impedance mismatch from the measured total efficiency. The radiation efficiency is also presented in Fig. 6. Over most of the operating band, the radiation efficiency remains above 80%.

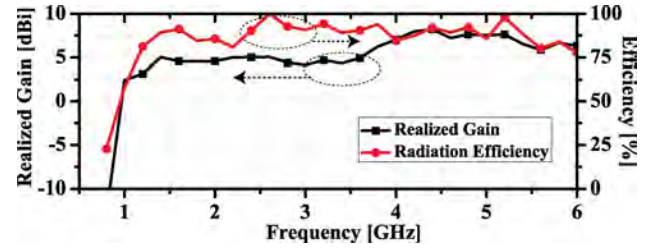


Fig. 6. Measured realized gain and the radiation efficiency of the antenna. The gain values reported take into account the effect of the impedance mismatch.

The minimum radiation efficiency is approximately 50% at the lowest frequency of operation.

IV. CONCLUSION

An extremely low-profile UWB antenna was presented in this letter. The proposed antenna takes advantage of two loop radiators with bent diamond-shaped arms. Using capacitive top hat loading and a simple capacitive feed network, the lowest frequency of operation of the antenna is reduced while maintaining its occupied volume. At the lowest frequency of operation, the antenna achieves electrical dimensions of $0.22\lambda_{\min} \times 0.22\lambda_{\min} \times 0.033\lambda_{\min}$. The proposed antenna demonstrates a VSWR lower than 3:1 and consistent, monopole-like radiation patterns over a frequency range of about two octaves. Because of its low profile and compact overall dimensions, scaled versions of this design are expected to be useful for low-frequency applications operating within the VHF and UHF frequency bands.

REFERENCES

- [1] E. W. Seeley, "An experimental study of the disk loaded folded monopole," *IRE Trans. Antennas Propag.*, vol. AP-4, no. 1, pp. 27–28, Jan. 1956.
- [2] G. Goubau, N. N. Puri, and F. Schwing, "Diakoptic theory for multi-element antennas," *IEEE Trans. Antennas Propag.*, vol. AP-30, no. 1, pp. 15–26, Jan. 1982.
- [3] C. H. Friedman, "Wide-band matching of a small disk-loaded monopole," *IEEE Trans. Antennas Propag.*, vol. AP-33, no. 10, pp. 1142–1148, Oct. 1985.
- [4] H. Nakano, H. Iwaoka, K. Morishita, and J. Yamauchi, "A wideband low-profile antenna composed of a conducting body of revolution and a shorted parasitic ring," *IEEE Trans. Antennas Propag.*, vol. 56, no. 4, pp. 1187–1192, Apr. 2008.
- [5] N. Behdad and K. Sarabandi, "A compact antenna for ultrawide-band applications," *IEEE Trans. Antennas Propag.*, vol. 53, no. 7, pp. 2185–2192, Jul. 2005.
- [6] N. Behdad, M. Al-Joumayly, and M. Salehi, "Ultra-wideband low profile antenna," US 8,228,251.
- [7] A. Elsherbini and K. Sarabandi, "Very low-profile top-loaded UWB coupled sectorial loops antenna," *IEEE Antennas Wireless Propag. Lett.*, vol. 10, pp. 800–803, 2011.
- [8] H. Moon, G.-Y. Lee, C.-C. Chen, and J. L. Volakis, "An extremely low-profile ferrite-loaded wideband VHF antenna design," *IEEE Antennas Wireless Propag. Lett.*, vol. 11, pp. 322–325, 2012.
- [9] S. Palud, F. Colombel, M. Himdi, and C. L. Meins, "Wideband omnidirectional and compact antenna for VHF/UHF band," *IEEE Antennas Wireless Propag. Lett.*, vol. 10, pp. 3–6, 2011.
- [10] Y. K. Yu and J. Li, "Analysis of electrically small size conical antennas," *Prog. Electromagn. Res. Lett.*, vol. 1, pp. 85–92, 2008.

ACKNOWLEDGMENT

The authors would like to thank the editors, reviewers, Dr. S. B. Yeap, Dr. R. Wong, and Dr. Z. Shu for their help to improve the quality of this communication.

REFERENCES

- [1] A. J. Paulraj, D. A. Gore, R. U. Nabar, and H. Bölcskei, "An overview of MIMO communications—A key to gigabit wireless," *Proc. IEEE*, vol. 92, no. 2, pp. 198–218, Feb. 2004.
- [2] C. B. Dietrich, K. Dietze, J. R. Nealy, and W. L. Stutzman, "Spatial, polarization, and pattern diversity for wireless handheld terminals," *IEEE Trans. Antennas Propag.*, vol. 49, no. 9, pp. 1271–1281, Sep. 2001.
- [3] Q. Rao and K. Wilson, "Design, modeling, and evaluation of a multiband MIMO/diversity antenna system for small wireless mobile terminals," *IEEE Trans. Antennas Propag.*, vol. 59, no. 3, pp. 410–419, Mar. 2011.
- [4] S. C. Del Barrio, A. Tatomirescu, G. F. Pedersen, and A. Morris, "Novel architecture for LTE world phone," *IEEE Antennas Wireless Propag. Lett.*, vol. 12, pp. 1676–1679, Jan. 2014.
- [5] L. Yang, M. Fan, F. Chen, J. She, and Z. Feng, "A novel compact electromagnetic band-gap (EBG) structure and its applications for microwave circuits," *IEEE Trans. Microw. Theory Tech.*, vol. 53, no. 1, pp. 183–190, Jan. 2005.
- [6] H. J. Chaloupka and X. Wang, "Novel approach for diversity and MIMO antennas at small mobile platforms," in *Proc. 15th IEEE Int. Symp. Pers. Indoor Mobile Radio Commun. (PIMRC' 04)*, Barcelona, Spain, Sep. 2004, vol. 1, pp. 637–642.
- [7] L. K. Yeung and Y. E. Wang, "Mode-based beamforming arrays for miniaturized platforms," *IEEE Trans. Microw. Theory Tech.*, vol. 57, no. 1, pp. 45–52, Jan. 2009.
- [8] X. Tang, K. Mouthaan, and J. C. Coetzee, "Beam steering with high front-to-back ratio and high directivity on small platforms using decoupled antenna pairs," in *Proc. Asia-Pac. Microw. Conf. (APMC)*, Melbourne, Australia, Dec. 2011, pp. 1326–1329.
- [9] J. Weber, C. Volmer, K. Blau, R. Stephan, and M. A. Hein, "Miniaturisation of antenna arrays for mobile communications," in *Proc. 35th European Microwave Conference, EuMC'05*, 2005, vol. 2, pp. 1173–1176.
- [10] J. Weber, C. Volmer, K. Blau, R. Stephan, and M. A. Hein, "Miniaturized antenna arrays using decoupling networks with realistic elements," *IEEE Trans. Microw. Theory Tech.*, vol. 54, no. 6, pp. 2733–2740, Jun. 2006.
- [11] W. P. Geren, C. R. Curry, and J. Andersen, "A practical technique for designing multiport coupling networks," *IEEE Trans. Microw. Theory Tech.*, vol. 44, no. 3, pp. 364–371, Mar. 1996.
- [12] S. C. Chen, Y. S. Wang, and S. J. Chung, "A decoupling technique for increasing the port isolation between two strongly coupled antennas," *IEEE Trans. Antennas Propag.*, vol. 56, no. 12, pp. 3650–3658, Dec. 2008.
- [13] X. Tang, K. Mouthaan, and J. C. Coetzee, "Flexible design of de-coupling and matching networks for two strongly coupled antennas," *Electron. Lett.*, vol. 49, no. 8, pp. 521–522, Apr. 2013.
- [14] K. Wang, L. Li, and T. F. Eibert, "Comparison of compact monopole antenna arrays with eigenmode excitation and multiport conjugate matching," *IEEE Trans. Antennas Propag.*, vol. 61, no. 8, pp. 4054–4062, Aug. 2013.
- [15] S. Dossche, S. Blanch, and J. Romeu, "Optimum antenna matching to minimise signal correlation on a two-port antenna diversity system," *Electron. Lett.*, vol. 40, no. 19, pp. 1164–1165, Sep. 2004.
- [16] M. A. Moharram and A. A. Kishk, "General decoupling network design between two coupled antennas for MIMO applications," *Prog. Electromagn. Res. Lett.*, vol. 37, pp. 133–142, 2013.
- [17] H. Li, X. Lin, B. K. Lau, and S. He, "Equivalent circuit based calculation of signal correlation in lossy MIMO antennas," *IEEE Trans. Antennas Propag.*, vol. 61, no. 10, pp. 5214–5222, Oct. 2013.
- [18] S. Blanch, J. Romeu, and I. Corbella, "Exact representation of antenna system diversity performance from input parameter description," *Electron. Lett.*, vol. 39, no. 9, pp. 705–707, May 2003.

A Low-Profile, Vertically Polarized Ultrawideband Antenna With Monopole-Like Radiation Characteristics

Kasra Ghaemi and Nader Behdad

Abstract—A compact, ultrawideband (UWB) antenna with an extremely low profile is presented. The antenna has consistent monopole-like radiation characteristics over approximately an 8.5:1 bandwidth. It consists of two radiators where one radiator is a smaller, slightly different version of the other one. The smaller radiator is partially embedded into the large one to avoid considerable increase in the maximum antenna height. Each radiator has two parallel loops in the shape of a bent diamond connected to the ground plane at their ends. A properly designed feed network is used to feed the larger antenna at lower frequencies while feeding the smaller one at higher frequencies to improve the consistency of the radiation characteristics of the system over a very broad bandwidth. A prototype of the proposed antenna and the feed network are fabricated and experimentally characterized. The fabricated antenna prototype has electrical dimensions of $0.26\lambda_{\min} \times 0.26\lambda_{\min} \times 0.046\lambda_{\min}$ at its lowest frequency of operation and demonstrates monopole-like radiation characteristics with consistent, vertically polarized, omni-directional radiation patterns over roughly an 8.5:1 (0.66–5.6 GHz) bandwidth.

Index Terms—Broadband antennas, electrically small antennas, omni-directional antennas, ultrawideband (UWB) antennas.

I. INTRODUCTION

HF, VHF, and UHF frequency bands have long been used for many military communications applications. Currently, monopole whip antennas used in conjunction with automatic antenna tuners are the primary available antenna options for such applications. Whip antennas, however, have high profiles (i.e., they stick out of the vehicles they are mounted on) and narrow bandwidths. The former is not desired in military systems, since it can give out the location of important assets, and the latter limits the utility of such antennas in wideband applications. Therefore, there is a significant need for developing low-profile and compact HF/VHF/UHF antennas capable of covering extremely broad bandwidths as replacements for current whip antenna technology.

Various techniques have been used in the past to design compact ultrawideband (UWB) antennas that radiate like vertically polarized monopoles. Multiresonant antennas composed of top-hat-loaded monopoles that incorporate various impedance-matching elements within the structure of the antenna were among the first such structures developed in this area [1], [2]. In [1], Goubau reports an antenna that achieves a bandwidth of about one octave while occupying a cylindrical volume with a diameter of $0.18\lambda_{\min}$ and a height of $0.065\lambda_{\min}$ (λ_{\min} is the free-space wavelength at the lowest frequency of operation). A somewhat different design was proposed by Friedman in [2], which achieves a bandwidth of an octave from a structure occupying the same volume. More recently, a low-profile antenna with an overall height of $0.065\lambda_{\min}$, composed of a conducting body of revolution and a shorted parasitic ring, was reported in [3]. In [4], a three-dimensional

Manuscript received October 03, 2014; revised February 28, 2015; accepted May 04, 2015. Date of publication May 07, 2015; date of current version July 31, 2015. This work was supported by the Office of Naval Research under ONR award No. N00014-11-1-0618.

The authors are with the Department of Electrical and Computer Engineering, University of Wisconsin-Madison, Madison, WI 53706-1691 USA (e-mail: ghaemi@wisc.edu; behdad@wisc.edu).

Color versions of one or more of the figures in this communication are available online at <http://ieeexplore.ieee.org>.

Digital Object Identifier 10.1109/TAP.2015.2430880

(3-D) UWB antenna composed of a hemispherical helix with a cone feed is reported. The antenna has a height of $0.125\lambda_{\min}$ and maximum lateral dimensions of $0.25\lambda_{\min}$ and achieves a bandwidth of 10:1. Compact antennas that use loops as the main radiating elements have also been examined [5]–[8]. In [5], a compact UWB antenna utilizing two coupled loops was demonstrated to achieve monopole-like radiation patterns over a very wide frequency band. Miniaturized versions of this antenna, which reduce the overall antenna height and its lateral dimensions, were later reported in [6] and [7].

The most significant challenge in designing compact UWB antennas is to reduce the lowest frequency of operation of the antenna without increasing its occupied volume. Once the maximum linear dimension of an antenna is reduced below $\lambda/4\pi$ (corresponding to $ka = 0.5$, where $k = 2\pi/\lambda$ is the wavenumber and a is the radius of the smallest sphere that circumscribes the antenna), the antenna becomes electrically small and its bandwidth reduces significantly. Many attempts have been made to design small antennas with bandwidths that approach the theoretical limits. A notable example is the design presented in [9] and a comprehensive list of such antennas is provided in [10]. UWB antenna designs with $ka < 0.5$ have also been reported [11]–[13]. However, these designs use either lossy ferrites [11] or resistive materials [12], [13] to load the antenna and achieve improved impedance matching at the lowest frequency of operation.

Recently, we reported a compact UWB antenna with a vertically polarized monopole-like radiation pattern [14]. This antenna has an extremely low overall height ($0.033\lambda_{\min}$) and its impedance matched over a bandwidth greater than 10:1, but it demonstrates consistent radiation characteristics over a 4:1 bandwidth. Specifically, the radiation patterns of the antenna start to deviate from the desired monopole-like omni-directional patterns at a frequency approximately four times its minimum frequency of operation. This change in the radiation patterns limits the bandwidth of this antenna. In this communication, we propose a new antenna, which takes advantage of the low-profile, broadband nature of the antenna proposed in [14] to achieve a low-profile antenna with an extremely broad operational bandwidth. The proposed antenna is composed of two radiating elements, where one element is a smaller, slightly modified version of the other. Each radiating element is based on the topology of the antenna discussed in [14]. The two elements are nested within each other to ensure that the antenna height and lateral dimensions are not increased significantly [15]. A frequency-dependent feed network feeds the appropriate radiating element based on the frequency of the excitation signal. Using this topology, a compact, low-profile UWB antenna with electrical dimensions of $0.26\lambda_{\min} \times 0.26\lambda_{\min} \times 0.046\lambda_{\min}$ is designed and fabricated. The antenna demonstrates consistent monopole-like radiation patterns over an 8.5:1 bandwidth. In what follows, the principles of operation of the proposed antenna along with the measurement results of a fabricated prototype are presented and discussed.

II. ANTENNA DESIGN

A. Principles of Operation

The antenna presented in [14] consists of two 3-D half-loops coupled to each other. Each half loop is in the shape of a bent-diamond and is fed at its center and short-circuited to the ground at its end. The two loops are fed in parallel at their common feeding point and a common top hat is used to cover both structures to reduce the lowest frequency of operation of the antenna. The antenna shows a good impedance match over an extremely wide bandwidth (in excess of 10:1) [14]. However, its bandwidth is limited by the deterioration of the radiation patterns of the antenna at higher frequencies. Specifically, the antenna shows consistent, monopole-like, omni-directional radiation

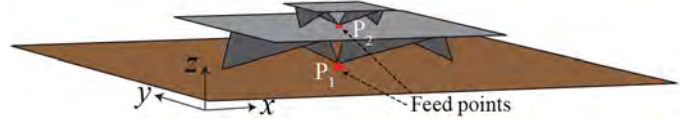


Fig. 1. 3-D topology of an antenna composed of two similar radiators with different sizes, which is capable of providing consistent, monopole-like radiation patterns over an extremely broad bandwidth.

patterns only over a 4:1 bandwidth. As frequency increases, the electrical dimensions of the antenna increase too and the phase differences between the electric currents flowing on different parts of the antenna increase. Thus, the radiated fields emanating from different locations on the antenna add constructively and destructively at different directions. This deteriorates the omni-directionality of the antenna and effectively limits its operating bandwidth.

To develop an UWB antenna with consistent radiation characteristics over an extremely wide bandwidth, we use the antenna introduced in [14] as a building block and improve the consistency of its radiation patterns. This can be accomplished by reducing the effective radiation zone of the antenna as frequency increases. One method for accomplishing this is shown in Fig. 1, where a smaller and slightly modified version of the original antenna is mounted on top of the top hat of the larger antenna. In this arrangement, the smaller antenna is designed such that it has a lowest frequency of operation that approximately coincides with the highest frequency of operation of the larger antenna. In this case, the highest operating frequency of the larger antenna is determined by the maximum frequency at which the radiation patterns of the larger antenna remain acceptable. The antenna arrangement shown in Fig. 1 can be fed with a frequency-dependent feed network that automatically feeds the correct antenna based on the frequency of the excitation signal. When fed in this manner, the structure acts as a single antenna with an extremely broad bandwidth.

While the structure shown in Fig. 1 can operate over a larger bandwidth compared to a single-element antenna, its height is increased compared to the single-element antenna of [14]. This becomes an issue if this type of antenna is to be used for relatively low-frequency applications (e.g., upper HF and the lower VHF bands). To circumvent this problem, we first examine the electric field distribution in the near-field region of the antenna. Fig. 2(a) and (b) shows the electric field distribution in the near-field region of the antenna proposed in [14] in the x - z and y - z planes, respectively. As can be observed, the intensity of the electric field in the central region of the antenna (marked “field free”) is significantly smaller than the field intensity in the other regions. A similar behavior is also observed for the magnetic field intensity in this region (for brevity, the field distributions are not shown.) Therefore, if the central part of the antenna’s top hat is modified in this region, the response of the structure is not expected to change significantly. Specifically, the topology of the antenna shown in Fig. 1 can be modified and the smaller antenna can be partially embedded in the larger antenna as shown in Fig. 3. In this arrangement, the top hat of the larger antenna is modified to create an open top cavity in its field free region. Fig. 2(c) and (d) shows the electric field distribution in the near field of the larger antenna with the modified top hat in the x - z and y - z planes, respectively. As seen, the intensity of the electric field in the region marked “field free” (below the top hat) is still considerably smaller compared to the surrounding regions. Using the antenna topology shown in Fig. 3, the overall height of the antenna shown in Fig. 1 can be reduced while achieving the desired broadband operation.

To examine the impact of the cavity height on the performances of both antennas, a prototype of the structure shown in Fig. 3 is simulated in CST Microwave Studio. The dimensions of the larger antenna in this prototype are $12.1 \text{ cm} \times 12.1 \text{ cm} \times 1.8 \text{ cm}$ and that of the smaller

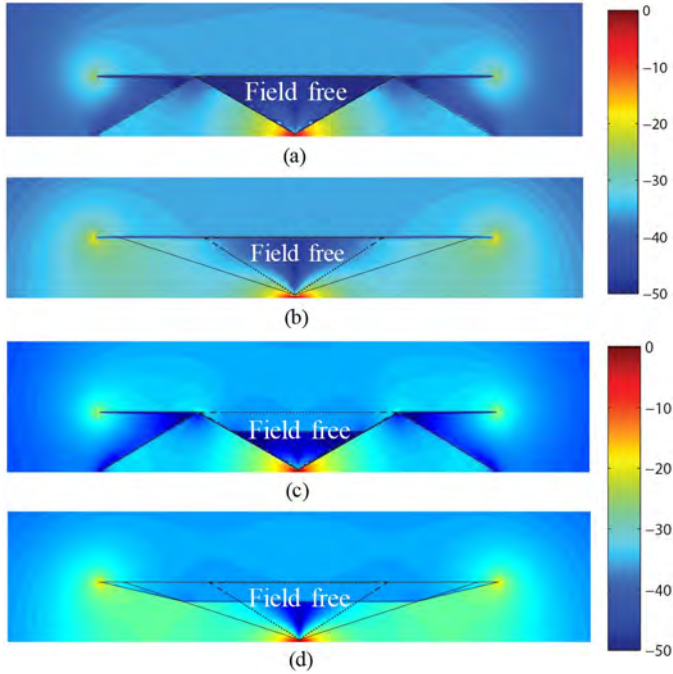


Fig. 2. Normalized electric field distribution of the larger antenna shown in Fig. 1 at 1.0 GHz in the (a) x - z plane and (b) y - z plane. (c) and (d) Normalized electric field distribution, at 1 GHz, of the large antenna when its top hat is modified to create an open top cavity: x - z plane and y - z plane.

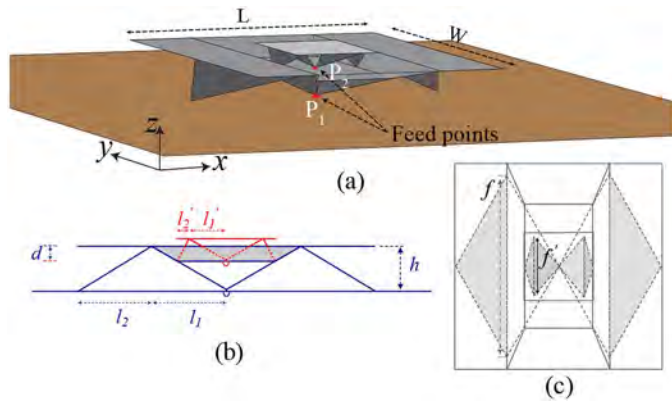


Fig. 3. (a) 3-D topology of the proposed antenna. (b) Side view. (c) Top view. The parameters labeled are as follows: $l_1 = 30.2$, $l_2 = 30.2$, $l'_1 = 15.1$, $l'_2 = 4.5$, $f = 109$, $f' = 36.3$, $d = 6$, $W = 121$. The values are in mm.

antenna are $4 \text{ cm} \times 4 \text{ cm} \times 0.9 \text{ cm}$. Other significant geometrical parameters of the antennas are presented in the caption of Fig. 3. These dimensions are obtained following the design procedure reported in [14] and are chosen, so that the larger and smaller antennas have lowest frequencies of operation of 0.6 and 2 GHz, respectively. This frequency range is chosen for our experimental studies because the lowest frequency of operation of our antenna characterization system is 0.6 GHz. Fig. 4(a) and (b) shows the impact of the cavity depth d on the input VSWRs of both antennas. In these simulations, each antenna is fed with a lumped port at its feed location. As can be observed from Fig. 4(a), changing the cavity depth does impact the VSWR of the larger antenna. However, the most significant variations are observed at frequencies above 4 GHz, which fall outside of the (omni-directional) bandwidth of this antenna. Particularly, the cavity depth does not significantly impact the VSWR of the larger antenna below 4.0 GHz for

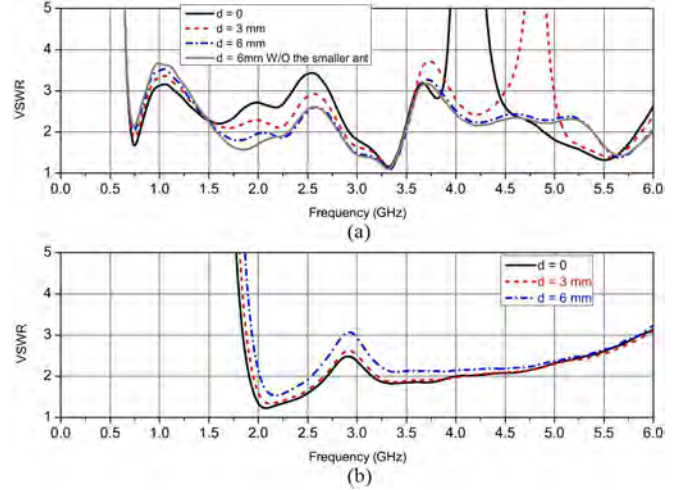


Fig. 4. VSWRs of the (a) large and (b) small antennas shown in Fig. 3 for different cavity depths.

cavity depths as large as 6 mm. This figure also shows the effect of the presence of the smaller antenna in the top cavity (for $d = 6 \text{ mm}$) on the input VSWR of the larger antenna. Fig. 4(b) shows that increasing the cavity depth slightly deteriorates the VSWR of the smaller antenna, particularly in the frequency band of 2.5–3 GHz. Based on the results shown in Fig. 4, it appears that choosing a cavity depth of $d = 6 \text{ mm}$ offers a good compromise between the height and impedance matching.

B. Feed Network Design

To work as a single, ultra-broadband radiator, the antenna shown in Fig. 3 uses a frequency-dependent feed network that feeds the appropriate radiating structure based on the frequency of the input signal. This can be accomplished using a diplexer and a simple power divider as shown in Fig. 5(a). This feed network consists of a main $50\text{-}\Omega$ line, a T-junction, and a highpass and a lowpass filter. The circuit models of the lowpass and highpass filters used in this feed network are shown in Fig. 5(b) and (c), respectively. The lowpass filter and the highpass filter have second-order responses. This feed arrangement ensures that each antenna is only excited in the desired frequency band of operation. To feed the smaller antenna in practice, a coaxial cable is used. This cable passes through the ground plane of the larger antenna and its top hat to arrive at the input terminals of the smaller structure. Since this cable passes through the near-field of the larger antenna, it impacts the impedance matching of that antenna slightly. As a result, a series capacitor is used at the terminals of the larger antenna to help improve the overall VSWR of the structure [see Fig. 5(a)].

The larger antenna loses its omni-directionality at approximately 2 GHz, whereas the smaller antenna starts to radiate efficiently at around this frequency. The lumped element values of the various components of the feed network are chosen in a manner to achieve a diplexer cutoff frequency of around 2 GHz and a good impedance match at the input port of the feed network. The values of the lumped element inductors and capacitors used in the design of this feed network are reported in the caption of Fig. 5. The response of the diplexer is simulated in Agilent's Advanced Design System (ADS) and the results are presented in Fig. 5(d).

To predict the response of the antenna shown in Fig. 3 with its feed network [shown in Fig. 5(a)], the antenna is first simulated in CST Microwave Studio including the coaxial cable that feeds the smaller antenna. The physical parameters of this antenna are shown in the

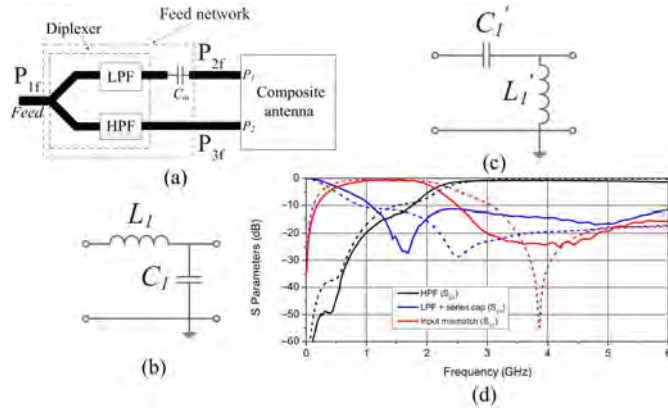


Fig. 5. (a) Topology of the frequency-dependent feed network used to feed the composite two-element antenna shown in Fig. 3. The antenna is represented with the two-port network. The feed network is composed of a diplexer in conjunction with a series capacitor. (b) Circuit model of the low-pass filter used in the diplexer. (c) Circuit model of the high-pass filter used in the diplexer. (d) Frequency responses of the diplexer. Dashed and solid lines correspond to diplexers' responses designed for the simulated and the fabricated antenna prototype, respectively. The values of the lumped elements used in the simulated (fabricated) feed network are as follows: $L_1 = 4$ (3.3), $L_1' = 1.2$ (1.6). These values are in nH. $C_1 = 0.85$ (1), $C_1' = 0.9$ (0.7), and $C_m = 4.4$ (3.3). These values are in pF.

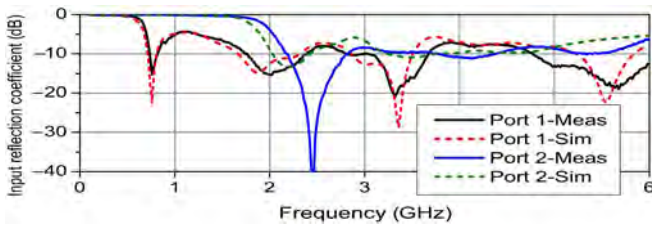


Fig. 6. Simulated and measured input reflection coefficients of the two-port antenna.

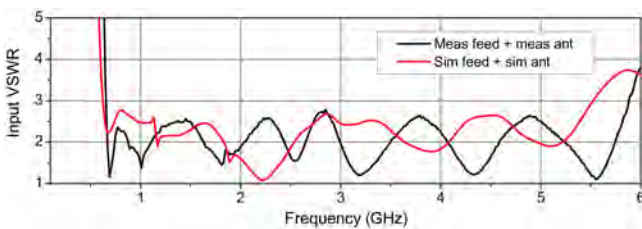


Fig. 7. Simulated and measured input VSWRs of the antenna.

caption of Fig. 3. The input reflection coefficients of each antenna simulated in CST Microwave Studio are shown in Fig. 6. The simulated two-port S-parameters of the antenna are then exported to the circuit simulation software Agilent ADS and the response of the antenna with the feed network is calculated using circuit-based simulations in ADS. In these combined full-wave/circuit simulations, the effects of the frequency-dependent variations of the input impedances of the antennas as well as those of the feed network are all taken into account. Fig. 7 shows the simulated input VSWR of the antenna, as seen from the input port of the feed network. As can be observed, the responses of the two antennas can be combined successfully. Based on these simulation results, the antenna is expected to have a VSWR below 2.7 from 0.66 to 5.4 GHz.

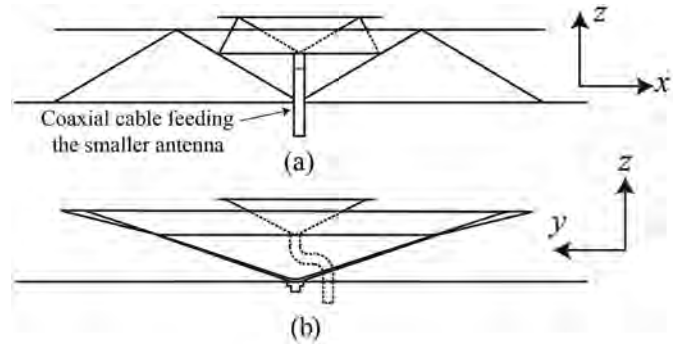


Fig. 8. (a) and (b) Topology of the fabricated prototype showing the SMA connector used to feed the larger antenna and the semirigid coaxial cable feeding the smaller antenna. (a) $x-z$ plane. (b) $y-z$ plane.

III. MEASUREMENT RESULTS AND DISCUSSION

The antenna was fabricated. The fabricated prototype is mounted on a circular ground plane with a radius of 35 cm. The larger antenna is fed with an SMA connector at the center. The smaller antenna is fed with a semirigid coaxial cable that passes through a hole drilled in the metallic ground plane of the larger antenna. This hole is 8.4 mm off center (along the negative y -axis direction) with respect to the feed point of the larger antenna. This offset is required to avoid the SMA connector feeding the larger antenna, which is located at the center of the ground plane. Above the ground plane, an S-shaped bend is created in this semirigid coaxial cable to feed the smaller antenna at the center feed location. The outer conductor of this cable is connected to the top hat of the larger antenna and its center conductor is connected to the feed point of the smaller antenna. The outer shield of this semirigid coaxial cable is electrically connected to the ground plane of the larger antenna at the location where it passes through this ground plane. This is done to ensure that any current that may be induced on the outer surface of the outer shield of this cable (by the larger antenna) is simply shorted to the ground and does not flow along the feeding cable. The presence of this semirigid feeding coaxial cable in the near-field of the larger antenna does not significantly impact its performance. This is due to the fact that the region where this cable is placed in the "field free" region of the larger antenna as shown in Fig. 2(c) and (d). Moreover, the fact that this cable short circuits the top hat of the larger antenna to ground at this location also does not impact the response of the larger antenna since the center part of the top hat of the larger antenna is a virtual ground point. Fig. 8(a) and (b) shows a detailed drawing of the feeding mechanism of the antenna in the $x-z$ and $y-z$ planes, respectively.

The S-parameters of the prototype are measured using a vector network analyzer. Fig. 6 shows a comparison between the measured and the simulated input reflection coefficients of the two antennas. In general, there is a very good agreement between the simulation and the measurement results at low frequencies (i.e., for the larger antenna). This is due to the fact that at these frequencies, the wavelength is large. Therefore, the inevitable variations that exist (due to fabrication errors) between the exact dimensions of the fabricated antenna and those of the simulated one are only a small fraction of the wavelength and do not significantly impact the measurement results. As frequency increases, however, these small variations become more significant as evidenced by the deterioration of the agreement between the measured and simulated results seen in Fig. 6. There is also a generally good agreement at higher frequencies which can be seen in Fig. 6 other than a slight frequency shift in the second resonance of the second port's measured input impedance compared to the simulated one.

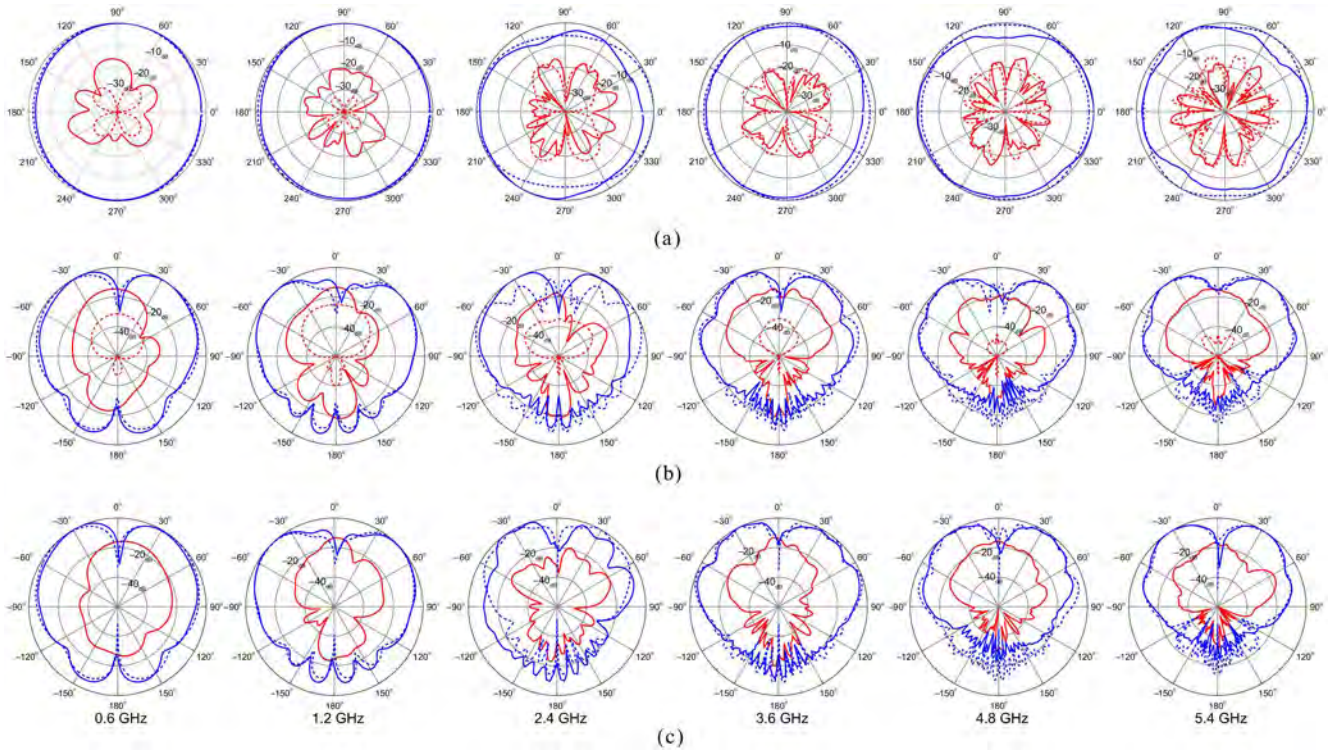


Fig. 9. Measured and simulated radiation patterns of the antenna in the (a) azimuth (x - y); (b) elevation (x - z); and (c) elevation (y - z) planes. Blue solid line is the measured co-pol (E_θ) component. Blue dashed line is simulated co-pol (E_θ) component. Red solid line is measured cross-pol (E_ϕ) component. Red dashed line is simulated cross-pol (E_ϕ) component.

The feed network discussed in Section II-B was also fabricated and the response of the antenna and the feed network together were measured. To compensate for the slight discrepancies observed between the measurement and simulation results observed in Fig. 6, the element values of the fabricated feed network are slightly different. These new feed network element values are reported in the caption of Fig. 5. The measured response of the fabricated feed network is shown in Fig. 5(d). As seen, the cutoff frequency of this diplexer is also around 2 GHz. The measured input VSWR of the antenna as seen from the input terminal of the feed network is presented in Fig. 7 along with the simulation results. As can be observed, the fabricated antenna demonstrates a VSWR below 2.7:1 over the frequency range 0.66–5.9 GHz. The discrepancies between the measured and the simulated responses are attributed to fabrication tolerances (specifically those of the 3-D loops), the uncertainties in modeling the through-hole vias, SMA connectors, and the feeding cable (of the smaller antenna), as well as the tolerances in the values of the capacitors, inductors, and dielectric constant of the substrate of the feed network.

The radiation parameters of the fabricated antenna with its feed network were measured using a multiprobe spherical near-field measurement system. The measurement process is carried out over the frequency range 0.6–6 GHz. Fig. 9(a)–(c) shows the measured radiation patterns of the fabricated antenna system along with the simulated results for different frequencies. Fig. 9(a) shows the measured radiation pattern of the antenna in the azimuth plane (x – y plane). The results for both the co- and cross-polarized components of the radiated fields are presented. The antenna shows relatively low cross-polarization levels across its entire band of operation. As can be observed, unlike the structure reported in [14], this antenna maintains its omni-directionality over an extremely broad bandwidth starting from 0.6 GHz to approximately 5.6 GHz. Fig. 9(b) and (c) shows the measured and the simulated radiation patterns of the antenna in two

elevation planes (x - z and y - z planes). Observe that despite the fact that the antenna is not rotationally symmetric, it demonstrates similar radiation patterns in both elevation planes. Moreover, the radiation patterns of the antenna in these two planes are similar to those of a monopole antenna with a finite ground plane size. Similar to the previous case, a good agreement between the measured and the simulated results and relatively low levels of cross-polarized radiation are also observed in these results. There is no cross-polarized radiation in the y - z plane of simulation results because the simulated structure is perfectly symmetric with respect to this plane while such an exact symmetry does not exist in the fabricated prototype due to fabrication errors resulting in the presence of low cross-polarization levels in measurement results.

This antenna radiates similar to a monopole antenna placed on a finite ground plane. In such antennas, as long as the ground plane dimensions are larger than approximately half a wavelength, the ground plane size will not significantly affect the input VSWR of the antenna. In such structures, the ground plane dimensions primarily impact the shape of the radiation patterns of the antenna. A larger ground plane reduces the radiation toward the lower hemisphere and slightly increases the gain and directivity of the antenna. Moreover, using a larger ground plane is beneficial in reducing the cross-polarization levels of the antenna. This is due to the fact that the magnitudes of the horizontal currents excited on the edges of the finite ground plane decrease as the ground plane size increases. Since the proposed antenna is expected to be mounted on top of a metallic vehicle, the assumption of having a large enough ground plane is expected to be valid in practice.

The realized gain of the antenna system as well as its total efficiency is also measured using the spherical near field measurement system and the results are presented in Fig. 10. The realized gain of the antenna takes into account the effect of impedance mismatch as

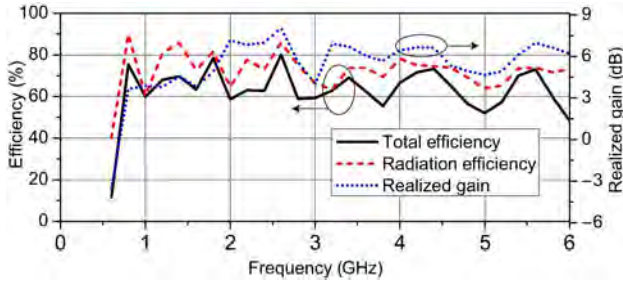


Fig. 10. Measured realized gain, total, and radiation efficiency of the antenna.

TABLE I
COMPARISON OF THE PERFORMANCE OF THE PROPOSED ANTENNA WITH
A REPRESENTATIVE SAMPLE OF THE CURRENT STATE-OF-THE-ART IN
LOW-PROFILE, VERTICALLY POLARIZED, UWB ANTENNAS WITH
MONOPOLE-LIKE RADIATION CHARACTERISTICS

Group	$H(\lambda_{min})$	$L(\lambda_{min})$	$W(\lambda_{min})$	BW
[16]	0.065	0.18	0.18	1.9:1
[4]	0.125	0.25	0.25	10:1
[9]	0.077	0.154	0.154	1.2:1
[3]	0.065	0.264	0.264	4:1*
[7]	0.053	0.36	0.36	4:1*
[17]	0.1	0.4	0.4	10:1
[8]	0.06	0.2	0.2	1.46:1
[18]	0.085	0.189	0.189	5.5:1
[19]	0.088	0.15	0.15	4:1*
[14]	0.033	0.24	0.24	4:1
This work	0.046	0.26	0.26	8.5:1

*denotes for the reported bandwidth.

well as the ohmic losses in the antenna structure and the fabricated feed network. As can be observed, over most of its operating band, the antenna demonstrates a gain higher than 4.0 dBi. Similar to the realized gain results, the total antenna efficiency takes ohmic losses, impedance mismatch, and the feed network losses into account. As can be observed, the total antenna efficiency remains above 60% over most of the antenna's frequency band of operation while radiation efficiency is mostly over 70%. Table I provides a comparison between the performance of this antenna with the current state-of-the-art in vertically polarized, ultra-broadband antennas with monopole-like radiation characteristics. To allow for a fair comparison of the performances of the different antennas reported in this table, the bandwidth of each antenna is calculated by determining the frequency range over which the input VSWR is better than 3:1 and the antenna maintains an omni-directional radiation pattern. As can be observed, the proposed antenna has one of the lowest overall heights among the state-of-the-art compact, vertically polarized UWB antennas reported to date.

IV. CONCLUSION

A UWB antenna with an extremely low-profile and consistent monopole-like radiation patterns was presented and discussed in this communication. The antenna takes advantage of two important properties of a recently reported UWB antenna [14]. These include the extremely low-profile nature of this design and a relatively large field-free region within the center of the volume of this antenna. The latter property was exploited in this work to place a smaller, slightly modified version of this antenna within its interior field-free region. The smaller antenna operates at a higher frequency than the larger antenna. A frequency-dependent feed network was used to feed each antenna only in the frequency range where it radiates omni-directionally. This way, a single radiator capable of

providing consistent monopole-like radiation characteristics over an extremely broad bandwidth was obtained. The antenna's electrical dimensions at its lowest frequency of operation are $0.26\lambda_{min} \times 0.26\lambda_{min} \times 0.046\lambda_{min}$. The antenna shows a VSWR better than 2.7:1 and monopole-like radiation characteristics over approximately an 8.5:1 bandwidth. The structure has a total efficiency better than 60% over its entire band of operation. The proposed antenna is expected to be particularly useful for military communication systems operating at the upper end of the HF band, the entire VHF band, and the lower end of the UHF frequency bands where currently high-profile, monopole whip antennas are widely used. In such applications, low-profile, wide-band antennas capable of providing VSWRs better than 3:1 are highly sought. Using the concept proposed in this communication offers a practical means of achieving vertically polarized monopole-like radiation from a structure that has a significantly lower overall profile and an extremely larger bandwidth than a conventional monopole whip antenna and does not need automatic impedance tuners to operate over a wide bandwidth.

REFERENCES

- [1] G. Goubau, N. N. Puri, and F. Schwing, "Diakoptic theory for multielement antennas," *IEEE Trans. Antennas Propag.*, vol. 30, no. 1, pp. 15–26, Jan. 1982.
- [2] C. H. Friedman, "Wide-band matching of a small disk-loaded monopole," *IEEE Trans. Antennas Propag.*, vol. 33, no. 10, pp. 1142–1148, Oct. 1985.
- [3] H. Nakano, H. Iwaoka, K. Morishita, and J. Yamauchi, "A wideband low-profile antenna composed of a conducting body of revolution and a shorted parasitic ring," *IEEE Trans. Antennas Propag.*, vol. 56, no. 4, pp. 1187–1192, Apr. 2008.
- [4] T. Yang, W. A. Davis, and W. L. Stutzman, "The design of ultra-wideband antennas with performance close to the fundamental limit," in *Proc. URSI General Assembly*, Chicago, IL, 2008, p. 234.
- [5] N. Behdad and K. Sarabandi, "A compact antenna for ultrawide-band applications," *IEEE Trans. Antennas Propag.*, vol. 53, no. 7, pp. 2185–2192, Jul. 2005.
- [6] N. Behdad, M. Al-Joumayly, and M. Salehi, "Ultra-wideband low profile antenna," U.S. Patent 8,228,251, Jul. 24, 2012.
- [7] A. Elsherbini and K. Sarabandi, "Very low-profile top-loaded UWB coupled sectorial loops antenna," *IEEE Antennas Wireless Propag. Lett.*, vol. 10, pp. 800–803, Aug. 2011.
- [8] O. Jungsuek and K. Sarabandi, "Low profile vertically polarized omnidirectional wideband antenna with capacitively coupled parasitic elements," *IEEE Trans. Antennas Propag.*, vol. 62, pp. 977–982, Feb. 2014.
- [9] H. R. Stuart and S. R. Best, "A small wideband multimode antenna," in *Proc. Int. Symp. Antennas Propag. Soc. (IEEE AP-S'08)*, 2008, pp. 1–4.
- [10] D. F. Sievenpiper *et al.*, "Experimental validation of performance limits and design guidelines for small antennas," *IEEE Trans. Antennas Propag.*, vol. 60, pp. 8–19, Jan. 2012.
- [11] H. Moon, G.-Y. Lee, C.-C. Chen, and J. L. Volakis, "An extremely low-profile ferrite-loaded wideband VHF antenna design," *IEEE Antennas Wireless Propag. Lett.*, vol. 11, pp. 322–325, Mar. 2012.
- [12] S. Palud, F. Colombel, M. Himdi, and C. L. Meins, "Wideband omnidirectional and compact antenna for VHF/UHF band," *IEEE Antennas Wireless Propag. Lett.*, vol. 10, pp. 3–6, Jan. 2011.
- [13] Y. K. Yu and J. Li, "Analysis of electrically small size conical antennas," *Prog. Electromagn. Res. Lett.*, vol. 1, pp. 85–92, 2008.
- [14] N. Behdad, M. Li, and Y. Yusuf, "A very low-profile, omnidirectional, ultrawideband antenna," *IEEE Antennas Wireless Propag. Lett.*, vol. 12, pp. 280–283, Feb. 2013.
- [15] K. Ghaemi and N. Behdad, "A low-profile, vertically-polarized, compact, ultra-wideband antenna with a 10:1 bandwidth," in *Proc. Int. Symp. Antennas Propag. Soc. (APSURSI)*, 2014, pp. 203–204.
- [16] G. Goubau and F. Schwing, "Multi-Element Monopole Antennas," in *Proc. ECOM-ARO Workshop Elect. Small Antennas*, U.S. Army Electronics Command, Fort Monmouth, NJ, USA, 1976, pp. 63–68.
- [17] Z. Jing, D. Psychoudakis, C.-C. Chen, and J. L. Volakis, "Design optimization of a low-profile UWB body-of-revolution monopole antenna," *IEEE Trans. Antennas Propag.*, vol. 60, no. 12, pp. 5578–5586, Dec. 2012.

- [18] S. Abadi and N. Behdad, "An electrically small, vertically polarized ultrawideband antenna with monopole-like radiation characteristics," *IEEE Antennas Wireless Propag. Lett.*, vol. 13, pp. 742–745, Apr. 2014.
- [19] M. Koohestani, J.-F. Zurcher, A. Moreira, and A. K. Skrivervik, "A novel, low-profile, vertically-polarized UWB antenna for WBAN," *IEEE Trans. Antennas Propag.*, vol. 62, no. 4, pp. 1888–1894, Apr. 2014.

Parallel Marching-on-in-Degree Solver of Time-Domain Combined Field Integral Equation for Bodies of Revolution Accelerated by MLACA

Z. He, H. H. Zhang, and R. S. Chen

Abstract—Time-domain combined field integral equation (TD-CFIE) for bodies of revolution (BORs) is solved by marching-on-in-degree (MOD) method. A multilevel partitioning is adopted to group the spatial basis functions along the longitudinal dimension. The interactions of the adjacent groups are calculated directly in the traditional manner, while the impedance matrices associated with the well-separated groups at each level are computed by the multilevel adaptive cross approximation (MLACA) algorithm. The hybrid MPI and OpenMP parallel programming technique is utilized to further accelerate the solving process on a shared-memory computer system. Two numerical results demonstrate that the proposed method can greatly reduce the memory requirement and CPU time, thus enhance the capability of MOD method.

Index Terms—Body of revolution (BOR), marching-on-in-degree (MOD) method, MPI, multilevel adaptive cross approximation (MLACA) algorithm, OpenMP, time-domain combined field integral equation (TD-CFIE).

I. INTRODUCTION

In the area of computational electromagnetics, scattering from bodies of revolution (BORs) such as spheres, cylinders, and ellipsoids are often used as benchmark targets to validate new methods. Meanwhile, many real-world objects such as warhead, radome, and reflector antenna are also BORs. Therefore, the scattering analysis of BORs is very useful and important. Due to their rotationally symmetrical property, the integral equation can be discretized by using basis functions defined on the boundary curve and Fourier series in the azimuthal direction. Since different Fourier modes are independent, only a small matrix equation needs to be solved for each Fourier mode, which can reduce both the memory requirement and the CPU time greatly [1]–[3].

Manuscript received October 22, 2014; revised May 03, 2015; accepted May 04, 2015. Date of publication May 07, 2015; date of current version July 31, 2015. This work was supported in part by the National Natural Science Foundation of China under Grant 61431006 and Grant 61171041, in part by the Jiangsu Natural Science Foundation under Grant BK2012034, and in part by the Ph.D. Programs Foundation of Ministry of Education of China under Grant 20123219110018.

The authors are with the Department of Communication Engineering, Nanjing University of Science and Technology, Nanjing 210094, China (e-mail: eerschen@njust.edu.cn).

Color versions of one or more of the figures in this communication are available online at <http://ieeexplore.ieee.org>.

Digital Object Identifier 10.1109/TAP.2015.2430879

The time-domain integral equation (TDIE) has been widely used to analyze many practical transient electromagnetic scattering problems in the past decades. There are two solution schemes for the transient electromagnetic scattering analysis, namely the marching-on-in-time (MOT) method [4], [5] and marching-on-in-degree (MOD) method [6]–[8]. However, for BORs, the MOT method cannot make use of the axial symmetry of them since the subdomain temporal basis functions are adopted [9]. The MOD method does not have this limitation because the weighted Laguerre polynomials are used as the global temporal basis functions. Originally, the MOD solver of time-domain magnetic field integral equation (TD-MFIE) is proposed for the transient electromagnetic scattering analysis of closed BORs [10]. In this communication, we presented the MOD solver of time-domain combined field integral equation (TD-CFIE) for BORs.

Since the impedance matrices of each Fourier mode are dense matrices in the MOD solver of TD-CFIE for BORs, the matrix filling time, memory requirement, and matrix–vector multiplication operations are of $O(N_s^2)$ complexity, where N_s is the number of spatial unknowns for each mode. In other words, the MOD solver of TDIE calls for very high computational cost and memory requirement for large-scale scattering problems. As a result, many fast algorithms based on the MOD solver of TDIE method have been applied to overcome this difficulty to some reasonable extent in recent years. For example, the fast Fourier transform (FFT) [11], the UV method [12], the adaptive cross approximate (ACA) algorithm [13], and so on. By using these fast algorithms, the computational complexity can be reduced for the analysis of transient electromagnetic scattering problems. The multilevel adaptive cross approximation (MLACA) algorithm has been applied to the MOD solver of TDIE to accelerate matrix–vector product and reduce the memory requirement in [13]. The MLACA algorithm is a purely algebraic and kernel independent algorithm [14]. In this communication, the MLACA algorithm is utilized to speed up the transient electromagnetic scattering analysis of BORs. Moreover, the hybrid MPI and OpenMP parallel programming technique is adopted to further accelerate the solving process on a shared-memory computer system.

The remainder of this communication is organized as follows. Section II gives a detailed introduction of the proposed method. Two numerical results are presented to demonstrate the accuracy and efficiency of the proposed method in Section III. At last, the conclusion is given in Section IV.

II. THEORY AND FORMULATION

A. MOD Solver of TDIE for BORs

Considering that a PEC BOR is illuminated by a transient electromagnetic field $\{\mathbf{E}^i(\mathbf{r}, \tau), \mathbf{H}^i(\mathbf{r}, \tau)\}$ in free space, as shown in Fig. 1. The TD-EFIE and the TD-MFIE can be written as follows, respectively,

$$\begin{aligned} \hat{\mathbf{n}} \times \hat{\mathbf{n}} \times \mathbf{E}^i(\mathbf{r}, \tau) &= \hat{\mathbf{n}} \times \hat{\mathbf{n}} \times \frac{\mu_0}{4\pi} \frac{\partial}{\partial t} \int_S \frac{\mathbf{J}(\mathbf{r}', \tau - R/c)}{R} dS' \\ &\quad - \hat{\mathbf{n}} \times \hat{\mathbf{n}} \times \frac{\nabla}{4\pi\epsilon_0} \int_S \int_{-\infty}^{\tau - R/c} \frac{\nabla' \cdot \mathbf{J}(\mathbf{r}', \tau)}{R} d\tau dS' \end{aligned} \quad (1)$$

$$\hat{\mathbf{n}} \times \mathbf{H}^i(\mathbf{r}, \tau) = \frac{\mathbf{J}(\mathbf{r}, \tau)}{2} - \hat{\mathbf{n}} \times \nabla \times \int_{S_0} \frac{\mathbf{J}(\mathbf{r}', \tau - R/c)}{4\pi R} dS' \quad (2)$$

An Electrically Small, Vertically Polarized Ultrawideband Antenna With Monopole-Like Radiation Characteristics

Seyed Mohamad Amin Momeni Hasan Abadi, *Student Member, IEEE*, and Nader Behdad, *Senior Member, IEEE*

Abstract—We present an electrically small, low-profile, ultrawideband (UWB) antenna with monopole-like radiation characteristics. The antenna is composed of a monopole bow-tie antenna reactively loaded with a cascaded system of top hats, two shorting arms, and a ring slot cut into the ground plane. The reactive loads are used to introduce two additional resonances close to each other and below the lowest resonant frequency of the bow-tie. This results in a very compact, ultrawideband antenna that utilizes the available volume inside the Chu's sphere rather efficiently. At the lowest frequency of operation, the proposed antenna has electrical dimensions of $0.085\lambda_{\min} \times 0.189\lambda_{\min} \times 0.189\lambda_{\min}$, where λ_{\min} is the free-space wavelength. The antenna demonstrates a VSWR of 2.2:1 and consistent monopole-like, omnidirectional radiation patterns over a 5.5:1 bandwidth. A prototype of the antenna, which operates in the 0.6–3.2-GHz band, is fabricated and characterized using a multiprobe spherical near-field system.

Index Terms—Electrically small antennas, omnidirectional antennas, ultrawideband antennas.

I. INTRODUCTION

VERTICALLY polarized antennas with omnidirectional radiation characteristics have been studied widely in the past. These antennas are commonly used for many communications applications, particularly military communications at the HF, VHF, and UHF frequency bands. In such applications, physically large monopole (whip) antennas are widely used. However, such monopole antennas suffer from a number of practical challenges. First, to radiate efficiently, monopole antennas need to be at least a quarter of a wavelength long. Therefore, it is not uncommon to see several-meters-long whip antennas used at HF and VHF frequency bands. Such physically large antenna dimensions present numerous practical and security challenges in these systems. Second, whip antennas tend to be narrowband and seldom can they cover the entire HF or VHF band without the use of external antenna tuners. This limits the application of such antennas in radio systems that exploit waveforms with instantaneously wide bandwidths. Therefore, compact ultrawideband (UWB) antennas that radiate like vertically polar-

TABLE I
COMPARISON BETWEEN THE PERFORMANCE OF THE ANTENNA
REPORTED IN THIS WORK AND A FEW OTHER COMPACT
UWB ANTENNAS REPORTED IN THE LITERATURE

Ref. Work	H/λ_{\min}	L/λ_{\min}	W/λ_{\min}	BW	ka
[2]	0.125	0.250	0.250	10:1	0.785
[3]	0.078	0.156	0.156	1.2:1	0.491
[4]	0.100	0.400	0.400	10:1	1.427
[5]	0.065	0.180	0.180	1.9:1	0.898
[6]	0.071	0.284	0.284	4:1	1.338
[7]	0.053	0.360	0.360	4:1	1.634
[8]	0.065	0.200	0.200	1.5:1	0.978
[9]	0.033	0.240	0.240	4:1	1.085
Present work	0.085	0.189	0.189	5.5:1	0.803

ized monopoles but can cover an extremely large instantaneous bandwidths are desired.

A number of previous studies have been conducted in this area. Resistive loading of the antenna has been used to improve the impedance matching, and thereby enhancing the realized gain, of the antenna at its lowest frequency of operation [1]. This, however, adversely affects the radiation efficiency and performance of the structure at higher frequencies. Other approaches have relied on using the available volume of the antenna (e.g., the volume interior to Chu's sphere) efficiently [2]–[4] or using multimode resonant structures within the confines of the available antenna volume [5]–[8].

An important goal in designing a compact UWB antenna is to obtain the widest possible bandwidth with the lowest $ka = (2\pi/\lambda)a$ value at the lowest frequency of operation of the antenna (a is the radius of the smallest sphere circumscribing the antenna [10]). In this letter, we present an electrically small UWB antenna. The antenna is composed of a bow-tie structure, a cascaded system of top hats, two shorting arms, and a ring slot cut into the ground plane. The antenna's electrical dimensions are $0.085\lambda_{\min} \times 0.189\lambda_{\min} \times 0.189\lambda_{\min}$ at its lowest frequency of operation. A prototype of the proposed antenna is also fabricated and achieves a VSWR of 2.2:1 over an extremely broad frequency band. The antenna also demonstrates monopole-like frequency radiation patterns over a bandwidth that exceeds 5.5:1. Table I presents a comparison between the performance of the proposed antenna and some of the other top performing compact broadband antennas reported in the literature.

II. PRINCIPLES OF OPERATION

Fig. 1(a) and (b) shows the three-dimensional and the top views of the proposed antenna, respectively. The antenna is

Manuscript received January 16, 2014; revised March 11, 2014; accepted March 31, 2014. Date of publication April 04, 2014; date of current version April 23, 2014. This material is based upon work supported by the Office of Naval Research under ONR Award No. N00014-11-1-0618.

The authors are with the Department of Electrical and Computer Engineering, University of Wisconsin–Madison, Madison, WI 53706-1691 USA (e-mail: momenihassana@wisc.edu; behdad@wisc.edu).

Color versions of one or more of the figures in this letter are available online at <http://ieeexplore.ieee.org>.

Digital Object Identifier 10.1109/LAWP.2014.2315816

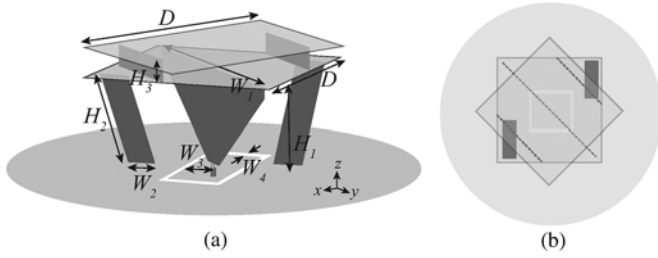


Fig. 1. (a) Three-dimensional topology of the proposed UWB antenna. (b) Top view of the structure.

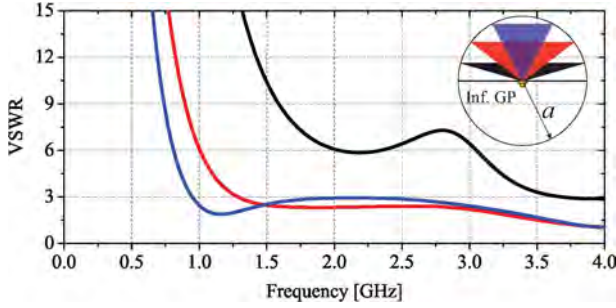


Fig. 2. Comparison of the VSWRs of a number of different bow-tie antennas that fit within a sphere with fixed radius of $a = 58$ mm. For a given antenna height, each antenna has the largest possible size that fits within this sphere.

composed of a top-loaded bow-tie section with a system of cascaded top hats mounted on top of a ground plane, two shorting arms, and a ring slot in the ground plane. The low end of the planar bow-tie is connected to the feed extending from the ground plane, and the top end is connected to the bottom top hat. The bottom top hat is connected to the second top hat through two shorting pins. The slanted shorting pins connect the bottom top hat to the ground plane. A rectangular-shaped ring slot is cut around the feed in the ground plane, which creates a series capacitor in the path of the electric currents flowing on the ground plane to the feed.

To understand the principles of operation of this structure, we will examine the effects of different building blocks of the antenna on its performance. We start with the bow-tie section. Let us consider a sphere with a radius of 5.8 cm. The VSWRs of three different bow-tie monopole antennas, which fit in this sphere, are presented in Fig. 2. The first resonance of the bow-tie occurs when the height is approximately a quarter of a wavelength. Fig. 2 shows that as the height increases, the lowest frequency decreases. However, increasing the height to the maximum possible value, i.e., a , results in conversion of the bow-tie to a conventional thin monopole and adversely impacts the impedance matching bandwidth of the antenna.¹ To achieve a compromise between the antenna height and the input VSWR, a bow-tie antenna with a height of 33.3 mm and width of 66.7 mm is used. Interestingly, this bow-tie fits within the largest cubical volume completely enclosed by the sphere with radius of $a = 5.8$ cm.

The main role of the other building blocks of the antenna shown in Fig. 3 is to act as a composite reactive load with proper frequency response to introduce two additional reso-

¹This can be seen in Fig. 2 by comparing the red and blue VSWR curves. The blue antenna has a lower first resonant frequency, but higher VSWR than the red antenna.

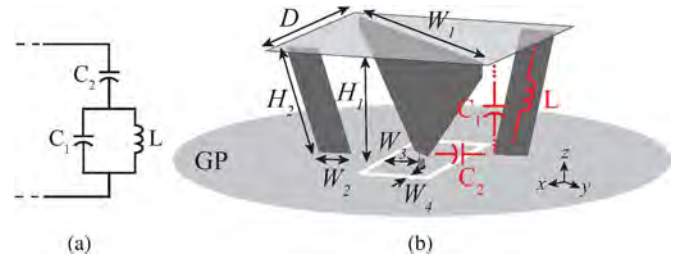


Fig. 3. (a) circuit model of the distributed reactive load that loads the bow-tie antenna. (b) Topology of the bow-tie antenna loaded with the distributed load whose equivalent circuit is shown in part (a).

TABLE II
GEOMETRICAL PARAMETERS OF THE REACTIVELY LOADED
BOW-TIE ANTENNA SHOWN IN FIG. 3(b)

Parameter	W_1	W_2	W_3	W_4	H_1	H_2	D
Value	84.8	12.0	16.3	2.3	33.3	41.9	66.7

nances below the lowest frequency of operation of the bow-tie section and considerably reduce the lowest frequency of operation of the structure. The lowest resonance in the bow-tie antenna is a series-type resonance. According to the Fosters reactance theorem, the imaginary part of the reactance for passive and lossless networks increases with frequency. Therefore, to further reduce the lowest frequency of the bow-tie antenna, a reactive load with a series resonance at a frequency of f_{low} and a parallel resonance at a frequency of f_{high} was used. The equivalent circuit model of this resonator is composed of a capacitor in series with a parallel LC circuit as shown in Fig. 3(a). This circuit has two resonances at $f_{high} = 1/2\pi\sqrt{LC_1}$ and $f_{low} = 1/2\pi\sqrt{L(C_1 + C_2)}$, which are of parallel and series types, respectively. If the frequencies of these new resonances are close enough to each other and also fall below and close to the lowest frequency of the bow-tie, the lowest frequency of operation of the antenna can be further reduced.

Fig. 3(b) shows the geometrical configuration of the modified antenna that includes the proposed reactive load. The top hat, shorting arms, and the ring slot cut into the ground plane correspond to C_1 , L , and C_2 , respectively. The top-hat dimensions, which correspond to C_1 , affect both f_{low} and f_{high} . Therefore, the dimensions of the top hat need to be maximized to achieve the maximum miniaturization. To minimize the lateral dimensions of the antenna and efficiently use the available volume, the top hat is positioned on top of the bow-tie in such a way that the diagonal of the top hat is aligned with the plane of the bow-tie. The shorting arms mounted on the ground plane and the top hat correspond to L , and their inductance values can be controlled by the length H_2 and the width W_2 of the arms. The inductor value increases by decreasing the width and/or increasing the length of the arms. Introducing two slanted arms at both sides of the bow-tie helps achieve more omnidirectional radiation patterns. Finally, the ring slot cut into the ground plane corresponds to C_2 . The value of this capacitor can be adjusted by controlling the placement of the slot and the gap size between the inner and outer parts of the ground plane. The optimized values of all the geometrical parameters of a prototype of this antenna fit in a cubical volume with the lateral dimensions of 66.7 mm and are reported in Table II.

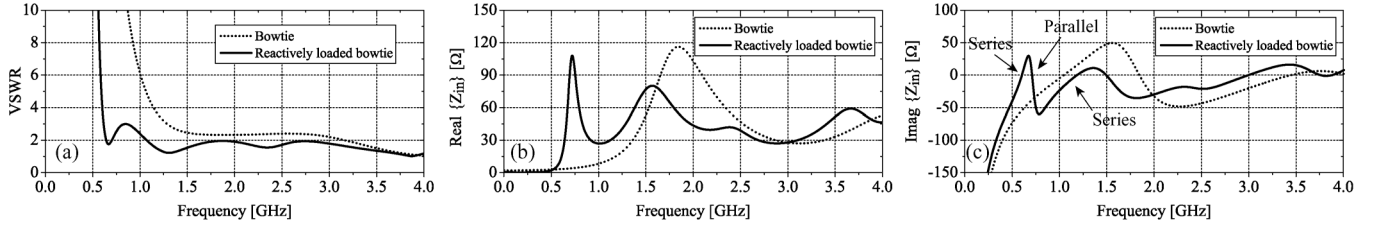


Fig. 4. Effect of the reactive load added to the bow-tie antenna on the performance of the antenna. (a) Input VSWR, (b) real part of the input impedance, and (c) imaginary part of the input impedance of the bow-tie and the reactively loaded bow-tie antennas are shown.

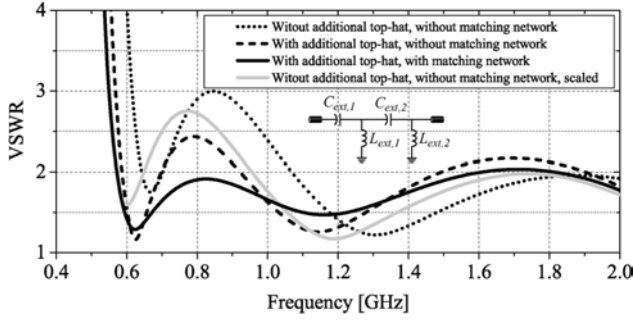


Fig. 5. Comparison between the VSWRs of the antenna with and without the additional top hat and external impedance matching network.

Fig. 4(a)–(c) shows the effect of the reactive load on the performance of the bow-tie antenna. As can be seen in Fig. 4(c), a parallel resonance and a series resonance close to the lowest resonance of the bow-tie antenna are introduced. Fig. 4(a) compares the input VSWR of the antenna with and without the reactive load. The lowest frequency where a VSWR of 3 is achieved is further reduced.

A number of different techniques can be employed to reduce the VSWR of the antenna within its operational bandwidth. A possible solution to do this is to increase C_1 , which shifts both resonances to lower frequencies. The quality factor of the series resonance also decreases, which helps improve the antenna's VSWR. As the maximum dimensions are already chosen for the top hat, an additional top hat is introduced to increase C_1 as depicted in Fig. 1. Adding an additional top hat increases the height of the antenna and eventually the enclosing sphere's radius. Therefore, to make a fair comparison, the input VSWR of the antenna with the additional top hat and the scaled version of the antenna [shown in Fig. 3(b)] without the additional top hat are compared in Fig. 5. Both of these antennas fit within a sphere with a radius of $a = 64$ mm. As can be observed, the new version of the antenna has a better VSWR. The VSWR can further be improved by using an external four-element matching network with commercially available elements of $C_{ext,1} = 9$ pF, $C_{ext,2} = 9$ pF, $L_{ext,1} = 14$ nH, and $L_{ext,2} = 36$ nH. The circuit topology of the external matching network is shown in Fig. 5. The input VSWR of the antenna with additional top hat and the external matching network is also shown in Fig. 5.

III. MEASUREMENT RESULTS AND DISCUSSION

A prototype of the antenna discussed in Section II is fabricated. A dielectric substrate covered with metal on one side

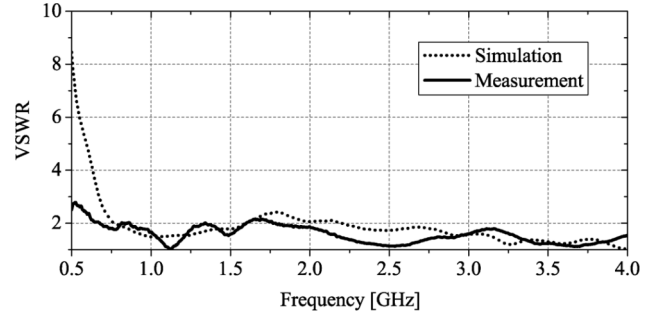


Fig. 6. Measured and simulated input VSWRs of the proposed UWB antenna.

with an etched ring slot is used as the ground plane of the antenna. The external matching network is formed by chip inductors and capacitors. One drawback of introducing the slot in the ground plane of the structure is that it makes the antenna unbalanced at low frequencies (i.e., less than 1.0 GHz) because of the small size of the central ground plane. To address this problem, a coaxial choke-balun that operates within the 0.5–1.5-GHz frequency range is used in the measurement. The balun effectively chokes the currents flowing on the outer conductor of the feeding coaxial cable. The measured and simulated input VSWRs of the prototype are shown in Fig. 6. As can be observed, the VSWR remains lower than 2.2 over a frequency band of 0.6 to at least 4 GHz.

The radiation patterns of the antenna are measured using a multiprobe spherical near-field system. Fig. 7 shows the far field co- and cross-polarized (E_θ , E_ϕ) radiation patterns of the antenna in the azimuth plane (xy -plane) in the frequency range of 0.6–3.2 GHz. Observe that the radiation patterns remain relatively omnidirectional within the azimuth plane. As frequency increases beyond 3.2 GHz, the radiation pattern of the antenna in the azimuth plane starts to become more directional. This directionality of the patterns is due to the presence of the shoring arms at two ends. The measured radiation patterns of the antenna in two elevation planes (xz - and yz -planes) are shown in Fig. 7 as well. Observe that the antenna at these two planes has radiation patterns similar to those of a vertically polarized monopole antenna on a finite ground plane.

The realized gain and total efficiency of the antenna are also measured using the same near-field system. A reference double-ridged horn antenna is used as a gain calibration standard. The measured peak realized gain alongside the simulation results and also the measured total efficiency of the antenna, which include the impedance mismatch effects, are shown in Fig. 8. As can be seen, the minimum radiation efficiency is approximately

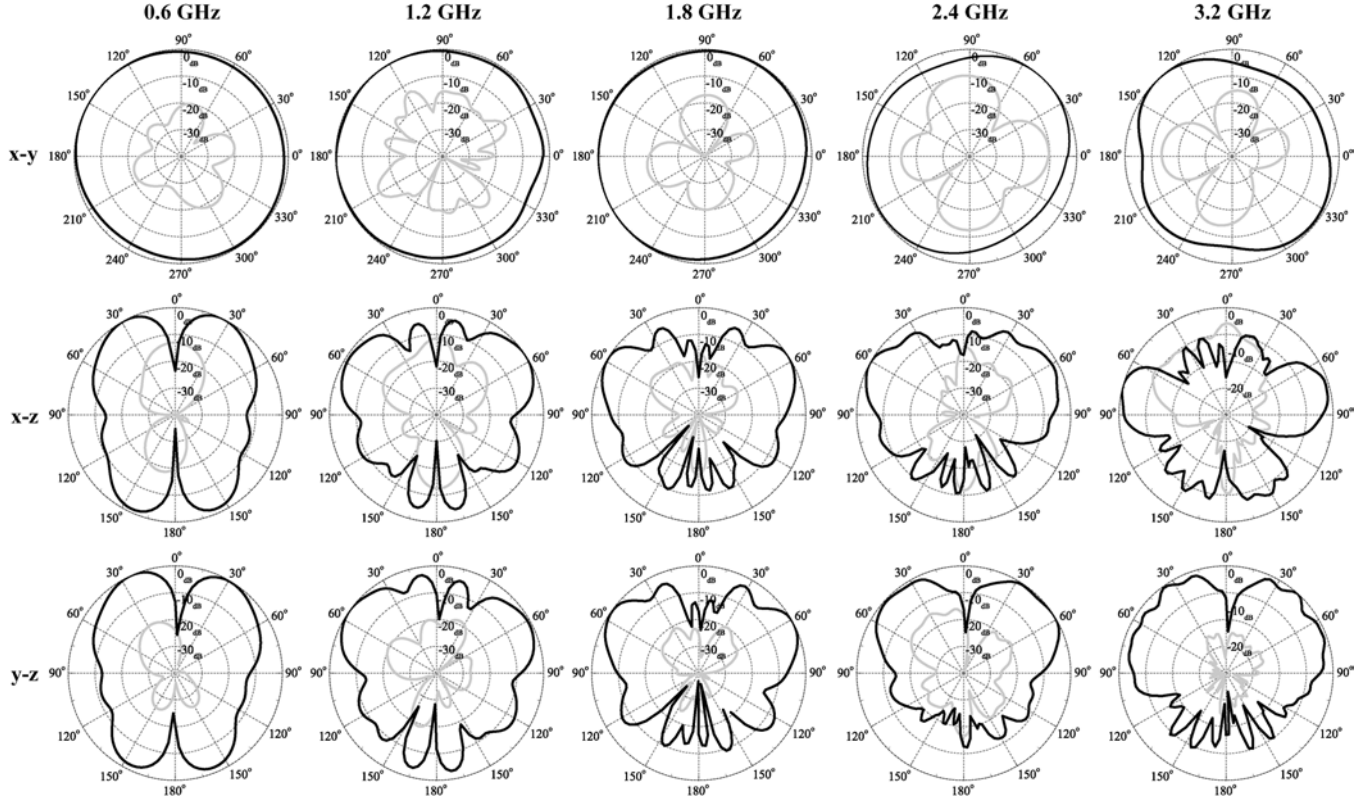


Fig. 7. Measured normalized radiation patterns of the antenna in the azimuth plane (x - y -plane) and two elevation planes (x - z - and y - z -planes).

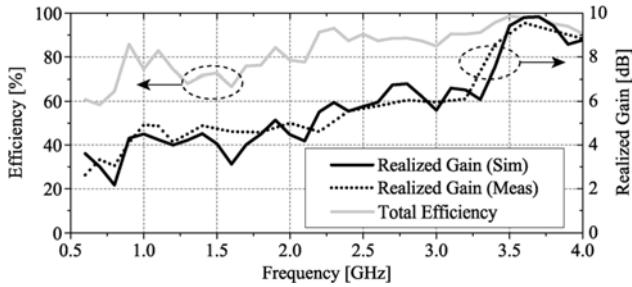


Fig. 8. Measured and simulated peak realized gain and measured total efficiency of the antenna.

60% at the lowest frequency of operation. Over most of the operating band, the total efficiency remains above 70%.

IV. CONCLUSION

A small, low-profile, ultrawideband antenna was presented in this letter. The proposed antenna takes advantage of broadband characteristics of a bow-tie section. Using a reactive load coupled to the bow-tie section and an external matching network added at the feed point, the lowest frequency of operation of the antenna is reduced while maintaining its occupied volume and a VSWR below 2.2. At the lowest frequency of operation, the antenna archives electrical dimensions of $0.085\lambda_{\min} \times 0.189\lambda_{\min} \times 0.189\lambda_{\min}$. The proposed antenna demonstrates a VSWR lower than 2.2:1 and consistent monopole-like radiation patterns over a frequency range of 5.5:1. As shown in Table I, for the same bandwidth, the proposed antenna has one of the lowest maximum dimensions among the current state-of-the-art antennas reported in the

literature. Because of the compact overall dimensions and omnidirectional vertically polarized radiation characteristics, scaled versions of this antenna are expected to be useful for low-frequency communication systems operating within the VHF and UHF frequency bands.

REFERENCES

- [1] S. Palud, F. Colombel, M. Himdi, and C. Le Meins, "Wideband omnidirectional and compact antenna for VHF/UHF band," *IEEE Antennas Wireless Propag. Lett.*, vol. 10, pp. 3–6, 2011.
- [2] T. Yang, W. A. Davis, and W. L. Stutzman, "The design of ultra wideband antennas with performance close to the fundamental limit," in *Proc. URSI Gen. Assembly*, Chicago, IL, USA, Aug. 7–16, 2008.
- [3] H. R. Stuart and S. R. Best, "A small wideband multimode antenna," in *Proc. IEEE Int. Symp. Antennas Propag.*, Jul. 5–11, 2008, pp. 1–4.
- [4] Z. Jing, D. Psychoudakis, C.-C. Chen, and J. L. Volakis, "Design optimization of a low-profile UWB body-of-revolution monopole antenna," *IEEE Trans. Antennas Propag.*, vol. 60, no. 12, pp. 5578–5586, Dec. 2012.
- [5] G. Goubau, N. N. Puri, and F. Schwing, "Diakoptic theory for multi-element antennas," *IEEE Trans. Antennas Propag.*, vol. AP-30, no. 1, pp. 15–26, Jan. 1982.
- [6] H. Nakano, H. Iwaoka, K. Morishita, and J. Yamauchi, "A wide low-profile, antenna composed of a conducting body of revolution and a shorted parasitic ring," *IEEE Trans. Antennas Propag.*, vol. 56, no. 4, pp. 1187–1192, Apr. 2008.
- [7] A. Elsherbini and K. Sarabandi, "Very low-profile top-loaded UWB coupled sectorial loops antenna," *IEEE Antennas Wireless Propag. Lett.*, vol. 10, pp. 800–803, 2011.
- [8] J. Oh and K. Sarabandi, "Ultra-wideband, miniaturized, low profile, omnidirectional antenna using a novel reactive loading approach," in *Proc. IEEE Int. Symp. Antennas Propag.*, Jul. 8–14, 2012, pp. 1–2.
- [9] N. Behdad, M. Li, and Y. Yusuf, "A very low-profile, omnidirectional, ultrawideband antenna," *IEEE Antennas Wireless Propag. Lett.*, vol. 12, pp. 280–283, 2013.
- [10] L. J. Chu, "Physical limitations of omni-directional Antennas," *J. Appl. Phys.*, vol. 19, pp. 1163–1175, Dec. 1948.

- [9] M. Bozzi, A. Georgiadis, and K. Wu, "Review of substrate-integrated waveguide circuits and antennas," *IET Microw. Antennas Propag.*, vol. 5, no. 8, pp. 909–920, Jun. 2011.
- [10] Y. J. Cheng, "Substrate integrated waveguide frequency-agile slot antenna and its multibeam application," *Prog. Electromagn. Res.*, vol. 130, pp. 153–168, Aug. 2012.
- [11] S. Sam, H. Kang, and S. Lim, "Frequency reconfigurable and miniaturized substrate integrated waveguide interdigital capacitor (SIW-IDC) antenna," *IEEE Trans. Antennas Propag.*, vol. 62, no. 3, pp. 1039–1045, Mar. 2014.
- [12] L. R. Tan, R. X. Wu, C. Y. Wang, and Y. Poo, "Magnetically tunable ferrite loaded SIW antenna," *IEEE Antennas Wireless Propag. Lett.*, vol. 12, no. 1, pp. 273–275, Feb. 2013.
- [13] L. R. Tan, R. X. Wu, C. Y. Wang, and Y. Poo, "Ferrite-loaded SIW bowtie slot antenna with broadband frequency tunability," *IEEE Antennas Wireless Propag. Lett.*, vol. 13, no. 1, pp. 325–328, Feb. 2014.
- [14] D. M. Pozar, *Microwave Engineering*, 3rd ed. Hoboken, NJ, USA: Wiley, 2004.
- [15] Q. L. Guo, Z. F. Hu, Y. P. Liang, Y. Y. Li, and L. L. Sun, "Development of low profile cavity backed crossed slot antennas for planar integration," *IEEE Trans. Antennas Propag.*, vol. 57, no. 10, pp. 2972–2979, Oct. 2009.

A Compact, Broadband Spiral Antenna With Unidirectional Circularly Polarized Radiation Patterns

Ting-Yen Shih and Nader Behdad

Abstract—A low-profile, compact spiral antenna with a broadband circularly polarized (CP) response is presented. The antenna is backed by a ground plane and has unidirectional radiation patterns over its entire frequency band of operation. This antenna is a multilayer structure composed of a center-fed modified Archimedean spiral that exploits a novel loading structure, a ring-shaped absorber, and a feed network, which includes a 180° power splitter. The loading structure possesses both inductive and capacitive characteristics, which increase the equivalent electrical length of the antenna while maintaining its maximum dimensions. The Archimedean spiral is integrated into the multilayer dielectric structure along with its differential feed network. An optimized ring-shaped absorber is used on the periphery of the antenna to reduce the ground effects on the antenna performance. The proposed antenna occupies a volume that is 89% smaller than that occupied by a conventional ground-plane-backed Archimedean spiral antenna. At its lowest frequency of operation, the antenna has electrical dimensions of $0.21\lambda_{\min} \times 0.21\lambda_{\min} \times 0.09\lambda_{\min}$, where λ_{\min} is the free-space wavelength at the lowest frequency of operation (0.5 GHz). Over the frequency range from 0.5 to 1.4 GHz (2.8:1), the antenna has a VSWR of 2.4:1, and it has a CP radiation pattern with an axial ratio better than 1.2 dB. Within this frequency range, the antenna has minimum and maximum realized gain values of -5.0 dBiC and 3.1 dBiC, respectively.

Index Terms—Broadband antennas, circular polarization, spiral antennas.

I. INTRODUCTION

Compact and broadband antennas have a wide spectrum of applications in commercial and military wireless systems. Numerous techniques for designing such antennas have been reported in the past [1]–[3]. In many applications, broadband antennas with circularly polarized (CP) radiation characteristics are needed. Examples include global navigation satellite systems, mobile satellite services, satellite communications, and certain radio-frequency identification applications [4]–[8]. A number of different techniques for designing broadband CP antennas have been examined in the past [9]–[12]. Among such antennas, spiral antennas have received a significant amount of attention over the past several decades due to their ultra-wideband (UWB) characteristics and reasonably compact and low-profile dimensions [3]. A two-arm Archimedean spiral antenna that has a constant input impedance and CP radiation patterns over a wide range of frequencies was proposed by Kaiser in 1960 [3]. In this traditional antenna, the lower and upper frequencies of operation are determined by the outer and inner radii of the spiral, respectively. The frequency response of this spiral antenna also depends on the growth factor of the spirals, as well as the line widths and the truncation effects in the finite spirals. From a practical point of view, when designing a spiral antenna, the growth factor and the line width can easily be determined by referring to the design rules

Manuscript received May 30, 2014; revised March 01, 2015; accepted March 14, 2015. Date of publication March 19, 2015; date of current version May 29, 2015. This work was supported by the Office of Naval Research under ONR Award N00014-11-1-0618.

The authors are with the Department of Electrical and Computer Engineering, University of Wisconsin-Madison, Madison, WI 53706 USA (e-mail: tshih6@wisc.edu; behdad@wisc.edu).

Color versions of one or more of the figures in this communication are available online at <http://ieeexplore.ieee.org>.

Digital Object Identifier 10.1109/TAP.2015.2414476

of the printed circuit board fabrication method used, which determine the lower bounds of the line and slot widths. Following these design rules and the guidelines for standard lithography techniques for fabricating printed circuit boards,¹ the maximum linear dimension of a bidirectional Archimedean spiral antenna (that provides CP radiation with an axial ratio better than 3 dB) can be calculated as approximately $0.38\lambda_{\min}$, where λ_{\min} is the free-space wavelength at the lowest frequency of operation of the spiral antenna [3]. Such a conventional Archimedean spiral antenna, however, has bidirectional radiation patterns. In many applications, this is not desirable since the antenna needs to be mounted on a large metallic platform. To achieve unidirectional radiation patterns, the spiral antenna can be placed over a ground plane at a distance of $\lambda_{\min}/4$ [13]. Therefore, a conventional CP, unidirectional Archimedean spiral antenna has electrical dimensions of $0.38\lambda_{\min} \times 0.38\lambda_{\min} \times 0.25\lambda_{\min}$ at its lowest frequency of operation. While such an antenna has a unidirectional radiation pattern, it also has a relatively high overall profile, which may not be desirable in many low-frequency (e.g., VHF and UHF) applications. Other techniques for achieving unidirectional radiation patterns in spiral antennas have also been examined [14]–[16]. Among all unidirectional antennas, ground-backed and cavity-backed antennas can be most easily mounted on metallic platforms. One of the challenges of designing ground-backed or cavity-backed antennas is to prevent strong mutual coupling between the antenna and the ground or the cavity. The coupling leads to axial ratio deterioration. A number of different researchers proposed using absorbers to decrease these mutual coupling effects [14], [17]. Other researchers utilized electromagnetic band-gap (EBG) structures or artificial magnetic conductors (AMC) in unidirectional spiral antennas [16]. Several ground-backed and cavity-backed antennas are compared in Table I. These antennas either demonstrate broadband responses or have compact sizes. However, having both of these criteria in a single antenna is highly desirable in many applications. To address this growing need, spiral antenna miniaturization techniques are needed.

A number of different spiral antenna miniaturization techniques have been examined in the past [26]–[33]. These techniques can be categorized into three classes: 1) inductive loading (series inductance); 2) capacitive loading (shunt capacitance); and 3) slow-wave treatments (series inductance and shunt capacitance). Inductive loading increases the inductance per unit length of the spiral arms. Some of the well-known realization methods are: using a series of lumped inductors along spiral arms [30], using two-dimensional (2-D) meandering lines [26]–[28], [33], and using three-dimensional (3-D) coils [31]. Similarly, capacitive loading increases the capacitance per unit length of the spiral arms. This can be realized by using dielectric material loading [33] and tapered dielectric loading [29]. The slow-wave treatment is a combination of inductive and capacitive loading. It increases both the series inductance and the shunt capacitance per unit length. In [31], the slow-wave treatment was realized by using 3-D coils in combination with dielectric loading.

In this communication, we present a miniaturization technique that takes advantage of several size reduction methods simultaneously, and can be applied to Archimedean spiral antennas. Using this technique, the volume occupied by a unidirectional Archimedean spiral antenna can be reduced to $0.21\lambda_{\min} \times 0.21\lambda_{\min} \times 0.09\lambda_{\min}$. This corresponds to a volume reduction factor of 89% compared to a conventional ground-plane-backed Archimedean spiral antenna. (Conservatively, such an antenna has electrical dimensions of $0.38\lambda_{\min} \times 0.38\lambda_{\min} \times 0.25\lambda_{\min}$ at its lowest frequency of

TABLE I

COMPARISON OF THE PROPOSED ANTENNA WITH A NUMBER OF DIFFERENT CAVITY-BACKED AND GROUND-BACKED ANTENNAS REPORTED IN THE LITERATURE

Ref.	H	L	W	BW	Peak Gain
[18]	0.18	0.86	0.86	15%*	8.7 dBiC
[19]	0.07	0.38	0.38	79%**	3 dBiC
[20]	0.09	0.22	0.22	13%	2.9 dBiC
[21]	0.22	1.14	0.66	22%*	9 dBiC
[22]	0.07	0.80	0.80	100%	8.5 dBiC
[23]	0.27	1.52	1.52	50%	11.0 dBiC
[24]	0.30	0.85	0.85	4%*	7.1 dBiC***
[25]	0.25	1.03	1.03	55%	9.9 dBiC
This Work	0.09	0.21	0.21	95%	3.4 dBiC

Bandwidth is determined based on the frequency range, where the axial ratio is less than 3 dB and the realized gain is higher than -5 dBiC.

*Only the 3 dB axial ratio was reported and used to determine the bandwidth.

**Only the realized gain was reported and is used to determine the bandwidth.

***7.1 dBiC (LHCP), 4.9 dBiC (RHCP).

****The unit of H, L, and W is λ_{\min} .

operation.) The proposed miniaturization technique is based on loading the spiral arms at their ends with a slow-wave structure possessing both capacitive and inductive elements. This increases the effective electrical lengths of the arms, thereby reducing the lowest frequency of operation of the antenna while maintaining its maximum linear dimensions. A ground plane is placed underneath the antenna to achieve unidirectional radiation. To further miniaturize the antenna and to decrease the spacing between the ground plane and the main radiator, the antenna and the ground plane are separated with dielectric substrate with a relatively high dielectric constant ϵ_r . Since doing this results in confinements of the antenna fields in the region below the plane of spiral, the antenna is also loaded with a thick, high- ϵ_r superstrate to enhance its radiation efficiency. To mitigate the adverse effects of the ground plane's presence on the axial ratio of the antenna, a ring-shaped absorber is placed on the periphery of the antenna. The antenna is fed with differential semirigid coaxial cables. A prototype of the proposed antenna operating in the frequency range of 0.5–1.4 GHz is designed, fabricated, and measured. The fabricated prototype shows a minimum realized gain of -5.0 dBiC, a maximum realized gain of 3.1 dBiC, a VSWR better than 2.4:1, and an axial ratio of 1.2 dB over this broad frequency band. In what follows, the details of the design and the principles of operation of the antenna are presented and discussed.

II. ANTENNA DESIGN

A. Antenna Structure

Fig. 1 shows the cross-sectional and the top views of the proposed antenna. Unlike a conventional Archimedean spiral antenna, the two arms of the proposed antenna are located on two different sides of a dielectric substrate ("sub 2" in Fig. 1). The inner and outer radii of the spiral antenna with loading structure are 1 and 60.6 mm, respectively. The spiral arm width and the gap between two adjacent arms are 1 mm. There are 13 turns of spiral arms and 1.5 turns of loading structure as shown in Fig. 1. Two dielectric substrates with the thickness of 25.4 mm and dielectric constants of $\epsilon_r = 10.2$ sandwich the spiral antenna ("sub 1" and "superstrate" in Fig. 1). Sub 1 and the superstrate are both composed of ten stacked layers of RT/duroid-6010.2LM substrates (from Rogers Corp.), each with a thickness of 2.54 mm. A

¹The following are typical design rules in fabricating printed circuit boards: The minimum line width is 0.005", the minimum trace to trace spacing is 0.005", and the minimum diameter of drilled non-plated holes is 0.010".

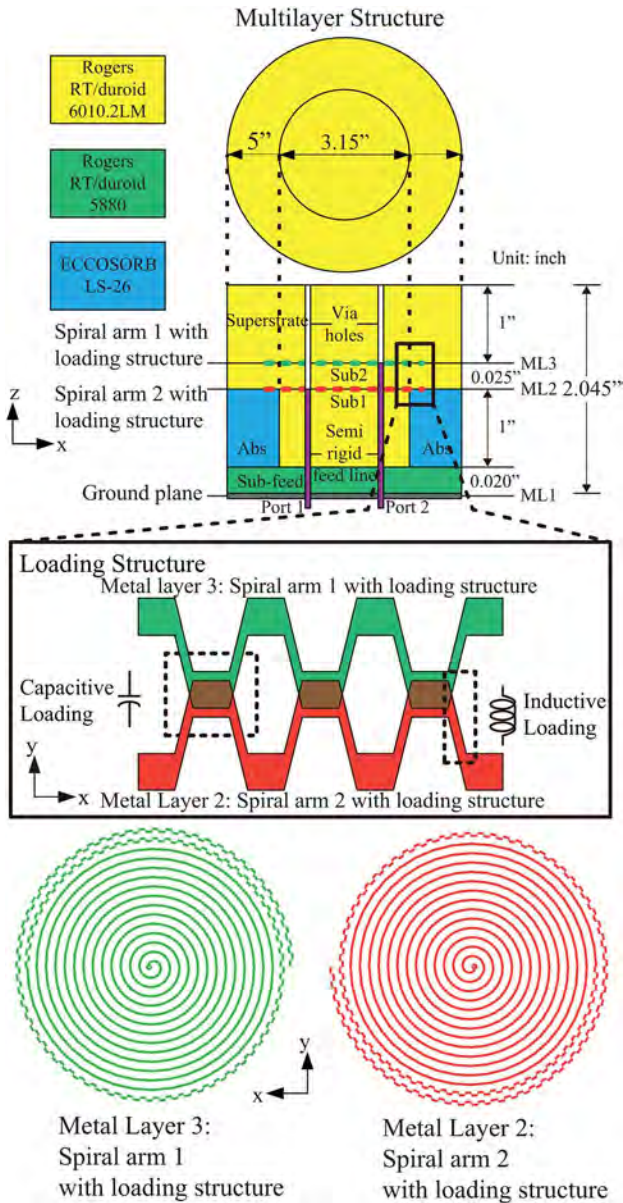


Fig. 1. Topology of the proposed ground plane backed UWB spiral antenna.

ground plane is placed behind the antenna (on metal layer 1), on the bottom side of a thin dielectric substrate, to make the radiation patterns unidirectional. The feed network is composed of two semirigid cables as shown in Fig. 1. The dielectric substrate immediately on top of the ground plane has a thickness of 0.508 mm and a dielectric constant of 2.2 (RT/duroid 5880 from Rogers Corp.). The feed network is composed of two 50 Ω semirigid coaxial cables as shown in Fig. 1. The semirigid cables are connected to SMA connectors and are used to feed the antennas. One of the semirigid cables extends all the way through the thickness of substrate 1 and its center conductor is connected to the feed point of spiral arm 2 (located on metal layer 2 as shown in Fig. 1). The other semirigid cable extends all the way through the thicknesses of substrates 1 and 2, and its center conductor is connected to the feed point of the spiral arm 1 (located on metal layer 3 as shown in Fig. 1). The distance between the centers of the two semirigid cables is 2.2 mm and the diameter of each semirigid cable is 2.2 mm. The outer conductors of the semirigid cables are connected within the region ranging from the ground plane (metal layer 1), the

“sub-feed,” and all the way to 1 mm below metal layer 2. The outer conductors of the semirigid cables are also connected to the ground plane (metal layer 1). The holes accommodating the two semirigid cables are extended all the way through the thickness of superstrate as well, even though the semirigid cables terminate on the two sides of substrate 2. This is done for two reasons. First, it provides a means for aligning different stacked dielectric substrates that constitute the superstrate. Second, the holes provide additional space for the center conductor of the semirigid cables to extend beyond the plane of the spirals. This extended length of the center conductors provides a reactive impedance in parallel with the feed point impedance of the spiral and can be used for impedance tuning purposes. A ring-shaped absorber is placed on the periphery of the antenna between metal layer 2 and the “sub-feed.” The inner and outer diameters of the ring-shaped absorber are 80 and 127 mm, respectively. The height of the absorber is 25.4 mm, which is the same as substrate 1. The circular absorber is made of ECCOSORB LS-26 (from Emerson and Cuming Microwave Products, Inc.) as shown in Fig. 1. The overall height of the multilayer structure is 52 mm and its diameter is 127 mm.

B. Innovation

The design process of the antenna started with an Archimedean spiral structure, where unlike conventional spirals, each arm of the spiral is placed on one side of a relatively thin dielectric substrate. To help decrease the physical separation between the ground plane and the spiral, a dielectric substrate with a dielectric constant of $\epsilon_r = 10.2$ was used below the antenna. This also helps with reducing the electrical dimensions of the antenna. To improve the radiation efficiency of the antenna and ensure that the fields are not confined between the antenna and the ground plane, a thick superstrate with the dielectric constant of $\epsilon_r = 10.2$ is used to load the antenna as well. To further miniaturize the antenna, a new type of a slow-wave loading structure was designed that possesses both inductive and capacitive characteristics, (see Fig. 1) and takes advantage of the fact that each arm of the spiral is printed on a different side of the dielectric substrate. This loading structure is in the form of two meandered lines with variable (modulated) widths that overlap each other on the periphery of the spiral. Each meandered line is connected to the end of an arm of the spiral. The narrow and wide sections of the meandered lines act, respectively, as distributed inductive and capacitive loads of a slow-wave structure. Unlike a conventional Archimedean spiral antenna, the two arms of this spiral are fabricated on the two different sides of the dielectric substrate. This helps further increase the capacitive loading effects of the meandered section as it allows for the meandered sections of each arm of the spiral to overlap with those of the other arm in the capacitive regions (see Fig. 1). This overlapping further increases the capacitance per unit length of the capacitive sections of the meandered spiral arm, resulting in further increasing of the electrical length of the structure for a given physical size. This slow-wave structure increases the electrical length of the spiral for a given physical length. To compare the performance of this slow-wave structure with other common structures, we conducted full-wave EM simulations of a conventional two-wire transmission line, zig-zag lines of the type reported in [26], and our proposed structure. Considering the two-wire line as the baseline, the zig-zag line provides a 13% reduction in the phase velocity, whereas our proposed structure provides a 54% reduction. The broadside-coupled meandered loading structure can be specified mathematically using

$$L = \alpha \times \text{square}(\beta \times \theta) \quad (1)$$

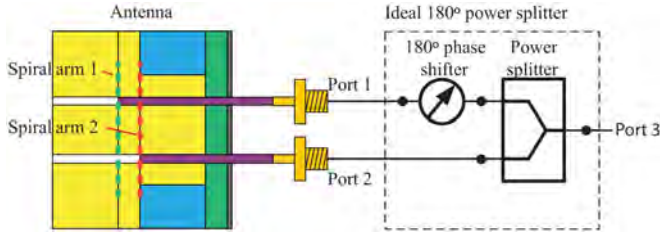


Fig. 2. The proposed UWB spiral antenna is fed with an ideal 180° power splitter, which provides differential feeding at the two ports.

where square is a function for square wave generation in MATLAB, α is 0.6, β is 128, and θ is measured from the z-axis. The size of arms 1 and 2 of the spiral antenna is determined by (2) and (3), respectively,

$$r_1 = r_0 + b \times \theta^{(1/n)} + L \quad (2)$$

$$r_2 = r_0 + b \times \theta^{(1/n)} - L \quad (3)$$

where r_0 is 39.37 mils (1 mm), b is $78.74/\pi$ mils ($2/\pi$ mm), n is 1, and θ is measured from the z-axis.

To achieve a unidirectional radiation pattern, the antenna is backed by a ground plane. In a ground-plane backed spiral antenna, the strong coupling between the antenna and the ground plane is a common problem, which can severely degrade the radiation characteristics of antenna, especially its axial ratio. In the past two decades, a variety of research groups studying cavity-backed antennas have tried to reduce the ground effects [17]–[25]. One common method used for alleviating the ground effects is to use absorbers [17]. Using absorbers decreases the mutual coupling between the ground plane and the antenna. In general, this improves the axial ratio of the antenna but it will naturally result in some gain reduction. To balance the tradeoff between these two radiation characteristics, the absorber was designed as ring-shaped, and is placed only on the periphery of the spiral arms. The inner diameter of the ring-shaped absorber is 80 mm and its width is 23.5 mm. These dimensions are determined using trial and error simulations in CST Microwave Studio. In these simulations, an attempt was made to balance the tradeoff between the axial ratio improvement and the realized gain degradation of the antenna. To achieve the desired mode of operation, the two arms of the antenna must be fed with the same magnitude and a 180° phase difference between them. This is accomplished using the feed network shown in Fig. 2. In this case, the two ports of the antenna are excited using a power divider/phase shift network. At VHF/UHF frequencies, commercially available 180° power splitters can be used to easily feed the antenna in the desired mode of operation.

III. SIMULATION AND MEASUREMENT RESULTS

The spiral antenna discussed in Section II was simulated in CST Microwave Studio. The main physical and geometrical parameters of the antenna are presented in Section II. The antenna is simulated as a two-port device, where each port is placed at the input port of one of the semirigid cables shown in Fig. 2. After each simulation, the results of the two-port full-wave EM simulations are combined to obtain the simulation results of the antenna when it is fed with a broad band 180° power splitter.

Using full-wave EM simulations in CST Microwave Studio, the electric current distribution on the spiral arms was first examined. These results confirmed that the electric currents flowing in the overlapping sections of the meandered arms are out of phase and flow in opposite directions. Therefore, the overlapped sections of the meandered spiral arms act similar to a two-wire transmission line with

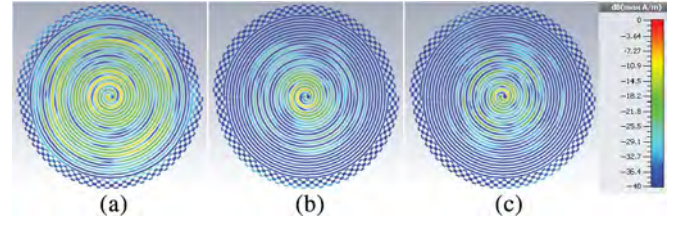


Fig. 3. Simulated surface current distributions of the antenna at: (a) 0.6 GHz; (b) 1.0 GHz; and (c) 1.4 GHz.

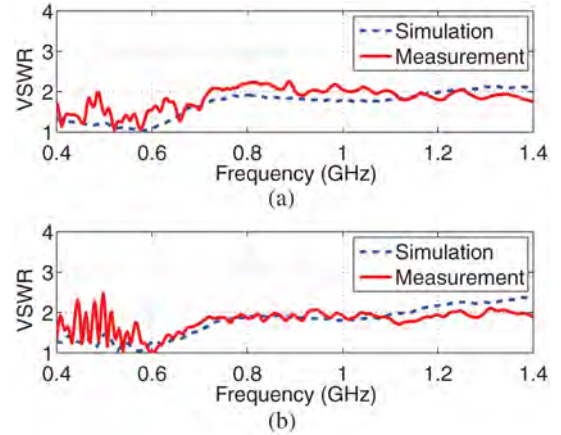


Fig. 4. Simulated and measured VSWR of the antenna (a) at port 1 when port 2 is terminated with $50\ \Omega$ load and (b) at port 2 when port 1 is terminated with $50\ \Omega$ load.

enhanced capacitance per unit length. Additionally, the narrow sections of the meanders have increased inductance per unit lengths. Therefore, the meandered sections of the spiral arms act as slow-wave structures with increased capacitance and inductance per unit length. The current distribution on the antenna arms is simulated and the results are shown for 0.6, 1, and 1.4 GHz in Fig. 3. As can be observed, at each frequency, the current magnitude on the spiral arms decays as one moves from the center toward the edges of the spiral. This is an indication that standing waves on spiral arms are not significant and consequently, a low axial ratio is expected. After completion of the design process and fine tuning of the physical and geometrical parameters of the antenna, a prototype of the proposed antenna was fabricated. The spiral antenna was fabricated using chemical etching. We prepared 20 panels of 0.1" thick RT/duroid 6010.2LM substrates. Ten of which were cut into the diameter of 127 mm (superstrate), and the rest into the diameter of 80 mm (sub2). We also prepared four panels of 6.35-mm thick ECCOSORB LS-26 absorbers. The absorbers were cut into ring shape with outer and inner diameters of 127 mm and 80 mm, respectively. Four additional pads were left on each layer for tightening with nylon screws and nuts.

The input reflection coefficient of the fabricated prototype was characterized using a vector network analyzer. Fig. 4(a) and 4(b) shows the simulated and measured input VSWRs of the antenna as seen from the inputs of ports 1 and 2, respectively. As can be observed, a relatively good agreement between the measurement and simulation results is achieved. The measured two-port S-parameters of the antenna were also postprocessed to calculate the input VSWR of the antenna as seen from the input of the broadband 180° power splitter shown in Fig. 2 and the results are presented in Fig. 5. As can be observed, the antenna shows a VSWR of 2.4:1 over its entire frequency band of operation.

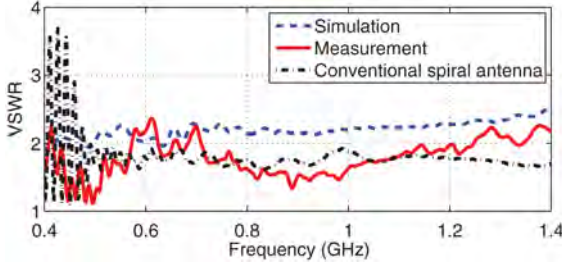


Fig. 5. Simulated and measured VSWR of the antenna as seen from the input port of the feed network shown in Fig. 2.

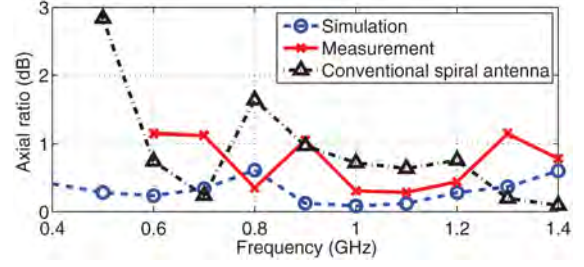


Fig. 7. Simulated and measured axial ratios of the antenna when the antenna is fed with the feed network shown in Fig. 2.

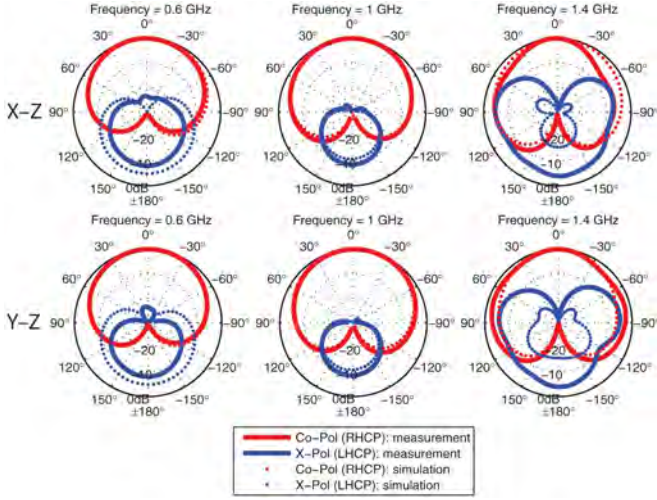


Fig. 6. Simulated and measured radiation patterns of the antenna in the $x-z$ and $y-z$ planes.

The radiation characteristics of the antenna were measured in a multiprobe, spherical near field system over the frequency range of 0.6–1.4 GHz. The measurements are conducted in two steps. First, the radiation characteristics of the antenna were measured when it was fed at port 1 while the second port was terminated with a matched load. Using the near-field system, the complex (magnitude and phase) far-field radiation parameters of the antenna were determined. Subsequently, a similar procedure was followed and the complex far-field radiated fields of the antenna were measured when the antenna was fed at port 2 while port 1 was terminated. These measured results were then postprocessed to obtain the radiation patterns of the antenna and its other radiation characteristics when the antenna is differentially fed using the feed network shown in Fig. 2. Since the spherical near-field measurement system used in these experiments provides us with all the complex far-field components, the process of combining the measurement results of the two ports is straightforward. The measured electric fields from each port were summed up with 180° phase difference in MATLAB. The axial ratio (the ratio of the major axis to the minor axis) was calculated by the combined electric fields in MATLAB. Fig. 6 shows the measured radiation patterns of the antenna over the frequency range of 0.6–1.4 GHz along with the simulated results. Measured and simulated results are shown for both the co-pol (RHCP) and cross-pol (LHCP) components of the radiated fields in two different cut planes ($x-z$ and $y-z$ planes). The cross-pol components are approximately 24 dB below the co-pol components in the direction of maximum radiation indicating a relatively good polarization purity. Moreover, the antenna's radiation patterns remain consistent across its entire frequency band of operation. In

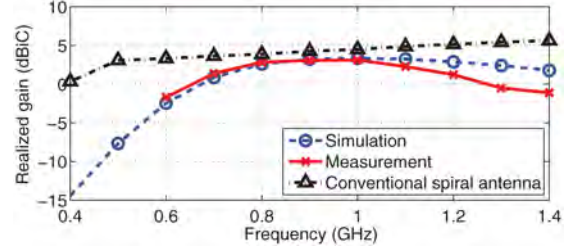


Fig. 8. Simulated and measured realized gains of the antenna when it is fed with the feed network shown in Fig. 2.

a real-life scenario, the proposed antenna should be fed with a single feed network that provides the necessary excitation amplitude and phase over a wide frequency range. In reality, such feed networks may have amplitude and/or phase imbalances at some frequencies over the band of operation. This will result in the deterioration of the axial ratio of the antenna and its polarization purity compared to what is reported in this communication.

Fig. 7 shows the measured and simulated axial ratios of the antenna along the direction of maximum radiation. As can be observed, the antenna demonstrates an axial ratio of lower than 1.2 dB across its entire band of operation. The simulated and measured realized gains of the antenna are shown in Fig. 8. The simulated and measured maximum realized gains of the antenna are 3.3 and 3.1 dBiC, respectively. Assuming that the minimum acceptable realized gain is -5.0 dBiC, the maximum acceptable axial ratio is 3.0 dB, and the maximum acceptable VSWR is 2.5:1, the bandwidth of the antenna is determined to be from 0.5 to 1.4 GHz (a 2.8:1 bandwidth). At the lowest frequency of operation of 0.5 GHz, the antenna has maximum electrical dimensions of $0.21\lambda_{\min} \times 0.21\lambda_{\min} \times 0.09\lambda_{\min}$. A conventional spiral antenna with a performance similar to the proposed antenna is also designed as a reference. It has electrical dimensions of $0.38\lambda_{\min} \times 0.38\lambda_{\min}$ (diameter = 228 mm). To make this antenna unidirectional, a ground plane is placed a quarter wavelength below the antenna [13]. The simulation results of this antenna are shown in Figs. 5, 7, and 8. The electrical volume occupied by this antenna is thus, $0.38\lambda_{\min} \times 0.38\lambda_{\min} \times 0.25\lambda_{\min}$. Notice that placing a ground plane below an Archimedean spiral antenna deteriorates its performance (i.e. axial ratio and gain) and generally shifts the lowest operation frequency of the antenna up. However, to be conservative in our comparison, we have considered the electrical volume of $0.38\lambda_{\min} \times 0.38\lambda_{\min} \times 0.25\lambda_{\min}$ as the reference for calculating the volume reduction factor of our proposed antenna 89%.

IV. CONCLUSION

In this communication, a low-profile ground-backed spiral antenna with a wideband CP response was presented. The proposed spiral

antenna achieves compact and miniaturized dimensions by employing a novel loading structure, where each arm of the antenna is both inductively and capacitively loaded. Additional miniaturization is achieved by using high dielectric constant superstrate and substrate materials. Using these techniques, the antenna diameter is effectively reduced to $0.21\lambda_{\min}$. In order to reduce the effects of the ground plane placed in close proximity of the antenna, an optimized ring-shaped absorber is placed between the antenna and the ground plane. The bandwidth of this antenna is from 0.5 to 1.4 GHz, over which the antenna shows an axial ratio of 1.2 dB, a VSWR of 2.4:1, and minimum and peak realized gain values of -5 and 3.1 dBiC, respectively. One of the advantages of the proposed multilayer structure presented in this communication is the potential integration of miniaturized-element frequency selective surfaces of the types reported in [34]–[35], within the superstrate layers of the antenna. This possibility is currently being explored for developing modified versions of the proposed antenna that demonstrate significantly reduced out of band radar cross sections and can be used for low-observable applications.

REFERENCES

- [1] N. Behdad and K. Sarabandi, "A compact dual-/multi-band wireless LAN antenna," in *Proc. IEEE Antennas Propag. Soc. Int. Symp.*, 2005, vol. 2B, pp. 527–530.
- [2] N. Behdad and K. Sarabandi, "Wideband double-element ring slot antenna," *Electron. Lett.*, vol. 40, no. 7, pp. 408–409, 2004.
- [3] J. Kaiser, "The Archimedean two-wire spiral antenna," *IRE Trans. Antennas Propag.*, vol. 8, no. 3, pp. 312–323, May 1960.
- [4] Z. Wang, S. Fang, S. Fu, and S. Jia, "Single-fed broadband circularly polarized stacked patch antenna with horizontally meandered strip for universal UHF RFID applications," *IEEE Trans. Microw. Theory Techn.*, vol. 59, no. 4, pp. 1066–1073, Apr. 2011.
- [5] J. Pourahmadazar and V. Rafii, "Broadband circularly polarized slot antenna array for L- and S-band applications," *Electron. Lett.*, vol. 48, no. 10, pp. 542–543, May 2012.
- [6] X. Chen and Wiley InterScience (Online service), *Antennas for Global Navigation Satellite Systems*. Hoboken, NJ, USA: Wiley, 2012 [Online]. Available: <http://dx.doi.org/10.1002/9781119969518>
- [7] J. Wang, "Antennas for global navigation satellite system (GNSS)," *Proc. IEEE*, vol. 100, no. 7, pp. 2349–2355, Jul. 2012.
- [8] Y. Yao, X. Wang, X. Chen, J. Yu, and S. Liu, "Novel diversity/MIMO PIFA antenna with broadband circular polarization for multimode satellite navigation," *IEEE Antennas Wireless Propag. Lett.*, vol. 11, pp. 65–68, Mar. 2012.
- [9] S. Gao, Y. Qin, and A. Sambell, "Low-cost broadband circularly polarized printed antennas and array," *IEEE Antennas Propag. Mag.*, vol. 49, no. 4, pp. 57–64, Aug. 2007.
- [10] Y.-X. Guo, L. Bian, and X. Q. Shi, "Broadband circularly polarized annular-ring microstrip antenna," *IEEE Trans. Antennas Propag.*, vol. 57, no. 8, pp. 2474–2477, Aug. 2009.
- [11] J.-H. Lu and S.-F. Wang, "Planar broadband circularly polarized antenna with square slot for UHF RFID reader," *IEEE Trans. Antennas Propag.*, vol. 61, no. 1, pp. 45–53, Jan. 2013.
- [12] X. Quan, R. Li, and M. Tentzeris, "A broadband omnidirectional circularly polarized antenna," *IEEE Trans. Antennas Propag.*, vol. 61, no. 5, pp. 2363–2370, May 2013.
- [13] J. Bell and M. Iskander, "A low-profile archimedean spiral antenna using an EBG ground plane," *IEEE Antennas Wireless Propag. Lett.*, vol. 3, no. 1, pp. 223–226, Dec. 2004.
- [14] T. Iwasaki, A. P. Freundorfer, and K. Iizuka, "A unidirectional semi-circle spiral antenna for subsurface radars," *IEEE Trans. Electromagn. Compat.*, vol. 36, no. 1, pp. 1–6, Feb. 1994.
- [15] J. Volakis, M. Nurnberger, and D. Filipovic, "A broadband cavity-backed slot spiral antenna," *IEEE Antennas Propag. Mag.*, vol. 43, no. 6, pp. 15–26, Dec. 2001.
- [16] W. Cao, A. Liu, B. Zhang, T. Yu, and Z. Qian, "Dual-band spiral patch-slot antenna with omnidirectional CP and unidirectional CP properties," *IEEE Trans. Antennas Propag.*, vol. 61, no. 4, pp. 2286–2289, Apr. 2013.
- [17] H. Nakano, S. Sasaki, H. Oyanagi, and J. Yamauchi, "Cavity-backed archimedean spiral antenna with strip absorber," *IET Microw. Antennas Propag.*, vol. 2, no. 7, pp. 725–730, Oct. 2008.
- [18] Q. Li and Z. Shen, "An inverted microstrip-fed cavity-backed slot antenna for circular polarization," *IEEE Antennas Wireless Propag. Lett.*, vol. 1, no. 1, pp. 190–192, Feb. 2005.
- [19] A. Bhoobe and D. Filipovic, "Cavity backed four-arm slot like spiral antenna for dual mode operation," in *Proc. IEEE Antennas Propag. Soc. Int. Symp.*, 2003, vol. 2, pp. 165–168.
- [20] D. Psychoudakis, J. Volakis, Z. Wing, and J. W. Halloran, "Cavity-backed miniature wideband UHF circular polarized antenna with textured dielectrics," *IEEE Trans. Antennas Propag.*, vol. 54, no. 12, pp. 3586–3592, Dec. 2006.
- [21] R. Li *et al.*, "Development of a cavity-backed broadband circularly polarized slot/strip loop antenna with a simple feeding structure," *IEEE Trans. Antennas Propag.*, vol. 56, no. 2, pp. 312–318, Feb. 2008.
- [22] H. Nakano, T. Igarashi, H. Oyanagi, Y. Iitsuka, and J. Yamauchi, "Unbalanced-mode spiral antenna backed by an extremely shallow cavity," *IEEE Trans. Antennas Propag.*, vol. 57, no. 6, pp. 1625–1633, Jun. 2009.
- [23] K.-F. Hung and Y.-C. Lin, "Novel broadband circularly polarized cavity-backed aperture antenna with traveling wave excitation," *IEEE Trans. Antennas Propag.*, vol. 58, no. 1, pp. 35–42, Jan. 2010.
- [24] Q. C. Zhang and W. Wu, "Compact dual-band circularly-polarized cavity-backed slot antenna," *Electron. Lett.*, vol. 47, no. 17, pp. 947–948, 2011.
- [25] Y.-J. Hu, W.-P. Ding, W.-M. Ni, and W.-Q. Cao, "Broadband circularly polarized cavity-backed slot antenna array with four linearly polarized disks located in a single circular slot," *IEEE Antennas Wireless Propag. Lett.*, vol. 11, pp. 496–499, May 2012.
- [26] H. Nakano and J. Yamauchi, "Characteristics of modified spiral and helical antennas," *IEE Proc. H*, vol. 129, no. 5, pp. 232–237, Oct. 1982.
- [27] E. T. Roland and W. F. Patterson, "A slow-wave flat spiral antenna," in *Proc. 17th USAF Antenna Symp. (Univ. Illinois, Allerton)*, Nov. 1967, vol. 111.
- [28] D. Filipovic and J. Volakis, "Broadband meanderline slot spiral antenna," *IEE Proc. Microw. Antennas Propag.*, vol. 149, no. 2, pp. 98–105, Apr. 2002.
- [29] B. Kramer, M. Lee, C.-C. Chen, and J. Volakis, "Miniature UWB antenna with embedded inductive loading," in *Proc. IEEE Int. Workshop Antenna Technol. Small Antennas Novel Metamater.*, Mar. 2006, pp. 289–292.
- [30] M. Lee, B. Kramer, C.-C. Chen, and J. Volakis, "Distributed lumped loads and lossy transmission line model for wideband spiral antenna miniaturization and characterization," *IEEE Trans. Antennas Propag.*, vol. 55, no. 10, pp. 2671–2678, Oct. 2007.
- [31] B. Kramer, C. Chen, and J. Volakis, "Size reduction of a low-profile spiral antenna using inductive and dielectric loading," *IEEE Antennas Wireless Propag. Lett.*, vol. 7, pp. 22–25, Feb. 2008.
- [32] B. Kramer, C.-C. Chen, M. Lee, and J. Volakis, "Fundamental limits and design guidelines for miniaturizing ultra-wideband antennas," *IEEE Antennas Propag. Mag.*, vol. 51, no. 4, pp. 57–69, Aug. 2009.
- [33] J. L. Volakis, C.-C. Chen, and K. Fujimoto, *Small Antennas: Miniaturization Techniques & Applications*. New York, NY, USA: McGraw-Hill, 2010.
- [34] N. Behdad and M. Al-Joumayly, "A generalized synthesis procedure for low-profile, frequency selective surfaces with odd-order bandpass responses," *IEEE Trans. Antennas Propag.*, vol. 58, no. 7, pp. 2460–2464, Jul. 2010.
- [35] N. Behdad, "A second-order band-pass frequency selective surface using nonresonant subwavelength periodic structures," *Microw. Opt. Technol. Lett.*, vol. 50, no. 6, pp. 1639–1643, 2008.

Harmonic-Suppressed Miniaturized-Element Frequency Selective Surfaces With Higher Order Bandpass Responses

Seyed Mohamad Amin Momeni Hasan Abadi, *Student Member, IEEE*, Meng Li, *Member, IEEE*, and Nader Behdad, *Senior Member, IEEE*

Abstract—We introduce a new technique for designing miniaturized-element frequency selective surfaces (MEFSSs) with bandpass responses and no spurious transmission windows over extremely large bandwidths. The proposed harmonic-suppressed MEFSSs consist of multiple metallic and dielectric layers. Each metallic layer is in the form of a two-dimensional arrangement of capacitive patches or an inductive wire grid with extremely sub-wavelength periods. Harmonic-free operation in these structures is achieved by using multiple, closely spaced capacitive layers with overlapping unit cells to synthesize a single, effective capacitive layer with a larger capacitance value. This allows for reducing the unit cell size of a conventional MEFSS considerably and moving the natural resonant frequencies of its constituting elements to considerably higher frequencies. Consequently, the spurious transmission windows of such MEFSSs, which are caused by these higher order harmonics, can be shifted to very high frequencies and an extremely broad frequency band free of any spurious transmission windows can be obtained. Using this technique, an MEFSS with a second-order bandpass response is designed to operate at 3.0 GHz with 20% fractional bandwidth and be free of spurious transmission bands up to 27.0 GHz. A prototype of this harmonic-free MEFSS is fabricated and experimentally characterized in the lab. Measurement results confirm harmonic-free operation of the proposed FSS for incidence angles in the $\pm 60^\circ$ range for both the TE and TM polarizations of incidence.

Index Terms—Frequency selective surfaces, periodic structures, radomes.

I. INTRODUCTION

FREQUENCY selective surfaces (FSSs) have been the subject of numerous studies so far. At microwave and millimeter-wave frequencies, FSSs are used in a wide range of ap-

plications including spatial filters [1], [2], radar absorbing materials [3], [4], artificial magnetic conductors [5], [6], planar lenses [7], [8] and reflectarrays [9]. One common application of FSSs is to use them to reduce the radar cross section (RCS) of antennas used in low-observable or stealth platforms. Most antennas act as efficient scatterers both at the frequency band(s) that they are designed to operate in and at other frequency bands that fall outside of their desired frequency range of operation. A typical low-observable platform may have several low-frequency antennas operating at VHF and UHF bands. These antennas act as very efficient scatterers at higher frequencies where many radars operate at. In such applications, the RCS of the antenna can be reduced by shielding it from the outside environment using a shaped bandpass FSS that is transparent within the desired frequency of operation of the antenna and opaque at other frequencies. While the aforementioned RCS reduction approach works in principle, it suffers from a practical design problem. Namely, most FSSs reported in the literature have multiple spurious transmission windows occurring at frequencies higher than that of the main one (e.g., see [1, pp. 26–62]). Although the high frequency harmonics typically will not impact the in-band performance of these FSSs, they could become critically important in certain stealth applications in which they coincide with a frequency at which the antenna presents a high RCS value. For an FSS designed to work at a low frequency (e.g., UHF), a number of these spurious transmission windows can fall within the 1–20 GHz range where many radars operate. Thus, in such applications, suppression of the spurious harmonics of the FSS is highly desired.

A number of previous studies has been conducted in this area [10]–[12]. In [10], an absorptive/transmissive radome is presented. The presented multilayer structure is formed by placing an artificial absorbing coating on a frequency selective surface. This structure, however, achieves absorption properties by using a uniform resistive layer of conductive fiber, which deteriorates the in-band performance of the radome as well. In [11], a bandpass FSS with quasi-elliptic response and wide-stopband characteristics is reported. The structure is formed by cascading periodic arrays of double square loops and gridded square loops. However, this approach requires using several metallic layers separated from one another by rather thick dielectric substrates to design a low-frequency (e.g., UHF) FSS. This leads to a relatively large overall thickness for the FSS (compared to the wavelength) that makes the response of the structure sensitive

Manuscript received November 17, 2013; revised January 18, 2014; accepted January 25, 2014. Date of publication January 30, 2014; date of current version May 01, 2014. This work was supported by Level 3 Communications – Randtron Antenna Systems and by the Office of Naval Research under ONR Award No. N00014-11-1-0618.

S. M. A. Momeni Hasan Abadi and N. Behdad are with the Department of Electrical and Computer Engineering, University of Wisconsin-Madison, Madison, WI 53706-1691 USA (e-mail: momenihassana@wisc.edu; behdad@wisc.edu).

M. Li was with the Department of Electrical and Computer Engineering, University of Wisconsin in Madison, Madison, WI 53706-1691 USA. He is now with Qualcomm, San Diego, CA 92121 USA.

Color versions of one or more of the figures in this paper are available online at <http://ieeexplore.ieee.org>.

Digital Object Identifier 10.1109/TAP.2014.2303822

to the angle and polarization of incidence of the EM wave. In [12], a bandpass FSS with wideband absorbing properties is presented. The reported structure behaves as a bandpass filter in the main band of operation, while behaving as an absorber above the main band. This is realized by cascading a bandpass FSS and a resistive high-impedance surface which uses the FSS as the ground plane within its total reflection band. Although a relatively good performance was observed under normal incidence of the EM wave, the performance of this structure degrades when the structure is illuminated with an obliquely incident wave. The problem can be attributed to the absorption properties of the resistive surface which degrade as a function of the incident angle. As a result, some harmonics appear within the absorption band. This is not desirable in low-observable FSS and radome applications.

Over the past few years, several new classes of frequency selective surfaces with sub-wavelength unit cells dimensions are reported [14]–[25]. These structures are referred to as miniaturized element frequency selective surfaces (MEFSSs).¹ Depending on the specific design process, MEFSSs are composed of entirely nonresonant constituting elements (e.g., [14]–[19], [22]) or a combination of resonant and nonresonant elements (e.g., [20], [21], [23]–[25]). MEFSSs are shown to have very stable responses for a wide range of incidence angles and polarizations of incidence [14]–[22]. They also have been used to design tunable FSSs [18], [26] as well as FSSs for high-power microwave (HPM) applications [26], [27].

In this paper, we present a new type of MEFSS that shows a bandpass response, which is free of spurious transmission windows over an extremely wide frequency band. The proposed harmonic-free MEFSS is composed of multiple metallic layers separated from one another by thin dielectric substrates. Each metallic layer is a two-dimensional periodic structure composed of capacitive patches or inductive wire grids with extreme sub-wavelength dimensions. A prototype of the proposed harmonic-free MEFSS with a second-order bandpass response, center frequency of operation of 3.0 GHz, and fractional bandwidth of 20% is designed and is shown to be harmonic free up to approximately 27 GHz.² A prototype of the proposed structure is also fabricated and experimentally characterized in the lab. It is demonstrated that the proposed structure maintains its harmonic-free, second-order bandpass response for both the TE and TM polarizations with incidence angles in the $\pm 60^\circ$ range up to 27 GHz.

II. PRINCIPLES OF OPERATION

A. Sources of Harmonics in MEFSSs

Fig. 1(a) shows the three-dimensional topology of different layers of a miniaturized element frequency selective surface with an $((N + 1)/2)^{th}$ -order bandpass response (N is the

¹While FSSs that have miniaturized unit cell dimensions have been studied for a long time (e.g., [13]), we use the term MEFSS to refer to FSSs with unit cells that are composed of primarily nonresonant elements (e.g., sub-wavelength capacitive patches or wire grids).

²The frequency of main transmission window is chosen primarily for ease of measurement. The concepts proposed in this paper can easily be applied to MEFSSs operating at the VHF and lower UHF frequencies as well.

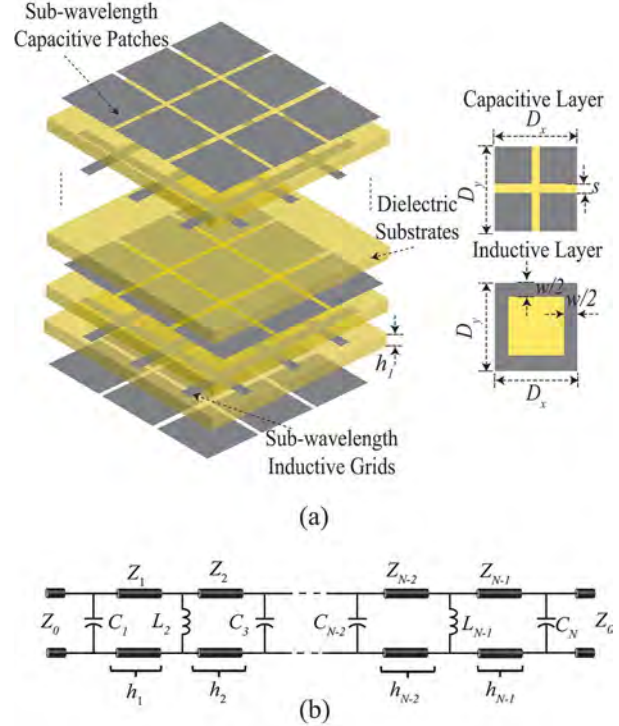


Fig. 1. (a) Topology of the bandpass MEFSS presented in [22]. The top view of the unit cells of the capacitive and inductive layers are shown on the right hand side of the figure. (b) Equivalent circuit model of the MEFSS. The structure has N metal layers and acts as an FSS with an $((N + 1)/2)^{th}$ -order bandpass response.

number of metallic layers used in this structure and is always an odd number [22]). The structure consists of two-dimensional periodic arrangements of sub-wavelength capacitive patches and planar wire grids, separated from one another by thin dielectric substrates. Assuming that the thickness of the substrate between two consecutive metal layers is h , the overall thickness of the FSS is $(N - 1) \times h$. The top views of one unit cell of a capacitive layer and that of an inductive layer are shown in the inset of Fig. 1(a). The dimension of each unit cell along the x and y directions is D . The capacitive patches are in the form of square metallic patches with dimensions of $D - s_i$, where s_i is the gap between the two adjacent patches in the i^{th} layer. The inductive wire grids are the combination of two metallic strips with the width of w oriented perpendicularly to each other. Assuming the same periodicity in both x and y directions, the frequency responses of the capacitive and inductive layers (and that of the FSS) are insensitive to the polarization of the incident wave for normal incidence.

This FSS can be modeled with the equivalent circuit model shown in Fig. 1(b), which is valid for a normally incident plane wave. In this circuit model, the capacitive patch layers are modeled with parallel capacitors C_1, C_3, \dots, C_N . The inductive wire grids are represented by parallel inductors L_2, \dots, L_{N-1} , and the thin dielectric substrates separating the inductive and capacitive layers are modeled with transmission lines with the characteristic impedances of Z_1, \dots, Z_{N-1} and lengths of h_1, \dots, h_{N-1} . Free space on each side of the FSS is modeled with semi-infinite transmission lines with characteristic impedances of $Z_0 = 377 \Omega$. The design procedure of this

device is based on synthesizing the desired filter response from the equivalent circuit model presented in Fig. 1(b), and mapping these equivalent circuit parameter values to the physical parameters of the FSS. This can be done using the procedure described in [22] and will not be repeated here for brevity.

Using the design procedure reported in [22], an MEFSS with a second-order bandpass response having a center frequency of operation of 3.0 GHz and a fractional bandwidth of 20% is designed. This structure is composed of two capacitive layers, one inductive layer, and two dielectric substrates. The physical parameters of this structure as well as the parameters of its equivalent circuit model are presented in Table I. This MEFSS is simulated using full-wave electromagnetic (EM) simulations in CST Microwave Studio and its frequency response is calculated over an extremely broad frequency band. Fig. 2 shows the calculated transmission coefficient of this structure for a normally incident plane wave in the frequency range of 0–30 GHz. As can be seen, in addition to the main transmission band centered at 3.0 GHz, there are multiple spurious transmission windows occurring at higher frequencies than that of the main one. The primary contributors to these harmonics are the resonances of the patches in the capacitive layers and the slots in the inductive layer that occur at higher frequencies. For example, the frequency of the first resonance of the capacitive patches in the capacitive layer and the slots in the inductive layer can be approximated as follows:

$$f_{r,cap} = \frac{c}{2(D-s)\sqrt{\epsilon_{r,eff,i}}} \quad (1)$$

$$f_{r,ind} = \frac{c}{2(D-w)\sqrt{\epsilon_{r,eff,i}}} \quad (2)$$

where D , s_i , and w_i are the physical parameters of the FSS unit cell shown in Fig. 1, c is the speed of light, and $\epsilon_{r,eff,i}$ is the effective dielectric constant for the i^{th} metallic layer of the FSS. In the second-order MEFSS example under discussion in this section, $\epsilon_{r,eff,1} = \epsilon_{r,eff,3} \approx (\epsilon_r + 1)/2$ for the capacitive layers and $\epsilon_{r,eff,2} \approx \epsilon_r$ for the inductive layer. Notice that in (1)–(2) the effect of the interaction between different layers on the higher order resonances of the constituting elements in each unit cell is ignored. Therefore, these formulas represent approximations of the actual resonant frequencies of the capacitive patches and apertures in the inductive layers. Using (1)–(2) along with the physical parameters of the MEFSS provided in Table I, the first resonant frequencies of the capacitive patches and the slots in the inductive layers are calculated to be 5.0 GHz and 7.8 GHz, respectively. At their first resonance, the patches in the capacitive layers act as band-stop elements, whereas the apertures in the inductive layer act as bandpass elements (see [1, pp. 26–62]). Therefore, the first spurious transmission window of this second-order MEFSS is expected to occur at a frequency close to the resonant frequency of the apertures in the inductive layer. Fig. 2 shows that this is indeed the case. At higher frequencies, the higher order resonant modes of the elements, the complex interactions between different layers, as well as the grid resonances (grating lobes) occurring at $D = n\lambda$ (e.g., see [1, pp. 26–62]) result in additional transmission windows and transmission nulls in the transmission coefficient of this device as can be observed in Fig. 2.

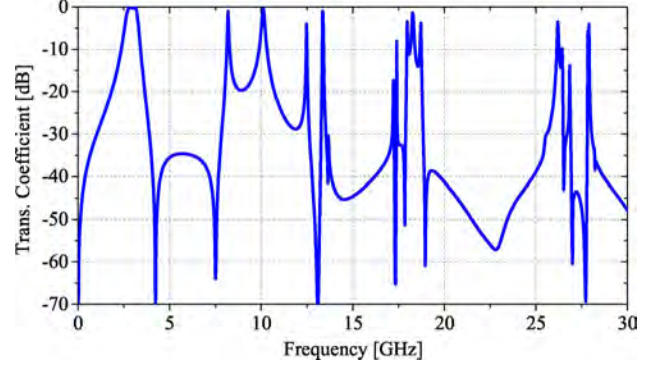


Fig. 2. Calculated transmission coefficient of the second-order bandpass FSS discussed in Section II-A with the parameters shown in Table I. Results are obtained using full-wave EM simulation in CST Microwave Studio.

TABLE I
PHYSICAL AND ELECTRICAL PARAMETERS OF THE SECOND-ORDER MEFSS WITH A CENTER FREQUENCY OF 3 GHz AND THE FRACTIONAL BANDWIDTH OF $\delta = 20\%$ DISCUSSED IN SECTION II-A

Parameter	D_x	D_y	s	w
Value	24 mm	24 mm	0.35 mm	11 mm
Parameter	h	C_1	L_2	C_3
Value	1.575 mm	1.18 pF	0.34 nH	1.18 pF

B. Concept for Designing Harmonic-Free MEFSSS

Since the first spurious passband of this MEFSS is caused by the natural harmonics of its constituting elements, an effective method for removing that from the desired frequency band of operation is to reduce the unit cell size of the structure. From (1)–(2), it can be seen that reducing D shifts these resonant frequencies to higher values. In doing this, however, the effective inductance and capacitance values provided from the metallic layers of the MEFSS must not change in order to maintain the frequency response of the structure within the desired transmission band (i.e., the element values of the equivalent circuit model of the MEFSS must not change). This shifts the spurious transmission bands to higher frequencies without disturbing the frequency response of the FSS within the desired operating band. However, implementing this in practice can be challenging, since reducing the period of the MEFSS while maintaining the desired capacitance and inductance values results in significant reduction of the minimum feature sizes of the unit cell of the MEFSS (i.e., the gap size between capacitive patches s_i and the width of the inductive wires w_i) [22]. For MEFSSs of the type shown in Fig. 1, however, this problem is more severe for the capacitive patch layers and the gap spacing between adjacent capacitive patches in these layers is the bottleneck in the process of miniaturization of the MEFSS unit cell [17]. In practice, the minimum spacing between the adjacent capacitive patches in each capacitive layer of the FSS, s_i , is determined by the minimum feature size that can be reliably fabricated using any given fabrication procedure. For most standard lithography techniques used in printed circuit board (PCB) fabrication, this minimum feature size is about 0.15 mm. Therefore, achieving the desired capacitance value from an extremely sub-wavelength periodic structure is rather challenging.

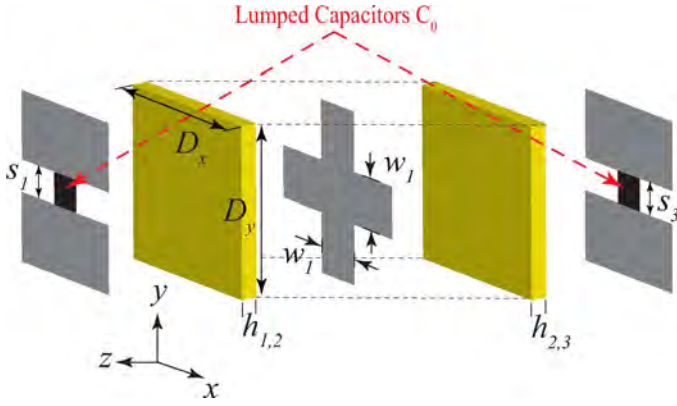


Fig. 3. Unit cell of the second-order bandpass MEFSS with the lumped capacitors loading the capacitive patch layers.

One technique for achieving the desired capacitance value in such situations is shown in Fig. 3. In this case, lumped-element capacitors C_0 are placed in parallel between the two adjacent edges of nearby capacitive patches. Taking the intrinsic capacitance of the unloaded capacitive patch layer, C_i , into account, the total capacitance of each capacitive layer in this structure can be modeled with a parallel combination of C_0 and C_i . Using this topology, the unit cell size of the capacitive patches of the structure can be reduced while maintaining the required capacitance value. To demonstrate this in practice, three different MEFSSs of the type shown in Fig. 3 are designed and simulated. All of these MEFSSs have second-order bandpass responses centered at 3.0 GHz and a fractional bandwidth of 20%. For all three cases, the gap sizes in the capacitive layers are $s = s_1 = s_3 = 0.35$ mm, and the thicknesses of the substrates are $h_{1,2} = h_{2,3} = 1.575$ mm. However, these MEFSSs have different periods and consequently, use different lumped-element capacitor values to maintain the desired frequency response. Fig. 4 shows the transmission coefficients of these three MEFSSs obtained using full-wave EM simulations in CST Studio. As expected, the frequencies of the spurious transmission windows increase as the unit cell sizes of the MEFSSs decrease. For example, for the structure with the unit cell size of $D = 10$ mm, and the lumped capacitor value of $C_0 = 0.7$ pF, the first spurious transmission window occurs at 11.5 GHz. As the unit cell size is decreased (and C_0 is increased), the frequency of the first spurious transmission window increases as well and in the extreme case of $D = 2$ mm and $C_0 = 0.95$ pF, the first spurious transmission window occurs at a frequency above 30 GHz.

C. Practical Implementation of Harmonic-Free MEFSSs

While this design example confirms the feasibility of removing spurious transmission bands from the responses of MEFSSs over a very wide frequency range, a major challenge limits the practicality of implementing MEFSSs of the type shown in Fig. 3. Specifically, the number of lumped elements needed to achieve the desired response can become extremely large, even in small FSS panels. For example, for $D = 2$ mm, a 10 cm \times 10 cm panel of the second-order MEFSS whose response is shown in Fig. 4 requires about 10 000 lumped capacitors (2 capacitive layers, 2500 capacitive patches per layer, and 2 lumped capacitors per patch to ensure polarization insensitivity). This becomes even more challenging when a

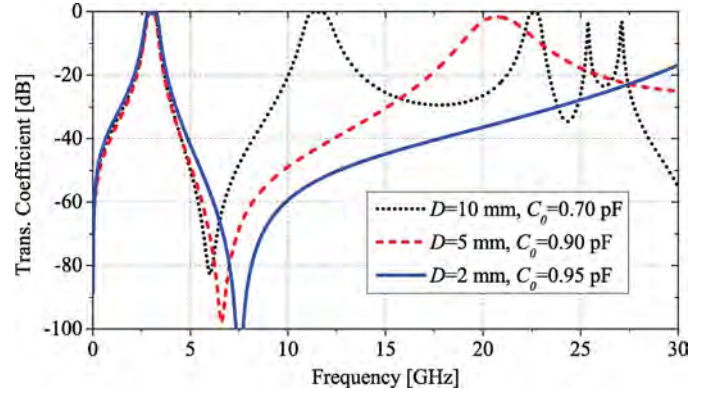


Fig. 4. Calculated transmission coefficients of the second-order bandpass MEFSS discussed in Section II-B where the capacitive patches are loaded with lumped-element capacitors. Results are obtained using full-wave EM simulation in CST Microwave Studio.

higher order filter response is required, since the number of capacitive layers in these filters increases [22]. Additionally, in MEFSSs with bandpass responses of order $P \geq 3$, $P - 2$ capacitive layers are sandwiched by dielectric substrates on both sides and are not directly accessible [22].

While the direct implementation of the MEFSS shown in Fig. 3 using lumped elements is challenging, alternative implementation techniques can be envisioned that address the practical problems of using lumped elements in a periodic structure. One such technique is to use cascaded capacitive patches separated by very thin dielectric substrates to synthesize a single capacitive layer with an effectively larger capacitance. In such an arrangement, each capacitive layer of the original MEFSS shown in Fig. 1 is replaced with multiple, closely spaced capacitive patch layers. In general, as the period of the MEFSS is reduced, the number of closely spaced capacitive patch layers needed to synthesize an effective capacitance layer will increase. Fig. 5(a) shows the unit cell of an effective capacitive layer composed of M individual capacitive patches separated from one another by $M - 1$ extremely thin dielectric substrates. For small substrate thicknesses, all these capacitive patches can be considered to be in parallel with one another and hence, they constitute a single composite capacitive layer with a larger capacitance value. Additionally, different capacitive patch layers that constitute the composite capacitive layer can overlap with each other to further increase the capacitance of the composite structure. Using M closely spaced capacitive patch layers to implement each single capacitive layer of the MEFSS shown in Fig. 1 will increase the total number of metallic layers of the MEFSS to $M \times P + P - 1$, where $P = (N + 1)/2$ is the order of the filter, and N is the total number of metallic layers of the original MEFSS shown in Fig. 1. The equivalent circuit model of the whole structure is shown in Fig. 5(b). Here, the combination of cascaded capacitive patches are modeled with $C_{1_{eff}}, \dots, C_{N_{eff}}$. Each capacitor in this equivalent circuit represents the effective capacitance obtained from one combination of M closely spaced capacitive layers. The sub-wavelength inductive wiregrids are modeled with L_2, \dots, L_{N-1} and the dielectric substrates separating the inductive layers and combined capacitive layers are modeled with the transmission lines with the lengths of h_1, \dots, h_{N-1} and the characteristic impedances of Z_1, \dots, Z_{N-1} . Free space on

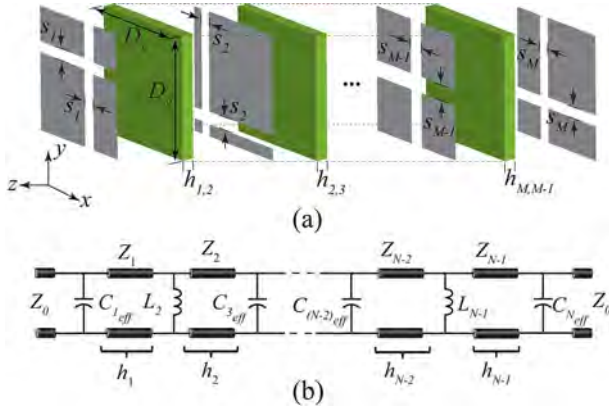


Fig. 5. (a) Multiple closely spaced capacitive patch layers are used to synthesize a single effective capacitive layer. The dielectric substrates are extremely thin. The unit cells of the patches used in different layers can overlap with each other and do not necessarily have to be aligned together. (b) The equivalent circuit model of a generalized MEFSS of the type shown in Fig. 1 in which each one of the capacitive layers is substituted with a composite, multi-layer effective capacitive layer similar to that shown in Fig. 5(a). In this equivalent circuit model $C_{i,eff}$ represents the effective capacitance of each of the composite, multi-layer capacitive structures that are used to synthesize the i^{th} capacitive layer of the MEFSS shown in Fig. 1(a).

each side of the FSS is modeled with semi-infinite transmission lines with the characteristic impedances of $Z_0 = 377 \Omega$.

There are a number of parameters that influence the effective capacitance obtained from the combination of cascaded patches. These include the number of capacitive layers in the cascade arrangement, the gap size between the adjacent capacitive patches in each layer, and the thickness and the dielectric constants of the separating substrates. Increasing the number of layers increases the effective capacitance but it will also increase the total number of layers used in the MEFSS and increases the overall thickness and the complexity of the design. Therefore, in the rest of this paper, we focus on designs that use only two cascaded capacitive layers to synthesize each of the constituting capacitive layers of the MEFSS of Fig. 1. Decreasing the gap size, increasing the dielectric constant value of the separating substrates, and decreasing their thicknesses will all increase the effective capacitance value. However, these parameters are primarily determined by the fabrication technology or the availability of commercially available substrates. In addition to these parameters, the capacitance value also depends on the offset overlap between two cascaded patches in the capacitive layer.

To demonstrate the effect of offset overlapping, we have examined a periodic structure composed of two capacitive patch layers with unit cell dimensions of $D = 6.5$ mm and the gap spacing of $s = 0.5$ mm. Both layers are assumed to be in free space and the spacing between them is $h = 0.2$ mm. As shown in Fig. 6(a), the overlap between two patch layers is modeled with a vector (x_c, y_c) connecting the centers of the two patches, within each unit cell of the structure, together. x_c refers to the horizontal offset between the positions of the two patches and y_c refers to the vertical offset between them. The structure is simulated using full-wave EM simulations in CST Studio to compute its effective capacitance as a function of the vector (x_c, y_c) . To do this, the unit cell of the structure shown in Fig. 6(b) is simulated using the periodic boundary conditions. The transmission and reflection coefficients of the structure for a normally incident wave are calculated for the two orthogonal polarizations.

These include the vertical and horizontal polarizations in which the electric field is respectively oriented along the \hat{y} and \hat{x} directions. Subsequently, the simplified equivalent circuit model of the structure, shown in Fig. 6(c) (right), is simulated in a circuit simulation software (Agilent Advanced Design System) and the transmission coefficient of the equivalent circuit model is calculated. Finally, the value of C_{eff} is tuned in ADS to match the magnitudes and the phases of the transmission and reflection coefficients obtained from the full-wave simulation and the simplified circuit model together. This way, the effective capacitance is calculated.

Fig. 6(d)-(e) shows the results obtained from these case studies for the aforementioned structure for both the vertical and horizontal polarizations. For both polarizations, the capacitance value is calculated as a function of x_c and y_c . For the vertical polarization, y_c , which represents the vertical offset between two patches, has the most significant effect on the capacitance value while x_c , which represents the horizontal offset between two patches, only has a negligible effect. However, for the horizontal polarization, x_c has the major effect and y_c only affects the capacitance negligibly. These can be described easily by the alignment of the direction of the electric field vector of the incident wave and the gap between two adjacent patches. Combining these two figures, we can find out that the maximum capacitance happens when the offset vector is equal to $(x_c, y_c) = (D/2, D/2)$. For this structure, the maximum value of the capacitance is 0.48 pF. The minimum capacitance value of 0.09 pF is obtained for the case when both patches are aligned together and $(x_c, y_c) = (0, 0)$.

D. Approximate Formula for Calculating the Capacitance of Cascade Overlapping Patches

To better understand the impact of the offset overlap on the capacitance of the cascaded patches and facilitate the design process of such structures, we have developed an analytical formula that can be used to approximate the effective capacitance of a two layer stack of cascaded capacitive patches with the offset vector of $(x_c, y_c) = (D/2, D/2)$. Fig. 7 shows a unit cell of such a structure. Observe that four parts of the upper patch layer form effective parallel plate capacitors of C_c with the bottom patch layer. C_c can be easily approximated by the following formula:

$$C_c = \frac{\epsilon_0 \epsilon_{eff} (D - s)^2}{4h} \quad (3)$$

where D is the unit cell size, s is the gap size between two adjacent patches, h is the thickness of the dielectric between two patch layers, and ϵ_{eff} represents the effective dielectric constant between the two layers. The total capacitance is modeled as the parallel combination of the intrinsic capacitance C_i , brought by the capacitive gap, in parallel with the series-parallel network of C_c capacitors as shown in Fig. 7(b). Therefore,

$$C_{total} = C_c + C_i \quad (4)$$

where

$$C_i = \epsilon_0 \epsilon_{eff} \frac{2D}{\pi} \ln \left(\frac{1}{\sin \left(\frac{\pi s}{2D} \right)} \right). \quad (5)$$

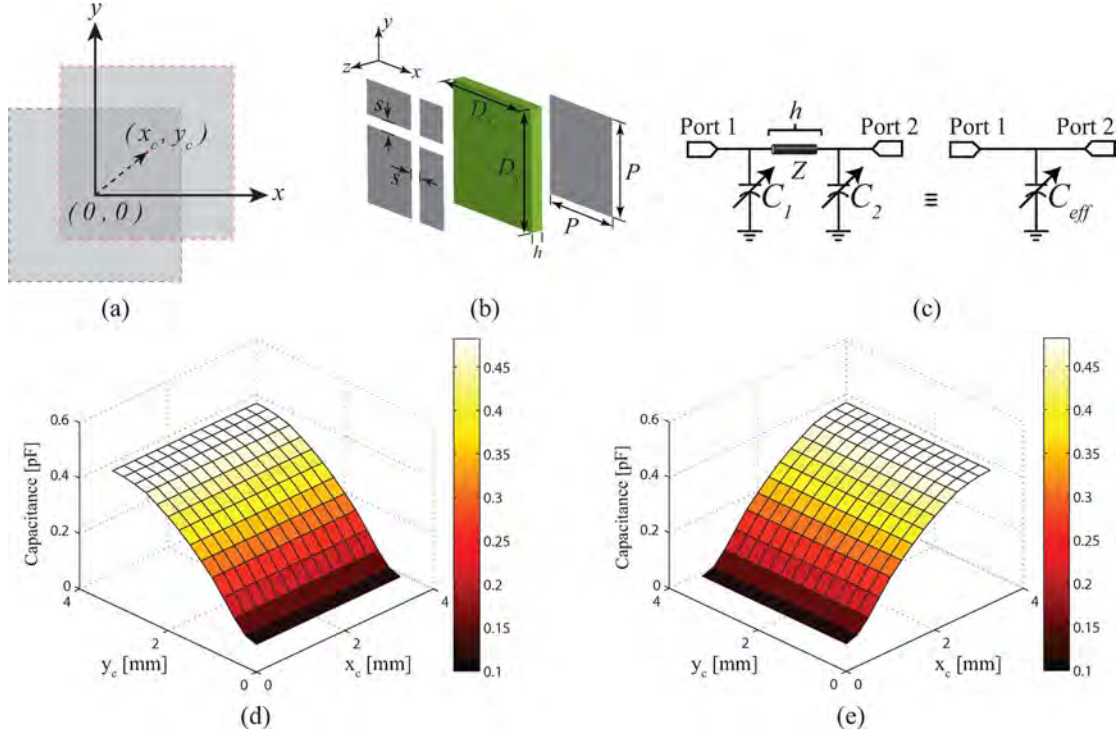


Fig. 6. (a) The unit cells of the two capacitive layers used to synthesize a single effective capacitive layer of the MEFSS of Fig. 1(a) can overlap with each other. This overlap is modeled by the vector (x_c, y_c) . (b) 3D topology of the unit cell of a composite patch layer showing the offset between the capacitive patches and the dielectric slab that separates them. (c) The equivalent circuit model of the capacitive structure shown in Fig. 6(b). (d)-(e) The extracted effective capacitance of the capacitive structure shown in Fig. 6(b) consisting of two cascaded capacitive patches and a thin substrate separating them. The structure has the unit cell dimensions of $6.5 \text{ mm} \times 6.5 \text{ mm}$. The gap size for both layers is $s = 0.5 \text{ mm}$ and the patch size is $P = 6 \text{ mm}$. The thickness of the substrate is $h = 0.2 \text{ mm}$. The study has been done for both (d) Vertical and (e) Horizontal polarizations.

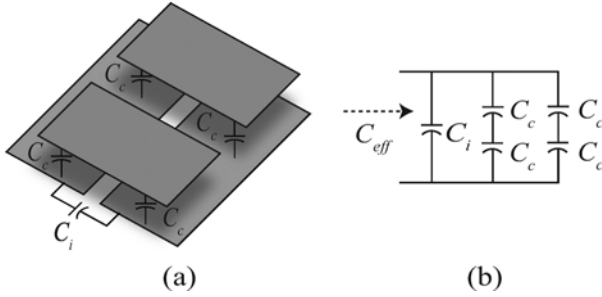


Fig. 7. (a) The capacitive structure composed of two cascaded capacitive layers can be modeled as four capacitors with capacitance values of C_c and one capacitor with a capacitance value of C_i as depicted. (b) The equivalent circuit model of the capacitive structure showing the relative arrangement of C_c and C_i capacitors.

These analytical formulas are used to calculate the effective capacitance of the two layer stack of capacitive patches examined in Section II-C as a function of the unit cell size. Fig. 8 shows the capacitance values calculated using (3)–(5) alongside the values extracted from full-wave EM simulations. As can be observed, both results are in good agreement. Thus, the analytical formula can be used in a design procedure of the proposed harmonic-free FSS to predict the capacitances to a first-order approximation.

III. DESIGN PROCEDURE AND A DESIGN EXAMPLE

A. Design Procedure

The design procedure of the proposed structure is based on synthesizing the desired filter response of the equivalent circuit

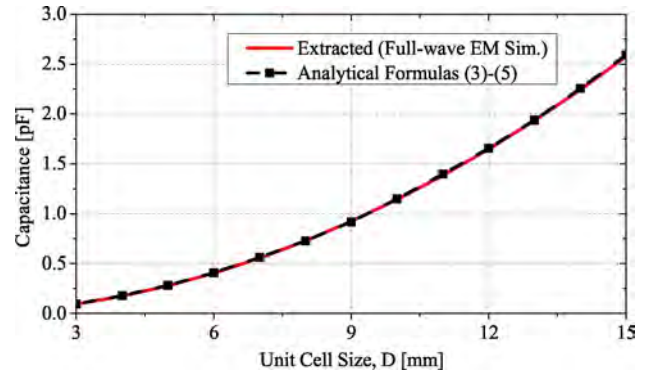


Fig. 8. Comparison between the capacitance values predicted using the analytical method and those extracted from full-wave EM simulations. The results are shown for the structure examined in Section II-C.

model of Fig. 5(b) and mapping the equivalent circuit parameters to the physical parameters of the proposed MEFSS. All the steps are similar to the procedure described in Section II-A and also that reported in [22] except the mapping of the effective parameters of the equivalent circuit model to the geometrical parameters of the capacitive layers constituting the FSS. In the mapping step, the desired values of the capacitors and inductors obtained from the equivalent circuit model are mapped to the geometrical parameters of the proposed structure. We assume that the dielectric constant of all the substrates used in the FSS are known. For simplicity, we also assume that all substrates used in the FSS have the same dielectric constants and that the thicknesses of the substrates used in between the capacitive multilayers are also equal and known. The gap size between

the sub-wavelength capacitive patches in each capacitive layer is primarily determined by the minimum feature size that can be reliably fabricated using the fabrication technology of choice. In general, the smallest gap size is chosen to ensure that the unit cell dimensions of the FSS can be reduced as much as possible. This will increase the bandwidth over which no spurious transmission window occurs. Assuming that the gap size, s , is known and fixed, the unit cell size, D , can be obtained using (3)–(5). Then, the width of the wire grids is determined from

$$L = \mu_0 \mu_{r_{eff}} \frac{D}{2\pi} \ln \left(\frac{1}{\sin \left(\frac{\pi w}{2D} \right)} \right). \quad (6)$$

Due to the close proximity of the metal layers, the presence of each layer will affect the capacitance or inductance of the other layers. Therefore, physical parameters obtained using this design process may need to be tuned slightly to achieve the desired response. This can be done by following an iterative procedure similar to the one described in [17] and [22] and will not be repeated here.

B. Design Example and Simulation Results

The procedure presented in Section III-A was followed to design an MEFSS prototype with a second-order bandpass response having a center frequency of $f_0 = 3.0$ GHz, a fractional bandwidth of $\delta = 20\%$, and no spurious transmission bands up to approximately 27 GHz. The equivalent circuit parameters of the structure (shown in Fig. 5(b)) were first determined following the design procedure described in [22]. In doing so, we assumed that dielectric substrates are non magnetic and have a dielectric constant of $\epsilon_r = 2.2$ (Rogers RT/duroid 5880). A conventional second-order MEFSS (of the type shown in Fig. 1(a)) has two capacitive layers and one inductive layer as shown in Fig. 1. In this harmonic-suppressed MEFSS, each of the capacitive layers were implemented by using two closely spaced, overlapping capacitive layers as described in Section II-C. The physical parameters of the MEFSS were obtained using the design procedure discussed in Section III-A. The structure has unit cell dimensions of $D = 5.2$ mm which is equivalent to approximately $\lambda_0/20$, where λ_0 is the free space wavelength at $f_0 = 3.0$ GHz. Since this MEFSS is composed of multiple substrates that need to be bonded together, the effect of the bonding material on the response of the MEFSS must also be taken into account. The bonding material used here was Rogers 4450F prepreg with the dielectric constant of $\epsilon_r = 3.58$ and a thickness of 0.1 mm. Introduction of the bonding layers creates an asymmetry in the topology of the proposed MEFSS, which slightly changes its response. This asymmetry was eliminated by using two closely spaced wire grids on the two sides of the middle bonding layer instead of using just one wire grid on one side as shown in Fig. 9. Using this strategy, the two inductive layers in the middle, which are separated by a thin prepreg layer, act as a single composite inductive layer. This way, the symmetry of the structure is maintained and impact of the prepreg layers on the response of the MEFSS can be minimized. The final physical parameters of the structure are listed in Table II. This structure was simulated in CST Microwave Studio and its frequency response was calculated. Fig. 10 shows the transmission coefficient of

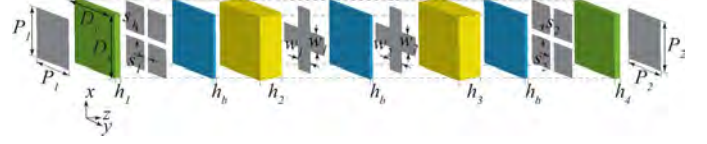


Fig. 9. Unit cell of the proposed harmonic-suppressed second-order bandpass FSS discussed in Section III-B.

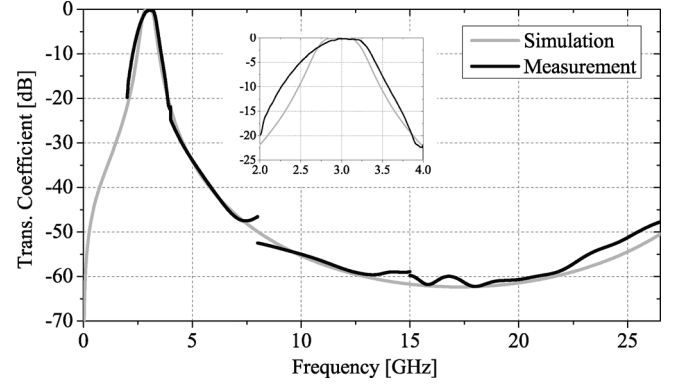


Fig. 10. Measured and calculated transmission coefficients of the FSS prototype discussed in Section III-B and shown in Fig. 11. The MEFSS is composed of the unit cells shown in Fig. 9 with physical dimensions reported in Table II.

TABLE II
PHYSICAL PARAMETERS OF THE SECOND-ORDER FSS WITH A CENTER FREQUENCY OF 3 GHz, THE FRACTIONAL BANDWIDTH OF $\delta = 20\%$, AND NO HARMONICS UP TO 27 GHz DISCUSSED IN SECTION III-B

Parameter	D	w_1	w_2	h_b
Value	5.2 mm	2 mm	2 mm	0.101 mm
Parameter	P_1	s_1	P_2	s_2
Value	4.85 mm	0.35 mm	4.85 mm	0.35 mm
Parameter	h_1	h_2	h_3	h_4
Value	1.575 mm	1.575 mm	0.127 mm	0.127 mm

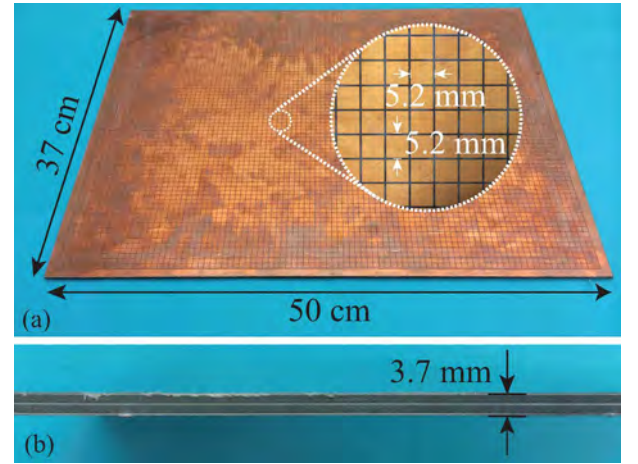


Fig. 11. (a) Photograph of the fabricated harmonic-suppressed MEFSS prototype. (b) Side view of the fabricated prototype.

this FSS in the 0–27 GHz range. As can be observed, a transmission window centered at 3.0 GHz is achieved and the FSS does not have any spurious transmission bands up to 27 GHz as expected.

IV. EXPERIMENTAL VERIFICATION AND MEASUREMENT RESULTS

A prototype of the aforementioned harmonic-suppressed MEFSS (discussed in Section III-B) was fabricated using

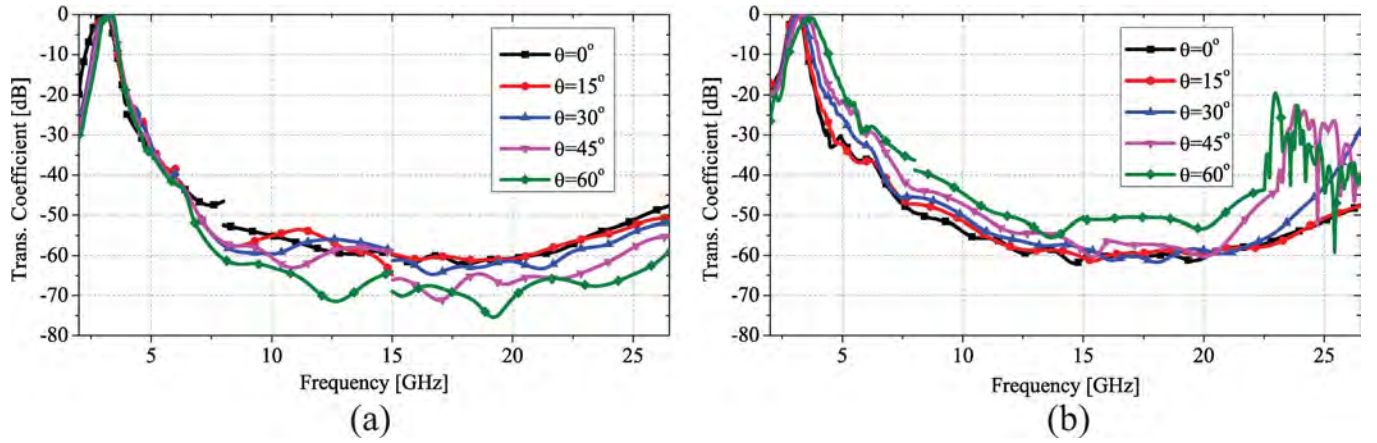


Fig. 12. (a)–(b) Measured transmission coefficients of the fabricated harmonic-suppressed MEFSS prototype discussed in Section III-B and shown in Fig. 11 for oblique incidence angles for the (a) TE and (b) TM polarization of incidence.

standard PCB lithography and substrate bonding techniques. The fabricated prototype has six metal layers, four dielectric substrates, and panel dimensions of 50 cm \times 37 cm. Rogers RT/duroid 5880 substrates ($\epsilon_r = 2.2$), with the thickness of 1.575 mm is used between inductive layers and capacitive multilayers. The same substrate material with the thickness of 0.127 mm is used between two cascaded captive patches. All the dielectric substrates are bonded together using a 0.1-mm-thick Rogers 4450F binding film with $\epsilon_r = 3.58$. The total thickness of the structure, including the bonding layers, is 3.7 mm which is less than $\lambda_0/25$ at 3.0 GHz. Fig. 11 shows a photograph of the fabricated harmonic-suppressed MEFSS.

The measurement setup consisted of a large metallic screen with the dimensions of 1.8 m \times 1.2 m with a rectangularly shaped opening having the same dimensions as those of the FSS at its center. This screen was placed between the transmitting and receiving antennas both connected to the two ports of a vector network analyzer (VNA). The large metallic fixture ensures that a transmitted EM wave must pass through the FSS to arrive at the receiver. Absorbers were used to cover points of specular reflection in the surrounding environment (e.g., on the ground and side walls of the room). Additionally, range gating in the VNA was used to eliminate the effects of scattering and diffraction of the EM waves from the edges of the metallic fixture that host the FSS as well as the effects of the multiple reflections between two antennas as discussed in [17]. Transmission coefficient measurements were carried out in two steps. First, the transmission coefficient of the screen without the FSS was measured and used for calibration. Then, the FSS was placed in the opening and its transmission coefficient was measured once again. The transmission coefficient of the MEFSS was obtained using these two measurement results. Measurements were performed in 2 GHz–27.0 GHz frequency range using multiple pairs of transmitting and receiving antennas that cover different parts of this frequency range. Over the 2 GHz–8 GHz frequency band, a pair of dual ridge horn antennas were used. A pair of X-band and a pair of K-band horn antennas were used to do the measurements in the 7.0 GHz–15 GHz and 15 GHz–27.0 GHz frequency bands, respectively. In these measurements, the X-band and K-band horn antennas were used outside of their recommended fre-

quency bands of operation (e.g., 7.0–8.0 GHz and 12–15 GHz for the X-band horns and 15 GHz–18 GHz for the K-band horns). This was done primarily due to the unavailability of other standard antennas that were specifically designed for operation at these bands during our measurements. Fig. 10 shows the measured frequency response of the MEFSS along with the full-wave simulation results. As can be observed, a relatively good agreement between the measured and simulated results is observed. The discrepancies observed between the measurement and simulation results in the vicinity of 7.0 GHz and 15.0 GHz are primarily attributed to using the receive and transmit antennas outside of their recommended frequency bands. Nonetheless, the measured result demonstrates clearly that the FSS does not have any spurious transmission windows up to 27.0 GHz.

The response of the fabricated prototype was also measured for oblique incidence angles for the TE and TM polarizations of incidence. Fig. 12(a) shows the transmission coefficients of the structure measured for the TE polarization for incidence angles in the range of 0°–60°. As can be observed, the FSS response is stable for such large incidence angles. Additionally, the structure maintains its harmonic suppressed operation for the TE polarization up to 27.0 GHz for incidence angles in the range of $\pm 60^\circ$. Fig. 12(b) shows the measured transmission coefficients of the structure for the TM polarization of incidence in the range of 0°–60°. Similar to the previous case, the FSS maintains its second-order bandpass response. However, the center frequency of operation of the structure shifts higher than 3.0 GHz for incidence angles exceeding 45°. This is also observed in other MEFSSs of the type shown in Fig. 1 (e.g., see [17]). This behavior can be explained by examining the variations of the parameters of the equivalent circuit model of the FSS under oblique incidence angles. Specifically, for the TE polarization of incidence, the capacitance values of the patch layers decrease as the angle of incidence increases while the inductance value of the wire grid does not change [28]. For the TE polarization, the series inductances—associated with small transmission lines representing the dielectric substrates of the MEFSS—increase as the incidence angle increases. These two effects compensate each other resulting in a stable center frequency of operation as the angle of incidence changes. For the

TM polarization, however, the inductance of the wire grid in the middle layer decreases as the incidence angle increases while the capacitance values of the patch layers do not change [28]. The values of the series inductances representing the short transmission lines modeling the dielectric substrates, however, decrease as the angle of incidence increases. The reduction of these inductance values results in increasing the center frequency of operation of the MEFSS for the TM polarization as the incidence angle increases. This effect, however, becomes significant only when the incidence angle increases beyond 45° as seen in Fig. 12. Additionally, for the TM polarization, as the angle of incidence is increased, one of the higher spurious transmission windows starts to shift towards lower frequencies and is observed in the results shown in Fig. 13(b) for $\theta = 45^\circ$ and $\theta = 60^\circ$. The peak transmission coefficient of this spurious band, however, remains below -20 dB for incidence angles up to 60° . Thus, the MEFSS maintains its desired harmonically suppressed transfer function for the TM polarization for incidence angles in the $\pm 60^\circ$ range as well.

V. CONCLUSION

We presented a new method for designing miniaturized-element frequency selective surfaces with higher order bandpass responses, which are free of spurious transmission windows over an extremely wide frequency band. The proposed harmonic-suppressed MEFSSs take advantage of the concept of cascaded, overlapping capacitive patch layers to drastically reduce the unit cell size of the structure. Using multiple closely spaced capacitive layers with overlapping unit cells to synthesize a single effective capacitive layer leads to a larger capacitance value for given unit cell dimensions. As a result, the natural resonant frequencies of these patches and the apertures within the wire grids shift to higher frequencies and a harmonic-free response over an extremely large bandwidth can be achieved. The proposed concept was experimentally verified by designing an MEFSS prototype having a second-order bandpass response with a fractional bandwidth of 20% at 3.0 GHz, which does not demonstrate any spurious transmission windows up to 27 GHz. This MEFSS was also fabricated and experimentally characterized using a free-space measurement setup. Measurements confirmed that the fabricated structure is indeed free of spurious transmission windows over the expected frequency band of operation. Additionally, we examined the performance of this prototype for various incidence angles and polarizations of the incident EM wave. The fabricated MEFSS prototype demonstrates a stable frequency response for both the TE and TM polarizations of incidence and maintains its harmonic free operation for incidence angles in the $\pm 60^\circ$ range for both the TE and TM polarizations of incidence. The concept presented in this work can also be expanded to design MEFSSs for the VHF and lower UHF frequency bands. If the MEFSS design presented in this work is directly scaled, it is expected that it will maintain the same harmonic free bandwidth (i.e., a 9:1 bandwidth). However, as the center frequency of operation of the MEFSS decreases, it may be necessary to extend the harmonic-free range of operation of the device to ensure that the device does not show any spurious transmission windows up to high frequencies (e.g., 20 GHz). In such situations, the

harmonic-free bandwidth of the MEFSS can be increased by using more cascaded capacitive layers with smaller unit cell dimensions. For example, computer simulations of an MEFSS with three cascaded capacitive patches operating in the 500–700 MHz range indicate that it remains free of spurious transmission windows up to 18.0 GHz, or equivalently a 30:1 bandwidth.

ACKNOWLEDGMENT

The authors would like to thank Dr. E. Caswell and Mr. C. Blakslee from Level-3 Communications for useful discussions and the valuable feedback they provided about this work.

REFERENCES

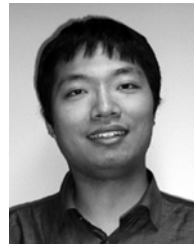
- [1] B. A. Munk, *Frequency Selective Surfaces: Theory and Design*. New York, NY, USA: Wiley-Interscience, 2000.
- [2] N. Behdad, "A second-order band-pass frequency selective surface using non-resonant sub-wavelength periodic structures," *Microw. Opt. Technol. Lett.*, vol. 50, no. 6, pp. 1639–1643, Jun. 2008.
- [3] S. Chakravarty, R. Mittra, and N. R. Williams, "On the application of the microgenetic algorithm to the design of broad-band microwave absorbers comprising frequency-selective surfaces embedded in multilayered dielectric media," *IEEE Trans. Microw. Theory Tech.*, vol. 49, no. 6, pt. 1, pp. 1050–1059, 2001.
- [4] A. Fallahi, A. Yahaghi, H. Benedickter, H. Abiri, M. Shahabadi, and C. Hafner, "Thin wideband radar absorbers," *IEEE Trans. Antennas Propag.*, vol. 58, no. 12, pp. 4051–4058, Dec. 2010.
- [5] A. Monorchio, G. Manara, and L. Lanuzza, "Synthesis of artificial magnetic conductors by using multilayered frequency selective surfaces," *IEEE Antennas Wireless Propag. Lett.*, vol. 1, no. 1, pp. 196–199, Jan. 2002.
- [6] M. A. Hiranandani, A. B. Yakovlev, and A. A. Kishk, "Artificial magnetic conductors realised by frequency-selective surfaces on a grounded dielectric slab for antenna applications," *IEE Proc. Microw. Antennas Propag.*, vol. 153, no. 5, pp. 487–493, 2006.
- [7] M. Al-Joumayly and N. Behdad, "Wideband planar microwave lenses using sub-wavelength spatial phase shifters," *IEEE Trans. Antennas Propag.*, vol. 59, no. 12, pp. 4542–4552, Dec. 2011.
- [8] M. Li, M. Al-Joumayly, and N. Behdad, "Broadband true-time-delay microwave lenses based on miniaturized element frequency selective surfaces," *IEEE Trans. Antennas Propag.*, vol. 61, no. 3, pp. 1166–1179, Mar. 2013.
- [9] J. A. Encinar, "Design of two-layer printed reflectarrays using patches of variable size," *IEEE Trans. Antennas Propag.*, vol. 49, no. 10, pp. 1403–1410, Oct. 2001.
- [10] W. S. Arceneaux, R. D. Akins, and W. B. May, "Absorptive/transmissive radome," U.S. patent 5,400,043, May 21, 1995.
- [11] B. Li and Z. Shen, "Synthesis of quasi-elliptic bandpass frequency-selective surface using cascaded loop arrays," *IEEE Trans. Antennas Propag.*, vol. 61, no. 6, pp. 3053–3059, Jun. 2013.
- [12] F. Costa and A. Monorchio, "A frequency selective radome with wideband absorbing properties," *IEEE Trans. Antennas Propag.*, vol. 60, no. 6, pp. 2740–2747, Jun. 2012.
- [13] E. A. Parker and A. N. A. El-Sheikh, "Convolutional array elements and reduced size unit cells for frequency-selective surfaces," *IEE Proc. H (Microw., Antennas Propag.)*, vol. 138, no. 1, pp. 19–22, Feb. 1991.
- [14] K. Sarabandi and N. Behdad, "A frequency selective surface with miniaturized elements," *IEEE Trans. Antennas Propag.*, vol. 55, no. 5, pp. 1239–1245, May 2007.
- [15] H. Liu, K. L. Ford, and R. J. Langley, "Miniaturised bandpass frequency selective surface with lumped components," *Electron. Lett.*, vol. 44, no. 18, pp. 1054–1055, Aug. 2008.
- [16] F. Bayatpur and K. Sarabandi, "Multipole spatial filters using metamaterial-based miniaturized-element frequency selective surfaces," *IEEE Trans. Microw. Theory Tech.*, vol. 56, no. 12, pp. 2742–2747, Dec. 2008.
- [17] N. Behdad and M. Al-Joumayly, "A new technique for design of low-profile, second-order, band-pass frequency selective surfaces," *IEEE Trans. Antennas Propag.*, vol. 57, no. 2, pp. 452–459, Feb. 2009.
- [18] F. Bayatpur and K. Sarabandi, "Tuning performance of metamaterial-based frequency selective surfaces," *IEEE Trans. Antennas Propag.*, vol. 57, no. 2, pp. 590–592, Feb. 2009.

- [19] R. J. Langley, L. L. Hui, and K. L. Ford, "Design methodology for a miniaturized frequency selective surface using lumped reactive components," *IEEE Trans. Antennas Propag.*, vol. 57, no. 9, pp. 2732–2738, Sep. 2009.
- [20] C.-N. Chiu and K.-P. Chang, "A novel miniaturized-element frequency selective surface having a stable resonance," *IEEE Antennas Wireless Propag. Lett.*, vol. 8, pp. 1175–1177, 2009.
- [21] N. Behdad and M. Al-Joumayly, "A generalized synthesis procedure for low-profile frequency selective surfaces with odd-order band-pass responses," *IEEE Trans. Antennas Propag.*, vol. 58, no. 7, pp. 2460–2464, Jul. 2010.
- [22] M. Al-Joumayly and N. Behdad, "A generalized method for synthesizing low-profile, band-pass frequency selective surfaces with non-resonant constituting elements," *IEEE Trans. Antennas Propag.*, vol. 58, no. 12, pp. 4033–4041, Dec. 2010.
- [23] G. Yang, T. Zhang, W. Li, and Q. Wu, "A novel stable miniaturized frequency selective surface," *IEEE Antennas Wireless Propag. Lett.*, vol. 9, pp. 1018–1021, 2010.
- [24] C.-N. Chiu and W.-Y. Wang, "A dual-frequency miniaturized-element FSS with closely located resonances," *IEEE Antennas Wireless Propag. Lett.*, vol. 12, pp. 163–165, 2013.
- [25] F. Deng, X. Q. Yi, and W. J. Wu, "Design and performance of a double-layer miniaturized-element frequency selective surface," *IEEE Antennas Wireless Propag. Lett.*, vol. 12, pp. 721–724, 2013.
- [26] M. Li and N. Behdad, "Fluidically tunable frequencyselective/phase shifting surfaces for high-power microwave applications," *IEEE Trans. Antennas Propag.*, vol. 60, no. 6, pp. 2748–2759, Jun. 2012.
- [27] M. Li and N. Behdad, "Frequency selective surfaces for pulsed high-power microwave applications," *IEEE Trans. Antennas Propag.*, vol. 61, no. 2, pp. 677–687, Feb. 2013.
- [28] O. Luukkonen, C. Simovski, G. Granet, G. Goussetis, D. Lioubtchenko, A. V. Raisanen, and S. A. Tretyakov, "Simple and accurate analytical model of planar grids and high-impedance surfaces comprising metal strips or patches," *IEEE Trans. Antennas and Propag.*, vol. 56, no. 6, pp. 1624–1632, Jun. 2008.



Seyed Mohamad Amin Momeni Hasan Abadi (S'14) received the B.S. degree in electrical engineering from the University of Tehran, Tehran, Iran, in 2011. He is currently working toward the Ph.D. degree at the University of Wisconsin-Madison, Madison, WI, USA.

He has been a Research Assistant in the Department of Electrical and Computer Engineering, University of Wisconsin-Madison since 2011. His research interests include electrically small antennas, periodic structures, frequency selective surfaces, phased-array antennas, and RF/Microwave circuit and system design.



Meng Li (M'13) received the B.Sc. degree in electrical engineering from Southeast University, Nanjing, China, in 2008, and the Ph.D. degree in electrical engineering from the University of Wisconsin at Madison, Madison, WI, USA, in 2013.

He is currently with Qualcomm Inc, San Diego, CA, USA, designing radio frequency front-end architecture for next-generation wireless standards. Prior to joining Qualcomm, he was a Graduate Research Assistant with the University of Wisconsin-Madison from 2009 to 2013. His research

interests include RF/microwave circuits, frequency selective surfaces, phased array antennas, and reconfigurable RF front ends.

Dr. Li received the 2012 Piergiorgio L. E. Uslenghi Letters Prize Paper Award of the IEEE Antennas and Propagation Society, was the recipient of the second prize in the student paper competition of the Antenna Application Symposium held in Allerton Park, IL, September 2011, and was a student paper finalist in the IEEE 2010 APS/URSI Symposium held in Toronto, ON, Canada and in the IEEE 2013 APS/URSI Symposium held in Orlando, FL, USA.



Nader Behdad (S'99–M'06–SM'12) received the B.S. degree in electrical engineering from Sharif University of Technology, Tehran, Iran, in 2000 and the M.S. and Ph.D. degrees in electrical engineering from the University of Michigan, Ann Arbor, MI, USA, in 2003 and 2006, respectively.

Currently he is an Associate Professor in the Electrical and Computer Engineering Department, University of Wisconsin-Madison, Madison, WI, USA. From 2009 to 2013, he was an Assistant Professor in the Department of Electrical and Computer Engineering,

University of Wisconsin, and from 2006 to 2008, he was an Assistant Professor in the Department of Electrical Engineering and Computer Science, University of Central Florida, Orlando, FL, USA. His research expertise is in the area of applied electromagnetics. In particular, his research interests include electrically small antennas, antenna arrays, antennas for biomedical applications, biomedical applications of RF/microwaves, periodic structures, frequency selective surfaces, passive high-power microwave devices, metamaterials, and biomimetics and biologically inspired systems in electromagnetics.

Dr. Behad is currently serving as an Associate Editor for the IEEE ANTENNAS AND WIRELESS PROPAGATION LETTERS and served as the cochair of the technical program committee of the 2012 IEEE International Symposium on Antennas and Propagation and USNC/URSI National Radio Science Meeting. He received the 2012 Piergiorgio L. E. Uslenghi Letters Prize Paper Award of the IEEE Antennas and Propagation Society. He is also the recipient of the 2011 CAREER award from the National Science Foundation, the 2011 Young Investigator Award from the Air Force Office of Scientific Research, and the 2011 Young Investigator Award from the Office of Naval Research. He received the Office of Naval Research Senior Faculty Fellowship in 2009, the Young Scientist Award from the International Union of Radio Science (URSI) in 2008, the Horace H. Rackham Predoctoral Fellowship from the University of Michigan in 2005–2006, the best paper awards in the Antenna Applications Symposium in September 2003, and the second prize in the paper competition of the USNC/URSI National Radio Science Meeting, Boulder, CO, USA, in January 2004. His graduate students were the recipients of the ten different awards/recognitions at the IEEE Pulsed Power & Plasma Science (2013), IEEE AP-S/URSI Symposium (2010, 2012, 2013), and the Antenna Applications Symposium (2008, 2010, 2011).

A Low-Profile, Wideband Antenna with Vertically-Polarized Directional Radiation

Kasra Ghaemi, *Student Member, IEEE*, and Nader Behdad, *Senior Member, IEEE*

Abstract—A low-profile, compact and wideband vertically-polarized antenna demonstrating directional radiation characteristics in both the azimuth and the elevation planes is presented. The antenna is composed of four bent-diamond-shaped half loops placed on a ground plane. The half loops are fed at their centers and short circuited to the ground at their ends. Two of the half loops are fed in phase while the other two are fed with 180° phase difference generating omni-directional and figure-eight shaped radiation patterns, respectively. Coherent combination of these radiation patterns generates a cardioid-shaped directional pattern. A prototype of the antenna was fabricated and characterized. The antenna has electrical dimensions of $0.54\lambda_{min} \times 0.4\lambda_{min} \times 0.116\lambda_{min}$ at its lowest frequency of operation and operates over a 2:1 bandwidth.

Index Terms—Broadband antennas, cardioid-shaped patterns, directional antennas, wideband antennas.

I. INTRODUCTION

Many military systems use HF, VHF, and UHF frequency bands for a variety of applications including communications, sensing, and electronic warfare. Monopole whips are the dominant type of antennas used at these frequencies. They, however, are high-profile structures with large visual signatures, which is not desirable in military applications. Furthermore, monopole antennas can only provide omni-directional radiation patterns in the azimuth plane. However, in certain applications, having an antenna that radiates a vertically-polarized wave, like a monopole but has a directional radiation pattern in the azimuth plane is desired. Examples include situations where multiple antennas are mounted on a single platform and the interference between them should be minimized or where directional patterns are needed to perform jamming operations.

Various techniques have been examined in the past for designing broadband, vertically-polarized directional antennas. Reflector-backed or self-grounded radiators were examined in [1]-[3]. These techniques require having a relatively large reflector placed behind the antenna to reduce the back radiation levels. This, however, increases the overall height of the antenna. The lowest-profile antenna among these antennas has an electrical height of around $0.19\lambda_{min}$ at its lowest frequency of operation.¹ Miniaturized horn antennas have also been used to achieve directional radiation in a compact form factor [4]-[6]. However, they are relatively high profile.

This work is supported by Office of Naval Research under ONR award No. N00014-11-1-0618. The authors are with the Department of Electrical and Computer Engineering, University of Wisconsin-Madison, Madison, WI 53706-1691 USA (e-mail: ghaemi@wisc.edu; behdad@wisc.edu).

¹The height of antennas without ground planes are divided by two to have a fair comparison. Additionally, realized gain values of those antennas are added to 3 dB for the same reason.

TABLE I
COMPARISON OF THE PERFORMANCE OF THE PROPOSED ANTENNA WITH THE CURRENT STATE-OF-THE-ART IN LOW-PROFILE, VERTICALLY-POLARIZED, WIDEBAND DIRECTIONAL ANTENNAS.

Group	$L \times W \times H (\lambda_{min}^3)$	BW	FTBR (dB)
[1]	$0.43 \times 0.32 \times 0.25$	4.5:1	10
[2]	$0.5 \times 0.5 \times 0.2$	3.2:1*	10
[3]	$0.36 \times 0.16 \times 0.19$	7.5:1	10
[4]	$0.55 \times 0.18 \times 0.135$	4.5:1	8
[5]	$1 \times 0.33 \times 0.59$	30:1	15
[6]	$0.25 \times NR \times 0.21$	4.5:1	10
This Work	$0.54 \times 0.4 \times 0.116$	2:1	9

*denotes for a dual-band response in the reported bandwidth.

In this letter, we present a low-profile, compact and wideband antenna capable of providing vertically-polarized, directional radiation in the azimuth plane. The architecture of this antenna can easily be modified to allow for dynamically switching its direction of maximum radiation by 180° . The antenna is composed of four half loops mounted on a ground plane and provides a cardioid-shaped radiation pattern over a wide bandwidth using a simple feed network. A prototype of the proposed antenna is fabricated and characterized. The antenna has electrical dimensions of $0.540\lambda_{min} \times 0.400\lambda_{min} \times 0.116\lambda_{min}$ at its lowest frequency of operation. The fabricated prototype demonstrates a VSWR below 2.4:1 and directional radiation patterns with typical front-to-back ratios of 9 dB over an octave bandwidth. Table. I shows a comparison between the performance of this antenna with those of the current state-of-the-art. Observe that the design proposed in this work offers an extremely low overall height, which is important for VHF/UHF military applications.

II. PRINCIPLES OF OPERATION

A. Antenna Design

A cardioid-shaped radiation pattern can be obtained by coherently combining an omnidirectional radiation pattern with a figure-eight-shaped one. This can be done by combining the radiation patterns of a dipole and a loop [7], or a monopole and a slot [8]. To generate the cardioid-shaped patterns over a broad bandwidth, however, broadband radiating elements are required. In [9], a compact ultra-wideband antenna composed of two closely coupled loops was presented. The compact size and low height of this antenna makes it a suitable element to be used in generating a cardioid-shaped radiation pattern over a wide bandwidth. Fig. 1(a) shows two closely-spaced half loop antennas with the shape of bent diamond arms. These half loops are fed at their center tips and short-circuited to the ground at their ends. When the two half loops are fed in phase,

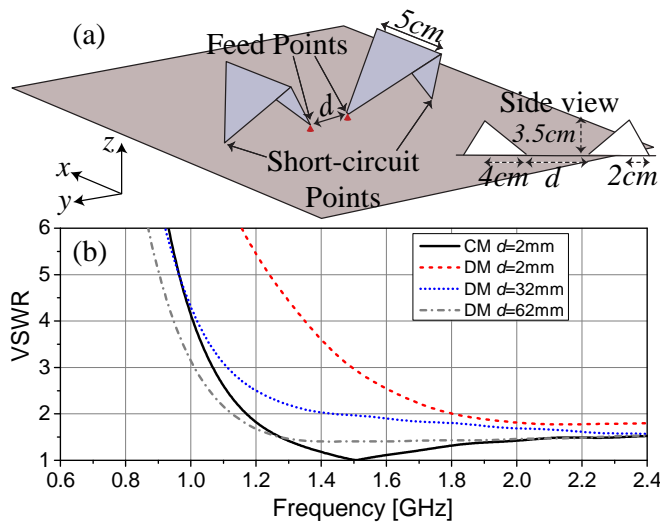


Fig. 1. (a) Two identical half loops placed close to each other. (b) Effect of the separation between the two half loops on the differential-mode VSWR.

the whole antenna structure acts as a wideband vertically-polarized monopole [9]. On the other hand, when they are fed with a 180° phase difference, it radiates a vertically-polarized wave with a figure-eight-shaped radiation pattern in the azimuth plane over a wide bandwidth [10]. Therefore, the common and differential modes of the structure shown in Fig. 1(a) can be used as building blocks of a cardioid-shaped radiation pattern over a broad bandwidth.

The input VSWR of the antenna shown in Fig. 1(a) is shown in Fig. 1(b) for both the common mode (CM) and the differential mode (DM). The results of the DM are presented for various spacings between the two loops. Observe that, for small d values, the lowest frequency of operation of the CM excitation is lower than that of the DM one. As the spacing between the two half loops increases, the VSWR of the DM improves and its lowest frequency of operation is reduced. This is due to the anti-symmetric current distributions of the antenna in DM. When the spacing between the half loops is small, the vertical components of the currents tend to cancel each other making the impedance matching process difficult. Fig. 1(b) shows that the operating band of the antenna having $d = 62$ mm in the DM is similar to that of the antenna with $d = 2$ mm excited in the CM. Based on this, we propose the antenna topology shown in Fig. 2 consisting of four half loops. In this structure, the two loops with spacing of 2 mm are fed in CM and the other two loops with a spacing of 62 mm are fed in DM. They respectively provide the omni-directional and the figure-eight patterns needed to obtain a cardioid-shaped radiation pattern in the azimuth plane.

To feed the two DM half loops, a compact, surface-mount RF transformer is used (NCS1-222-75+ from Minicircuits, Inc.). The transformer operates from 0.95 to 2.20 GHz with a maximum loss of 1 dB. When the DM half loops are fed with this transformer, the input VSWR of the antenna slightly deteriorates compared to what is shown in Fig. 1(b). To improve this, the shape of the DM half loops are modified as shown in Fig. 2. Specifically, the inner arms of these antennas are

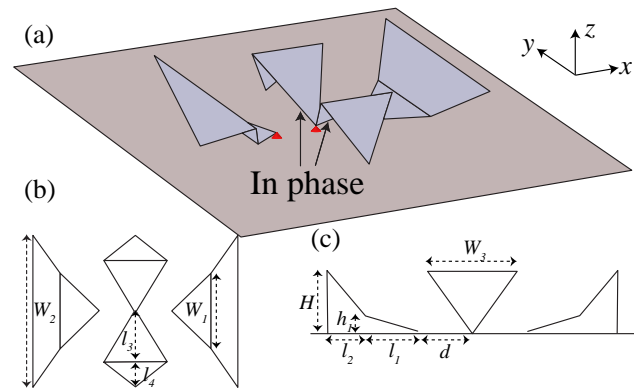


Fig. 2. (a) 3D view, (b) Top view, (c) Side view. $d=3$, $l_1=3$, $l_2=2.1$, $l_3=4$, $l_4=2$, $h_1=1$, $H=3.5$, $W_1=6$, $W_2=12$, $W_3=5$. All the values are in cm.

modified to two-section pieces of metal with abrupt changes in their slopes. This helps improve the impedance matching of the DM array when fed with the commercially-available balun. The width of the two half loops used in the DM array are also increased compared to the ones shown in Fig. 1(a). This was done to increase the gain of the DM array along the $\phi=0^\circ$ and 180° directions at higher frequencies. This way the DM array can maintain its desired figure-eight-shaped radiation pattern in the azimuth plane over a wide bandwidth. The physical dimensions of this antenna are reported in the caption of Fig. 2 and the antenna has a volume of $16.2 \text{ cm} \times 12 \text{ cm} \times 3.5 \text{ cm}$.

B. Feed Network Design

To generate the desired cardioid-shaped radiation patterns, the DM and CM patterns must be combined with proper complex weights. Figs. 3(a) and 3(b) show respectively the amplitude and the phase patterns of the DM and CM arrays in the far field at 1.5 GHz. Observe that the realized gain values of the CM and DM arrays along $\phi=0^\circ$ in the azimuth plane are almost equal (see Fig. 3(a)). The absolute phases of the CM and DM arrays along $\phi=0^\circ$ in the azimuth plane are 185° and 197° , respectively (see Fig. 3(b)). To create a null along $\phi=0^\circ$, a phase difference of 180° must be created between the radiated fields of the two arrays along $\phi=0^\circ$. This creates a perfect destructive interference of the two radiated waves along $\phi=0^\circ$ and a constructive interference along $\phi=180^\circ$. This can be done by using a feed network which provides equal amplitude excitations for both arrays and excites the CM array with a phase shift of 168° . The normalized radiation pattern provided by such a feed network is shown in Fig. 3(a). As seen, this pattern presents a maximum along $\phi=180^\circ$ and a null along $\phi=0^\circ$ in the azimuth plane. The direction of this maximum radiation can be changed from $\phi=180^\circ$ to $\phi=0^\circ$ if a constant phase difference of 180° is introduced between the two arrays. This can be done by switching the polarity of the feed terminals of the DM array. Alternatively, one can place a switchable $0^\circ/180^\circ$ binary phase shifter in the path of the CM array to electronically switch this direction of maximum radiation between $\phi=0^\circ$ and 180° along the azimuth plane.

The feed network can be implemented using a power splitter and a phase shifter. The power ratio expected at the output

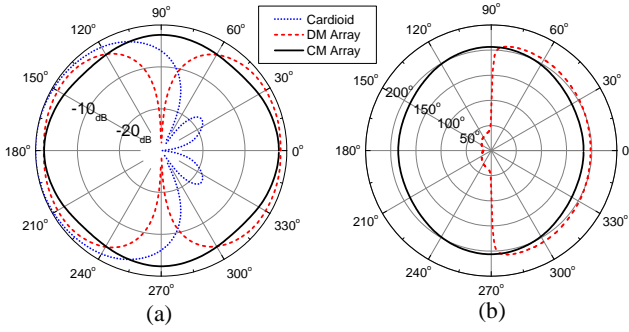


Fig. 3. (a) Realized gain values of the waves radiated by the CM and DM antenna arrays and the normalized combined cardioid-shaped radiation pattern at 1.5 GHz, (b) Phases of the radiated waves by the CM and DM antenna arrays at 1.5 GHz.

of the power splitter and the phase shift level needed for creating cardioid-shaped patterns may be calculated using the procedure described earlier. However, unlike the single-frequency cardioid-shaped pattern shown in Fig. 3, the goal of this work is to achieve wideband directional radiation patterns. Therefore, the calculation of the relative amplitudes and phases of excitations of the DM and CM arrays are conducted at multiple frequencies over the entire band. Due to the frequency-dependence of the complex radiation patterns of these arrays, the required excitation coefficients of the CM and DM arrays are also frequency dependent. However, for simplicity, a frequency-independent feed network was used in the proof-of-concept prototype. The power division ratio and phase shift values were chosen to achieve a front-to-back ratio better than 9 dB across the 1-2 GHz frequency range. The consequence of using a frequency-independent feed network is that the array will not provide a perfect cardioid-shaped radiation pattern at every frequency within 1-2 GHz. The feed network used in this work uses a power divider with an output power ratio of 3 dB and a phase shifter realized by a transmission line with an electrical length of 110° at 1 GHz as shown in Fig. 4(a). These values were chosen by carefully considering the magnitudes and phases of the radiation patterns of the DM and CM arrays over the whole bandwidth. Fig. 4(b) shows a schematic of the feed network

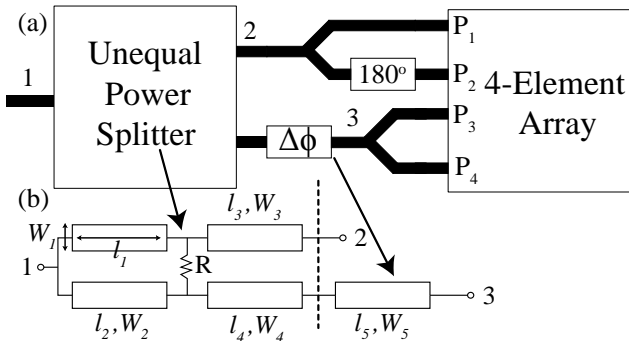


Fig. 4. (a) Feed network topology, (b) Feed network implementation using distributed elements. $l_1=30.3$, $l_2=32.2$, $l_3=29.8$, $l_4=30.6$, $l_5=55.4$, $W_1=3.1$, $W_2=0.65$, $W_3=4.3$, $W_4=2.4$, $W_5=3.2$, All the values are in mm. $R=106\ \Omega$.

implementation on a 60 mil RO4003C substrate. Achieving a more directional radiation characteristic over the entire bandwidth is possible by employing a frequency-dependent feed network. Additionally, by placing a switchable $0^\circ/180^\circ$ phase shifter in series with the transmission-line phase shifter, the direction of the maximum radiation of the array can be switched between $\phi=180^\circ$ and 0° , electronically.

III. MEASUREMENT RESULTS AND DISCUSSION

The antenna prototype discussed in Section II, with ground plane has dimensions of $20\text{ cm} \times 20\text{ cm}$, was fabricated. Below the ground plane, a 60 mil RO4003C substrate is placed on which two $50\ \Omega$ microstrip lines are fabricated to feed the CM and DM arrays. One of the microstrip lines directly feeds the CM array using a through-substrate via. To feed the DM array, a surface mount transformer is mounted on the bottom side of the substrate and its input pin is connected to the other $50\ \Omega$ microstrip line. Transformer's output pins are then connected to two $50\ \Omega$ microstrip lines feeding the two half loops of the DM array using through-substrate vias.

Fig. 5(a) shows the simulated and measured VSWRs of the CM and DM arrays. The CM (DM) array demonstrates a measured VSWR below 2.6 (2.5) over a frequency range of 1.1-2.0 GHz (1.0-2.0 GHz). The small discrepancies observed between the measured and simulated results are attributed to fabrication tolerances, the uncertainties in modeling via holes and SMA connectors, losses of the conductors, tolerances of the dielectric constant value of the substrate, and the uncertainties involved in modeling of the transformer.

The measured two-port S-parameters of the antenna network for the CM and DM arrays were then exported to Agilent ADS and were used in a simulation along with the feed network shown in Fig. 4(b) to obtain the measured input VSWR of the antenna as seen from the input port of the feed network. Fig. 5(b) shows the results obtained from this process along with the all-simulated input VSWR of the antenna system. As seen, the proposed antenna with its feed network is capable of providing a VSWR below 2.4:1 from 0.87-2.2 GHz.

The radiation parameters of the antenna were measured using a multi-probe near field system from 0.8 to 2.2 GHz. First, the radiation characteristics of the CM antenna array was measured while the other array was terminated with a $50\ \Omega$ load. Subsequently, the patterns of the DM array were measured while the CM array was terminated with $50\ \Omega$. Through this process, the far-field amplitudes and phases of the radiated fields of the two antenna arrays were measured at every point in space and at different frequencies. Then, these measured radiation patterns were combined in a post-processing step. In this step, the simulated S-parameters of the feed network shown in Fig. 4(b) and the measured S-parameters of the antenna were used to obtain the actual magnitudes and excitation coefficients of the CM and DM arrays at every frequency point where the far-field radiation patterns were measured. Using this process, the radiation patterns of the antenna with its feed network were obtained. Fig. 6 shows the normalized combined radiation patterns of the fabricated prototype and those of the simulated model both in

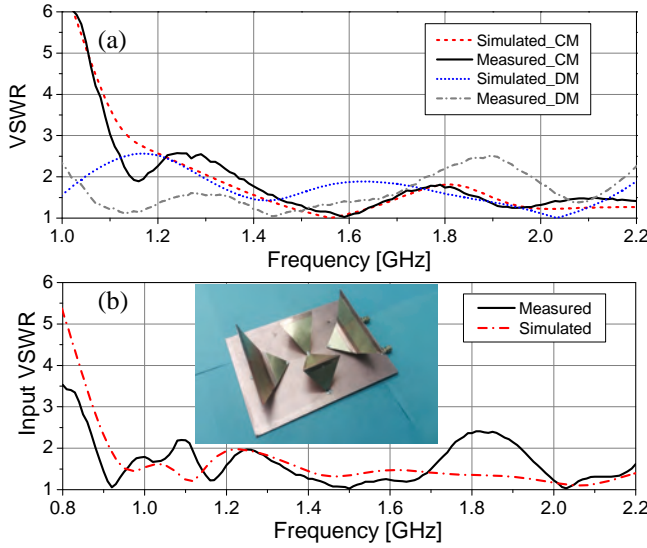


Fig. 5. (a) Simulated and measured VSWRs of the CM and DM antenna arrays, (b) Simulated and measured input VSWR seen at the input port of the feed network with the photograph of the fabricated prototype in its inset.

the azimuth ($x-y$) and in the elevation plane ($x-z$). As seen, directional radiation patterns are demonstrated in both planes over a 2:1 bandwidth. There is also a very good agreement between the simulated and measured responses. Observe that the antenna demonstrates a very good polarization purity. The direction of the maximum beam in the E-plane is tilted towards zenith since it is mounted over a finite ground plane [11]. Simulation results indicate that using a larger ground plane reduces the radiation towards the lower hemisphere, slightly increases the realized gain of the antenna, and reduces the cross-polarized radiation. Increasing the ground-plane size does not significantly impact the directionality and the front-to-back ratio of the antenna. The measured total efficiency and realized gain of the antenna are shown in Fig. 7. These parameters take into account the impedance mismatch and losses of the whole system including the feed network. As seen, the total efficiency is above 60% and the realized gain

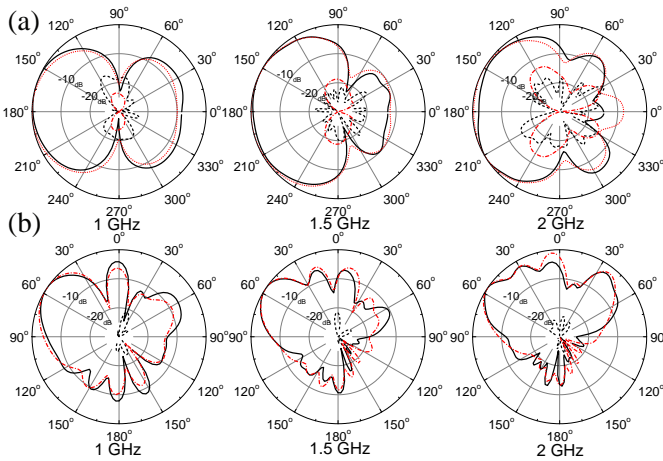


Fig. 6. Normalized (combined) radiation pattern of the antenna in the (a) azimuth plane ($x-y$), (b) elevation plane ($x-z$). Black solid (red dotted) line is the measured (simulated) co-pol (E_θ), black dashed (red dash-dotted) line is the measured (simulated) cross-pol (E_ϕ).

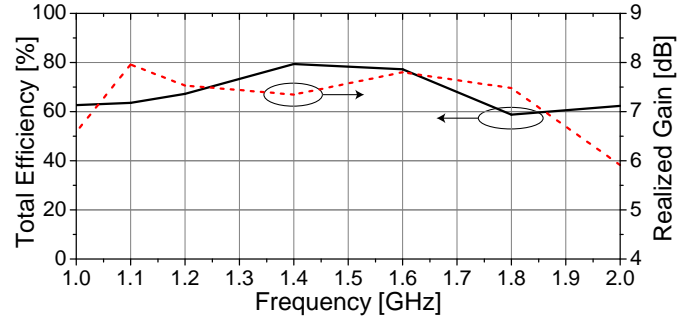


Fig. 7. Total efficiency and the realized gain of the antenna.

of the antenna is above 6 dBi for the whole bandwidth.

IV. CONCLUSIONS

A low-profile, compact and wideband vertically-polarized antenna showing directional radiation characteristics in the azimuth plane was presented. The antenna is composed of four bent diamond-shaped half loops placed on a ground plane. The half loops are fed properly by a feed network to achieve a cardioid-shaped directional radiation pattern over an octave bandwidth. The electrical dimensions of the antenna are $0.54\lambda_{min} \times 0.4\lambda_{min} \times 0.116\lambda_{min}$ at its lowest frequency of operation and it demonstrates an input VSWR below 2.4:1. Due to its low profile, compact dimensions, wide bandwidth and directional radiation characteristics, this design is expected to be useful for military communication systems operating at HF, VHF, and UHF frequency bands.

REFERENCES

- [1] A. Elsherbini and K. Sarabandi, "Directive coupled sectorial loops antenna for ultrawideband applications", *IEEE Antennas Wireless Propag. Lett.*, vol. 8, pp. 576-579, Apr. 2009.
- [2] Xi-Tong Wu, Wen-Jun Lu, Jin Xu, Kin Fai Tong, and Hong-Bo Zhu, "Loop-Monopole Composite Antenna for Dual-Band Wireless Communications," *IEEE Antennas Wireless Propag. Lett.*, vol. 14, pp. 293-296, Oct. 2014.
- [3] J. Yang and A. Kishk, "A novel low-profile compact directional ultrawideband antenna: the self-grounded Bow-Tie antenna," *IEEE Trans. Antennas Propag.*, vol. 60, pp. 1214-1220, Mar. 2012.
- [4] A. Elsherbini and K. Sarabandi, "Compact directive ultra-wideband rectangular waveguide based antenna for radar and communication applications", *IEEE Trans. Antennas Propag.*, vol. 60, pp. 2203-2209, Mar. 2012.
- [5] A. Mehrdadian, K. Forooghi, "Design and Fabrication of a Novel Ultrawideband Combined Antenna," *IEEE Antennas Wireless Propag. Lett.*, vol. 13, pp. 95-98, Jan. 2014.
- [6] M. A. Elmansouri, and Dejan S. Filipovic, "Design of Combined-Antennas Using Spherical Modes," *Antenna Applications Symposium*, Sep. 2014.
- [7] P. Hansen, J. Schukantz, "Dual-feed, dual-mode antenna for mono-directional pattern," US Patent H1, 571, 1996.
- [8] K. Itoh and D. K. Cheng, "A novel slots-and-monopole antenna with a steerable cardioids pattern", *IEEE Trans. Aerosp. Electron. Syst.*, vol. AES-8, pp. 130-134, Mar. 1972.
- [9] N. Behdad, M. Li, and Y. Yusuf, "A very low-profile, omnidirectional, ultrawideband antenna," *IEEE Antennas Wireless Propag. Lett.*, vol. 12, pp. 280-283, Feb. 2013.
- [10] M. Li, Y. Yusuf, and N. Behdad, "A compact, low-profile, ultra-wideband antenna utilizing dual-mode coupled radiators," *Progress In Electromagnetics Research B*, vol. 50, pp. 235-251, 2013.
- [11] K. Ghaemi and N. Behdad, "A Low-Profile, Vertically-Polarized Ultra-Wideband Antenna with Monopole-Like Radiation Characteristics," *IEEE Trans. Antennas Propag.*, vol. 63, no. 8, pp. 3699-3705, Aug. 2015.